BRNO UNIVERSITY OF TECHNOLOGY
VYSOKÉ UČENÍ TECHNICKÉ V BRNĚ

FACULTY OF MECHANICAL ENGINEERING
FAKULTA STROJNÍHO INŽENÝRSTVÍ

INSTITUTE OF PHYSICAL ENGINEERING
ÚSTAV FYZIKÁLNÍHO INŽENÝRSTVÍ

PHASE IMAGING BELOW THE DIFFRACTION LIMIT
FÁZOVÉ ZOBRAZOVÁNÍ POD DIFRAKČNÍM LIMITEM

MASTER'S THESIS
DIPLOMOVÁ PRÁCE

AUTHOR — **Bc. Daniel Nečesal**
AUTOR PRÁCE

SUPERVISOR — **Ing. Petr Dvořák, Ph.D.**
VEDOUCÍ PRÁCE

BRNO 2020

BRNO UNIVERSITY OF TECHNOLOGY
FACULTY OF MECHANICAL ENGINEERING

Specification Master's Thesis

Department:	Institute of Physical Engineering
Student:	**Bc. Daniel Nečesal**
Study programme:	Applied Sciences in Engineering
Study field:	Physical Engineering and Nanotechnology
Supervisor:	**Ing. Petr Dvořák, Ph.D.**
Academic year:	2019/20

Pursuant to Act no. 111/1998 concerning universities and the BUT study and examination rules, you have been assigned the following topic by the institute director Master's Thesis:

Phase imaging below the diffraction limit

Concise characteristic of the task:

In the last decade, rapid progress has been made in the field of phase imaging using holographic microscopy. Though, a fundamental limitation of these techniques for use in nanophotonics is the diffraction limit. However, this limit can be overcomed using near–field aperture scanning optical microscopy (a–SNOM). A special technique which combines the a–SNOM method with phase microscopy has recently been developed at the Institute of Physical Engineering. It opens new research possibility for optimization of this technique and investigation of its applications.

Goals Master's Thesis:

1) Carry out a research study on the topic of microscopic phase imaging below the diffraction limit.
2) Prepare suitable nanophotonic structures for phase imaging.
3) Build and optimize experimental setup for measuring phase images below the diffraction limit.
4) Experimentally, study the phase distribution of the fabricated samples using the experimental setup.

Recommended bibliography:

NOVOTNY, Lukas a Bert HECHT. Principles of Nano-Optics. Cambridge University Press, (2012), ISBN-10: 1107005469.

DVOŘÁK, Petr, Michal KVAPIL, Petr BOUCHAL, et al. Near-field digital holography: a tool for plasmon phase imaging. Nanoscale. 2018, 10(45), 21363-21368.

Students are required to submit the thesis within the deadlines stated in the schedule of the academic year 2019/20.

In Brno, 30. 10. 2019

prof. RNDr. Tomáš Šikola, CSc.
Director of the Institute

doc. Ing. Jaroslav Katolický, Ph.D.
FME dean

Abstrakt
Tato diplomová práce se zabývá konstrukcí interferenčních zařízení pro výzkum měření fáze světla na mikrostrukturách a fáze plazmonů na nanostrukturách. V první kapitole je vybudován teoretický základ pro optiku a nanofotoniku používaných v budoucích kapitolách. Následně je popsána interference vln a jejich praktické použití pro prolomení difrakčního limitu a úvod do holografie plazmonů. Prvním experimentální sestavou je Machův-Zehnderův holografický mikroskop. Je popsán způsob, jak ho sestavit z běžně dostupných součástek a jak byl navržen ovládací software k jeho používání. Následně jsou popsány výsledky naměřené pomocí tohoto zařízení. Poslední kapitola je zaměřena na sestavení holografického SNOM přístroje pro studování plazmonů a jejich interference. Je zde základní princip operace zařízení a jak byl navržen software pro automatizaci měření pro zrychlení vědeckých postupů. Nakonec jsou předloženy výsledky měření holografie plasmonů pomocí naší sestavy.

Abstract
This Master's thesis is focused on construction of phase imaging systems capable of studying both micro- and nanosized objects. The first chapter lays the foundation of optics and nanophotonics. Then the interference of coherent waves and its practical application are discussed for the use of breaking the diffraction limit and extracting information out of optical systems. First experimental setup discussed is the Mach–Zehnder type in–line digital holographic microscope. We show a way of constructing this device out of cheap materials and how to design its control software. Then, the experimental results obtained using this device are presented. In the last chapter, we focus on how a SNOM holography can be implemented. We show how our version of a holographic SNOM was built and how automation via software was utilized to reduce operator time waste. Finally, we present experimental results obtained using our system.

Klíčová slova
SNOM, interference SPP, interferenční struktury, holografie, interferometrie, Machův-Zehnderův interferometr, a-SNOM.

Keywords
SNOM, SPP interference, interferometric structures, holography, interferometry, Mach-Zehnder interferometer, a-SNOM.

NEČESAL, D. *Fázové zobrazování pod difrakčním limitem*. Brno: Vysoké učení technické v Brně, Fakulta strojního inženýrství, 2020. 75 s. Vedoucí práce Ing. Petr Dvořák, Ph.D.

I hereby declare that I have written my master's thesis on the topic of Phase imaging below the diffraction limit on my own under the guidance of my master's thesis supervisor Ing. Petr Dvořák, Ph.D. working with the technical literature and other bibliographic sources which are all quoted properly in the body of the thesis and listed in the bibliography section at the end of this thesis.

In Brno ....
(Daniel Nečesal)

I would like to thank Petr Dvořák for his time and guidance during the making of this Master's thesis. I also want to thank Jan Krpenský, Lukáš Kejík, and Michal Horák for helping me with sample preparations, Martin Hrtoň for the developement of theory and Michal Kvapil for his simulations of surface plasmon interference, and Jiří Spousta for his detailed corrections of this thesis.

Many thanks go to Olivier Martin for allowing me to complete an Erasmus exchange at NAM laboratories at EPFL, where part of this thesis was developed and Tomáš Šikola for mediating this exchange. I want to especially give my thanks to Toralf Scharf who was a superb mentor during the internship.

Last but not least, special thanks go to my parents and their partners, my brother, family, and friends, without whom this thesis would never would have been made.

Contents

INTRODUCTION

Humans have been fantasizing about the microworld from at least the classical antiquity. After all, the existence of the basic blocks of the world we live in, atoms, were postulated by a Greek philosopher Democritus in the 5th century BCE [1]. Though the natural philosophers have long speculated what the matter of this world is made out of, nobody could really peer into the microcosmos with their own eyes and confirm their hypotheses. The first acknowledged microscopist and microbiologist Antonie van Leeuwenhoek developed his high magnification microscope in 1670s, launching the scientific field of optical microscopy [2]. Optical microscopes have been steadily improving over the centuries and there seemed to be not limit on how deep into the microworld could a man peer. This changed in 1873 when Ernst Abbe proposed a hard limit on how small objects can be distinguished using an optical microscope. This so–called diffraction limit set the maximum resolution of an optical imaging system to around half a of a wavelength of the light used; good enough for studying micrometer sized objects, but far too prohibitive to delve into the nanoworld. The resolution could be improved by lowering the wavelength, but optical elements stop working for even near–UV light not to mention the studied objects are often damaged or destroyed by high energy photons, so a different approach was needed.

Several attempts were made to improve classical microscopy by introducing confocal microscopy, phase contrast microscopy, and interferometry, but it was not until the 1960s with the advent of lasers, CCD chips, and fast computing that a new method became viable, the digital holographic microscope. Originally discovered as an accident when optimizing scanning electron beam microscope by Dennis Gabor [3]. While the lateral resolution still remained diffraction limited, the longitudinal resolution was practically unlimited. This opened a whole new research field and led to many advances in surface sciences [4], microbiology [5], metrology [6], and microoptics [7].

To truly break the diffraction limit, a different approach was needed. The problem lied in that the information from the sample was lost before it reached the microscope. First, every microscope has a fixed aperture, so it can capture only certain spatial frequencies reducing its resolution. Second, the near–field information about the sample decays exponentially, so is impossible to detect in the far–field where microscopes operate. Both of these problems were solved in a theoretical work by Edward Hutchinson Synge in 1928. He envisioned an opaque metal film with an aperture in the center of around 100 nm. This aperture would scan the surface of the sample and collect information just under a 100 nm distance from the sample. He proposed the biggest challenge would be scanning with the aperture at constant distance from the sample [8]. This

problem was overcome with the advent of Scanning Tunneling Microscopy (STM) in 1981 and Atomic Force Microscopy (AFM) in 1986 at IBM [9]. These methods laid the foundation for a collection of measuring techniques called Scanning Probe Microscopy (SPM). These methods bring a sharp tip under 10 nm close to sample and scan the surface with a nanometer precision. By using approach mechanism developed by the AFM and a metal coated transparent tip with an aperture, Pohl and his team developed in 1984 the first Scanning Near–Field Optical Microscope (SNOM) [10]. This device could scan a sample with nanometer precision in all three dimensions while capturing or delivering light through the metal aperture on the apex of the scanning tip. A true super–resolution optical microscopy was born. It quickly found use in studying nanostructures [11, 12], microbiological samples [13], plasmons [14], and extreme light–mater interactions [15].

As scientists and engineers delved deeper into light–matter interactions, they discovered plasmons, collective oscillations of the free electron gas density, are responsible for large portion of optical phenomena in metals and semiconductors. This created a whole new branch of physics called Plasmonics. The main topic of interest of plasmonics is the quaziparticle traveling across metal–dielectric interface called surface plasmon polariton (SSP). In recent years, nanosize structures utilizing SPPs, called metasurfaces, are being studied intensely as they can perform same roles as traditional optical elements on a flat chip [16]. From wavefront shaping [17], light polarization [18], sensing [19] to flat lenses [20], and cloaking [21]. To study the properties of SPPs and the materials utilizing them, SNOM is the obvious choice as it measures both SPP signal and the topography with nanometer precision. Just as classical microscopy was improved by capturing both amplitude and phase by switching to holography, sensitivity of SNOM can be further improved by utilizing holographic methods. Surface plasmon holography implemented by scanning near–field microscopy is a new emerging research field and it offers new exciting possibilities for probing the nanoworld with optical trapping [22] and studying metasurfaces [23, 24].

In the first part of this thesis, we explain the basic physics of nano–optics. We begin with Maxwell's equations which govern the interaction of light and matter. Next, we describe basic models which arise from these equations. From these models we build the foundation of the field of plasmonics, and describe its main topic of interest, the surface plasmon polariton. In last section, we explain the history, physics, and applications of scanning near–field microscopy for the science of nanotechnology.

In second chapter, we focus on interferometry and its applications. We open the chapter with explanation on the physical mechanism of interferometry, the interference of two traveling waves and the formation of standing waves. Next, we describe the two basic types of interferometers along with their typical usage. Afterwards, we explain phase extraction and the two different methods commonly employed for the task. We also talk about the errors associated with phase shifting interferometry. In last part of the chapter, we focus on SPP interferometry.

In third chapter, we describe a Mach–Zehnder type in–line digital holographic microscope which was built in the Nanophotonics and Metrology laboratories of Ecole polytechnique fédérale de Lausanne (EPFL) in Switzerland. First, we present a detailed

schematic and how it operates. Then, we show the finished setup and the parts we have used. Next, we explain how a custom software written for the microscope and we describe each module in detail. In the last part, we show our experimental measurements of microlens arrays and metasurfaces obtained by the microscope.

In last chapter, we describe holographic scanning near–field microscope we have built in the laboratories of Brno University of Technology at the Institute of Physical Engineering. First, we describe the experimental layout with a 3D model of the system and mechanism of operation. Then, we reveal the finished microscope and describe all the parts used. Next, we present a custom software for controlling the microscope remotely and data evaluation along with its inner details and the operator usage loops. Finally, we present measurements of SNOM holography along with theoretical numerical models for comparison.

1. NANO–OPTICS

Nano–optics is a scientific field focused on studying light–matter interactions at nanometer scales near or beyond the the diffraction limit. It emerged from the fast advance of nanotechnologies which provided the necessary tools for fabricating and studying samples at this scale. The central principle which allow nano–optics to exist is the confinement of light on a boundary of two media of different refractive index. An electromagnetic wave traveling in free space follows the dispersion relation $\hbar\omega = c \cdot \hbar k$ which ties the frequency of the wave ω with the wavevector $k = \sqrt{k_x^2 + k_y^2 + k_z^2}$ with a constant c, the speed of light. If we confine this wave to measure small objects, the wave must still obey the Heisenberg's uncertainty principle, and for example in x–axis this means obeying the following relation

$$\hbar\Delta k_x \cdot \Delta x \geqslant \hbar/2, \tag{1.1}$$

where k_x is the x component of the wave vector k. As k_x can never be larger than the whole vector $k_x < 2\pi/\lambda$, so a following equation is also true

$$\Delta x \geqslant \frac{\lambda}{4\pi}. \tag{1.2}$$

This formulation of spatial confinement is very similar to the Abbe's diffraction limit. As long as all components of k are real, this limit cannot be broken, at least not by focusing the refracting light. However, near an interface of two media with different index of refraction an exponentially decaying field can exist. In such case, the wavevector component perpendicular to the interface will be imaginary $k_z \in \mathbb{C}$. This allows the wavevector components parallel to the interface's plane to be much higher than the previously stated free space limit. In such a case, the lateral resolution can be increased indefinitely, at least in theory.

This basic argument of how spatial inhomogeneity can induce theoretically infinite spatial confinement and break the diffraction limit is the foundational insight of nano–optics. The main challenge of nano–optics is to find material configurations which allow this confinement, what are the physical implications of it, and how to exploit it in useful way [25].

1.1 Maxwell's equations

The behavior of electromagnetic field in a material is governed by a set of four partial differential equations known as Maxwell's equation. Here is the macroscopic formulation of Maxwell's equations:

$$\nabla \cdot \mathbf{D} = \rho_f, \tag{1.3}$$

$$\nabla \cdot \mathbf{B} = 0, \tag{1.4}$$

$$\nabla \times \mathbf{E} = -\frac{\partial \mathbf{B}}{\partial t}, \tag{1.5}$$

$$\nabla \times \mathbf{H} = \mathbf{J}_f + \frac{\partial \mathbf{D}}{\partial t}. \tag{1.6}$$

Gauss's law, eq. 1.3, describes the relationship between the electric displacement field $\mathbf{D}$ and the free charge density ρ_f. Looking at the equation, reveals electric displacement field is 'oozing' out of free charges in the material. Oppose to this, Gauss's law for magnetism, eg. 1.4, reveals that magnetic field $\mathbf{B}$ has no monopoles: magnetic field lines always form a closed loop. Maxwell–Faraday equation, eg. 1.5, describes the relationship between electric field $\mathbf{E}$ and time changing magnetic field $\mathbf{B}$. Ampère-Maxwell's law, eq. 1.6, describes how magnetizing field $\mathbf{H}$ is tied to free current density $\mathbf{J}_f$ and time changing electric displacement field $\mathbf{D}$.
When a free space electromagnetic field enters a medium containing charged particles, permanent or induced electric/magnetic dipole moments are modified. This gives rise to a polarization field $\mathbf{P} = \varepsilon_0 \chi_e \mathbf{E}$ and a magnetization field $\mathbf{M} = \chi_m \mathbf{H}$, where ε_0 is the permittivity of vacuum. These induced fields are proportional to the strength of the driving field by the coefficients of proportionality called electric susceptibility χ_e and magnetic susceptibility χ_m. In order to apply these macroscopic Maxwell's equations, the relationships between $\mathbf{D}$ and $\mathbf{E}$; $\mathbf{B}$ and $\mathbf{H}$ have to be described:

$$\mathbf{D} = \varepsilon_0 \mathbf{E} + \mathbf{P} = \varepsilon_0 (1 + \chi_e) \mathbf{E} = \varepsilon_0 \varepsilon_r \mathbf{E} = \varepsilon \mathbf{E}, \tag{1.7}$$

$$\mathbf{H} = \frac{1}{\mu_0} \mathbf{B} - \mathbf{M} = \frac{1}{\mu_0 (1 + \chi_m)} \mathbf{B} = \frac{1}{\mu_0 \mu_r} \mathbf{B} = \frac{1}{\mu} \mathbf{B}, \tag{1.8}$$

where ε_0 is the free space permittivity and μ_0 is the permeability of free space. The material parameters, relative permittivity ε_r and relative permeability μ_r are in general complex function. For homogeneous materials they are constant in the material, but inside inhomogeneous materials they depend on location in space and possibly time. For anisotropic materials they become tensors. Also, they heavily depend on the frequency of the driving electromagnetic wave. For the displacement field $\mathbf{D}$ the linear approximation works well because most electric fields produced in laboratory conditions are much smaller than the interatomic electric fields of the materials at $10^{11}\,\mathrm{V/m}$.

However, the linear approximation for the magnetizing field $\mathbf{H}$ can break down for common materials like iron leading to hysteresis.

Fortunately, in plasmonics, the materials are generally linear, isotropic, and non-magnetic media ($\mu_r = 1$). This simplifies the problem of modeling material properties to finding suitable function of permittivity ε. It will be a complex function of frequency ω of the incident electromagnetic wave $\varepsilon(\omega) = \varepsilon_1(\omega) + \mathrm{i}\varepsilon_2(\omega)$.

When a current passes through a material, the current density $\mathbf{J}$ is proportional to the applied electric field $\mathbf{E}$ by a proportionality constant σ which is called conductivity,

$$\mathbf{J} = \sigma\mathbf{E}. \tag{1.9}$$

With that we can introduce Poynting's theorem which can be derived from Maxwell's equations. The proof is left as an exercise for the reader.

$$-\frac{\partial}{\partial t}\int_V (\frac{1}{2}\mathbf{E}\cdot\mathbf{D} + \frac{1}{2}\mathbf{B}\cdot\mathbf{H})\,\mathrm{d}V = \oint_{\partial V}(\mathbf{E}\times\mathbf{H})\cdot\mathrm{d}\mathbf{A} + \int_V \mathbf{J}\cdot\mathbf{E}\,\mathrm{d}V, \tag{1.10}$$

where ∂V is the boundary of the volume V. The equation holds for arbitrary volume shape. The term of the left side of the equation 1.10 represents temporal change of electromagnetic energy in the volume. The first term on the right side is the energy flow across the boundary of the volume of space and the second term on the right is the energy which the fields dissipate by exerting force on charged particles in the volume. The first term on the right is called the Poynting vector $\mathbf{S}$ which represents the directional energy flux of an electromagnetic field,

$$\mathbf{S} = \mathbf{E}\times\mathbf{H}. \tag{1.11}$$

When measuring electromagnetic waves using optical devices like a CCD chip, we measure the transferred energy over finite time period. So, the average average power flow is of interest. If the electromagnetic fields are sinusoidal $\propto \exp(-\mathrm{i}\omega t)$, the time averaged Poynting vector equals

$$\langle\mathbf{S}\rangle = \frac{1}{2}\,\mathrm{Re}(\mathbf{E}\times\mathbf{H}^*), \tag{1.12}$$

where * denotes the complex conjugate. If the electromagnetic field is not periodic, but rather evanescent (exponentially decaying), the time average Poynting vector equals zero, so evanescent waves do not propagate into far–field.

An electromagnetic wave traveling through a medium can strongy couple to an electric dipole excitation of crystal lattice. This coupling is called a polariton. Polaritons can couple with an vibrational excitation which can couple to light [26]. From Maxwell's equation we derive a wave equation of light in a lossy medium with no free charges $\rho_f = 0$ [27]

$$-\nabla^2\mathbf{E} = -\varepsilon(\omega)\mu(\omega)\frac{\partial^2\mathbf{E}}{\partial t^2} - \sigma(\omega)\mu(\omega)\frac{\partial\mathbf{E}}{\partial t} \tag{1.13}$$

For the case of plane wave $\mathbf{E} \propto \exp(-\mathrm{i}(\mathbf{k}\cdot\mathbf{r} - \omega t)$, the previous equation can be solved as

$$-\mathrm{i}\omega\mu(\omega)\sigma(\omega) + \omega^2\varepsilon(\omega)\mu(\omega) - k^2 = 0, \tag{1.14}$$

where $\mathbf{k}$ is the wave vector. This equation can be simplified by introducing a complex dielectric function $\hat{\varepsilon}$ [28]

$$\hat{\varepsilon}(\omega) = \varepsilon_0\varepsilon_r(\omega) - \mathrm{i}\frac{\sigma(\omega)}{\omega}. \tag{1.15}$$

Then, eq. 1.14 can be rewritten as

$$\mu(\omega)\hat{\varepsilon}(\omega) = \frac{k^2}{\omega^2}. \tag{1.16}$$

This is the dispersion relation of electromagnetic waves or polaritons in a medium containing no free charges. If the medium is a metal then the interaction between polaritons and plasmons (collective oscillations of electron gas) gives rise to a new quazi–particle plasmon polariton. The theory behind plasmon interactions will be explained in the following section.

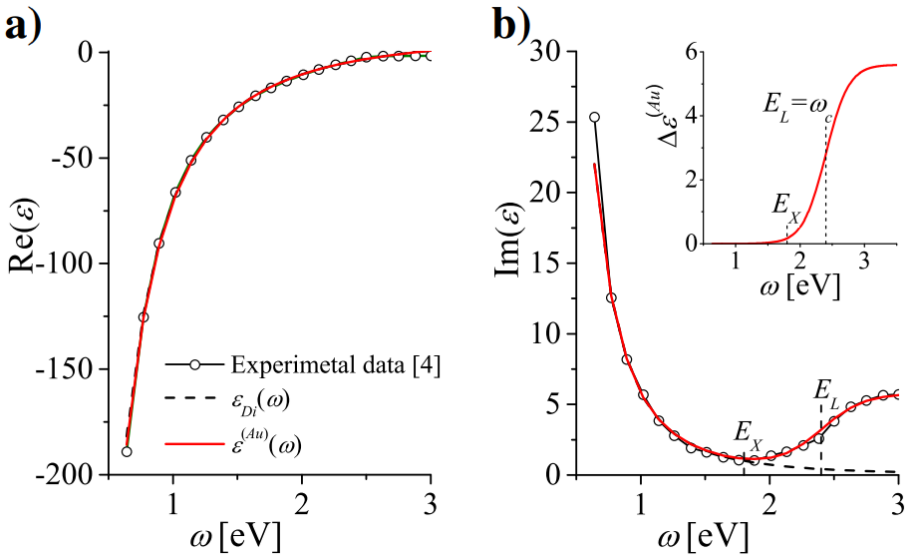

Fig. 1.1: Comparison of the real (a) and (b) imaginary part of the dielectric function for gold resulting from pure and from modyfied Drude model. Black dashed lines: $\varepsilon_{Di}(\omega)$ with parameters $\Gamma = 9.84$, $\omega_p = 9.010\,\mathrm{eV}$, $\Gamma = 0.072\,\mathrm{eV}$. Red solid lines: $\varepsilon^{Au}(\omega)$ with the same parameters Γ, ω_p and Γ, but accounting for the frequency dependent interband transitions over 1.8 eV by adding term $\Delta\varepsilon^{(Au)}$. Experimental data taken from [29] are presented by the line with circles. Reused from [30]

1.2 Drude model

As we have shown in the last section, the dielectric function is what governs the interaction between metals and electromagnetic waves. To get physically accurate models of dielectric function one must calculate the response of charge distribution in the medium to an external electromagnetic field. The problem can be solved at different levels of approximation. Some require large computational resources, and input parameters which are hard to estimate. Fortunately, classical models are precise enough for most applications in plasmonics. Metals, materials with free charge carriers, can be modeled as a medium with unbound oscillating charge carriers which is called the Drude model.

The Drude model is derived as following. First, external oscillating electric field $E = E_0 \exp(-\mathrm{i}\omega t)$ accelerates the free electrons which are in turn damped by a viscous force $F_v = -m_e \Gamma \dot{x}$. The physical meaning of this damping is scattering of electrons on other electrons, lattice imperfections, phonons, impurities, or grain boundaries. Second, using Newton's second law we derive the following equation of motion for a one-dimensional system:

$$m_e \ddot{x} = -m_e \Gamma \dot{x} - eE, \tag{1.17}$$

where m_e resp. $-e$ are mass resp. charge of an electron. Then, we assume the electron displacement x to be time varying as $x = x_0 \exp(-\mathrm{i}\omega t)$ and subsequently solve for x_0:

$$x_0 = \frac{e}{m_e} \frac{1}{\omega^2 + \mathrm{i}\omega\Gamma} E_0 \tag{1.18}$$

The polarization field is proportional to the electric dipole moment induced per unit volume $P = -n_e e x$. Plugging this into Eq. 1.7 and solving for the complex dielectric function ε gives us:

$$\varepsilon = (1 + \chi_e)\varepsilon_0 = \varepsilon_0 + \frac{P}{E} = \varepsilon_0 - \frac{\omega_p^2 \varepsilon_0}{\omega^2 + \mathrm{i}\Gamma\omega}, \tag{1.19}$$

where

$$\omega_p^2 = \frac{n_e e^2}{\varepsilon_0 m_e} \tag{1.20}$$

is the plasma frequency. In the Figure 1.1 the dielectric function of gold is shown. The real part crosses $\varepsilon(\omega_p) = 0$ at the plasma frequency. For high enough frequency $\varepsilon(\omega \to \infty) = 1$ the dielectric function goes to ε_0, and the passing electromagnetic waves behave the same as in free space because the electrons in the metal cannot respond fast enough. The Drude model of dielectric function of metals allows us to model dispersion relation of plasmons. Plasmons are of great importance to the field of plasmonics which we will now introduce.

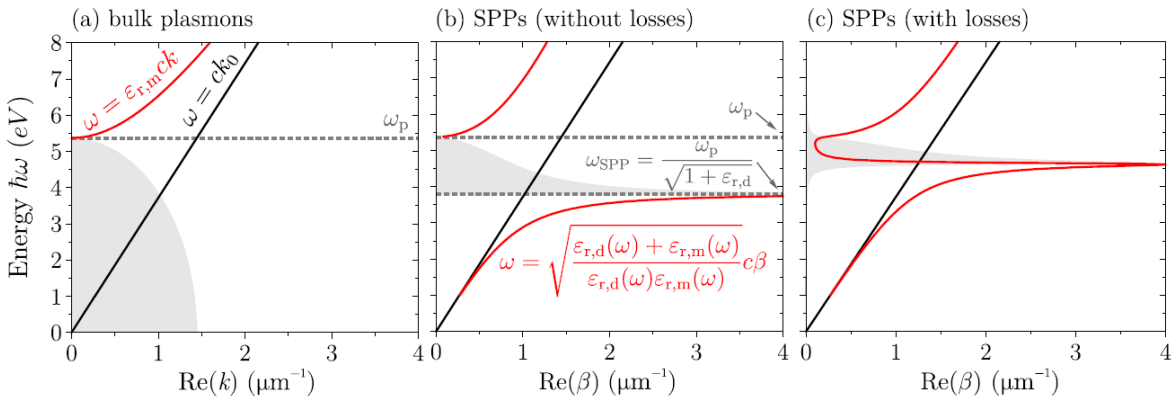

Fig. 1.2: Dispersion relations of plasmons (red lines). The magnitudes of the imaginary parts of the wave vectors are represented by the grey-filled curves. Dispersion relations of waves propagating in vacuum (light lines) are also plotted for reference (black lines). (a) Dispersion relation of bulk plasmons in a metal, which is represented by a lossless Drude oscillator with plasma energy $\hbar\omega_p = 5.37\,\mathrm{eV}$ (which closely corresponds to gold). (b) Dispersion relation of SPPs at the interface between a vacuum and the same Drude material as in (a). (c) SPP dispersion relation for a Drude material with the same $\hbar\omega_p$ as in (a) and (b) but with the additional damping ($\hbar\Gamma = 0.08\,\mathrm{eV}$). Taken from [31].

1.3 Plasmonics

Plasmonics is a scientific field studying collective oscillations of free electron gas called plasmons. Plasmons are responsible for majority of the optical properties of metals and semiconductors. For electromagnetic radiation with frequency above plasma frequency ω_p, metals are transparent because the free electrons in the metal cannot respond fast enough to the incoming electromagnetic radiation. For frequencies bellow the plasma frequency, the free electrons screen the electric field of the light and the material reflects the incoming electromagnetic wave. Since, plasma frequency for metals is usually in the ultraviolet region, metals exhibit high reflectivity in the visible light. Semiconductors have their plasma frequency usually in the deep ultraviolet. Most semiconductors and metals have electronic interband transitions in the visible range which are responsible for their distinct colors.

Photons traveling through medium can couple with bulk plasmons to create bulk plasmon polaritons. Their undampened dispersion relation can be calculated by combining eq. 1.19 with $\Gamma = 0$ and eq. 1.16 to obtain

$$\omega = \sqrt{c^2k^2 + \omega_p^2} = \varepsilon_{r,m} ck, \tag{1.21}$$

where c is the speed of light in vacuum, k is the wave vector of bulk plasmon polariton, ω_p is the plasma frequency, and $\varepsilon_{r,m}$ is the relative permittivity of the medium. This relationship is plotted in the Fig. 1.2(a) and a departure from the light line can be observed. As the frequency decreases, the waves "die–out" all the way to $\omega = \omega_p$ at $k = 0$. On the other hand, as the $k \to \infty$ the photons barely interact with matter and the dispersion relation approaches the light line in vacuum. In the next section we will discuss the main topic of interest of plasmonics, the surface plasmon polaritons.

1.4 Surface plasmon polaritons

By a coupling of a polariton and a plasmon on the interface of two materials with opposing signs of the real part of the dielectric constant, a new quaziparticle is created, the surface plasmon polariton (SPP). When we select material to use, the wavelength of the excitation radiation is crucial. Generally dielectrics have positive values of dielectric constant over visible light, so by analyzing the eq. 1.19 we can deduce that if we use a material with plasma frequency higher than the frequency of our light source, the material will exhibit negative dielectric constant. This is the reason metals are so valuable for plasmonic devices as they exhibit high negative dielectric constant in the visible range.

When excited, SPPs travel across the interface until they are attenuated or radiate their energy away e.g. back into the free space. A schematic of a SPP wave being excited on a periodic grating and traveling across an interface is shown in Fig. 1.3. SPPs have imaginary k_z wavevector perpendicular to the interface, meaning they decay exponentially in the surrounding media. The penetration depth $\delta_{d,m} = 1/k_{d,m}$ defines their confinement to the surface. They exist only in the TM polarization and their dispersion relation can be derived from Maxwell's equations using boundary conditions at the interface as [31]

$$\omega = \sqrt{\frac{\varepsilon_{r,d}(\omega) + \varepsilon_{r,m}(\omega)}{\varepsilon_{r,d}(\omega)\varepsilon_{r,m}(\omega)}}c\beta, \tag{1.22}$$

where β is the propagation constant and $\varepsilon_{r,m/d}$ is the dielectric function of metal/dielectric. The dispersion relation is plotted in the Fig. 1.2(b). The dispersion relation tells us that at low k the SPPs behave like photons. However, as the frequency increases, the dispersion relation asymptotically approaches the "surface plasma frequency" ω_{SPP},

$$\omega_{SPP} = \frac{\omega_P}{\sqrt{1 + \varepsilon_{r,d}}}. \tag{1.23}$$

The real part of the propagation constant is related to the wave length of the SPP wave as $\lambda_{SPP} = 2\pi/\operatorname{Re}(\beta)$ and it's imaginary part is related to its attenuation. First, we need to briefly talk about the propagation length L_{SPP} of SPP waves. As a wave is traveling across an interface, its energy is exponentially decaying along it's propagation direction due to scattering. The propagation length represents the distance the SPP can travel before its energy is decreased to only $1/e$ times the original. We can then describe the propagation length as

$$L_{SPP} = \frac{1}{2\operatorname{Im}(\beta)}. \tag{1.24}$$

For most materials used today in plasmonics, the propagation length is of the order of ten micrometers, limiting the device size built using plasmonic structures to tens of micrometers.

Since, the SPP dispersion lies to the right of the light line, $\omega = \beta c$, the SPP has a shorter wavelength than the excitation radiation. This implies free–space radiation

cannot couple in and out of SPPs as the frequency and momentum must be matched. The only case is for low values of k where the frequencies almost match and thermal vibrations can "bridge the gap". This can occur for radio waves and infrared radiation and is called the Sommerfeld–Zenneck surface wave [32]. For optical frequencies, visible light, special techniques must be utilized which we will be the topic of the next section.

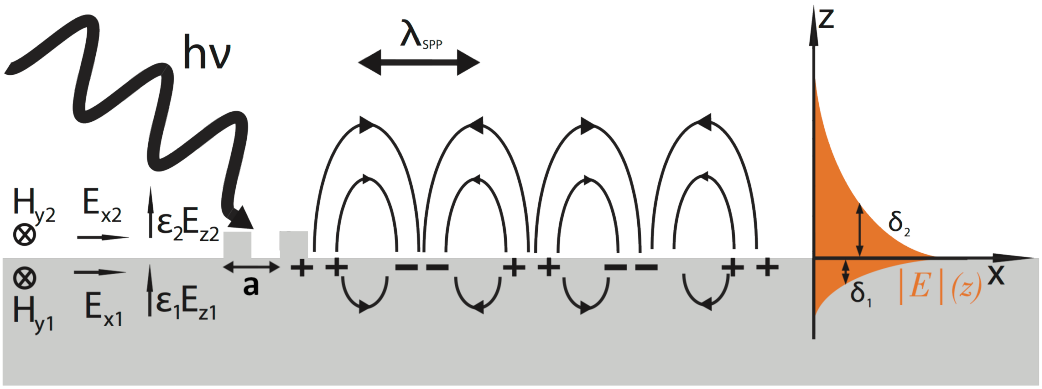

Fig. 1.3: A sketch of a SPP wave being excited by a periodic grating of pitch a and then traveling across an interface of metal (1) and dielectric (2). The exponential decay of $|E|(z)$ illustrates the evanescent character of SPP waves also showing the penetration depths into the material $\delta_{1,2}$.

1.4.1 Exciting and detecting SPPs at optical frequencies

Since, coupling and decoupling of surface plasmons with polaritons is time reversible phenomena, every method of exciting SPPs can be used as a detection method and vice versa. Both energy and momentum of excitation radiation have to be matched. The energy is easy to match as modern lasers can easily produce more than enough illumination, but the momentum is more tricky. This can be achieved by utilizing one these three distinct experimental methods:
1) Frustrated total reflection.
2) Near–field coupling using a probe.
3) Scattering on a metal structure.

Frustrated total reflection

The historically first method used is the frustrated total reflection. Two experimental setups have been developed; (a) Otto [33] and (b) Kretschmann [34] configurations as shown in Fig. 1.4. Both utilize total internal reflection of a laser beam inside a prism. An evanescent electromagnetic wave is formed outside the prism near the reflection spot. A metal surface is brought close ($< 100\,\text{nm}$) to the surface of the prism at the position of the total internal reflection. The wave vector of the evanescent wave is a function of the incoming radiation and the angle under which the laser beam reflects. By scanning the angle, one can find a position at which the reflected light's intensity dips. At this angle the momentum of the evanescent wave is matched with momentum

of the SPP waves on the metal surface and SPP waves are generated which cause energy to flow from the laser beam into plasmons on the surface of the sample.

The detection of surface plasmons happens in the energy loss of the laser beam. The method is well developed and easy to use, so it has many applications in biosensing for quantifying biomolecular interactions [35] and studying living organism by activating fluorophores in cells [36]. The limiting factor is the act of focusing the light source inside the prism which is diffraction limited, so this method cannot achieve super–resolution, so it is not practical for studying plasmonic structures.

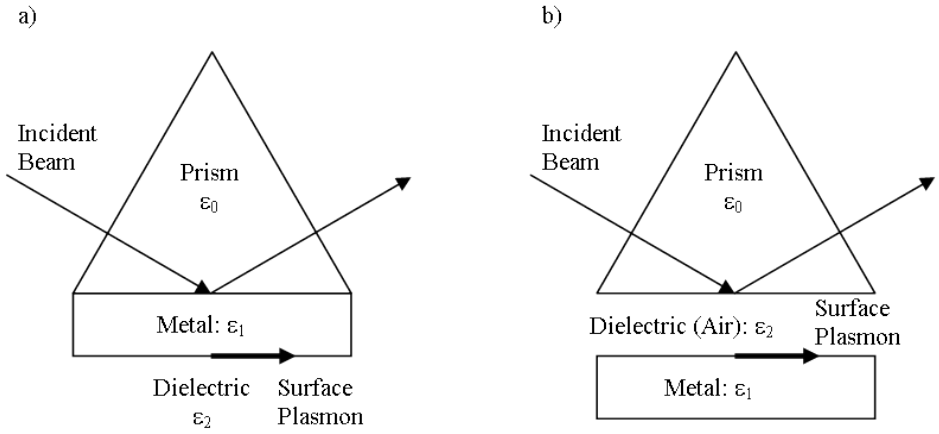

Fig. 1.4: (a) Kretschmann and (b) Otto configuration of a prism coupler for exciting surface plasmon polaritons on metal surface in a attenuated total reflection setup. In both configurations SPPs propagate along the metal/dielectric interface.

Scattering of incident light

Last, but not least, method for detecting and exciting SPP waves is taking advantage of the scattering phenomena of light. As a photon is scattered of a small metal particle or slit, its wave vector can be shortened and can match the wave vector and frequency of SPP waves. While the best method for coupling photons into SPP waves is by scattering off of periodic metal gratings can be around 20% efficient [37], a scattering event on a single slit or a metal structure can still couple up–to 14% of incoming radiation [38]. The advantage of this method is that the metallic structures can be fabricated by lithographic methods at precise location on the sample to induce SPP waves.

The experimental setup for generating SPP waves in this thesis is shown in the Fig. 1.7(b). Gold slits are illuminated by a laser source. Each slit scatters light, so it acts as an electric dipole. SPP waves travel from this dipole along the metal inside the slit to the surface of the sample. Here, they excite new SPPs on the sample's surface which create a standing wave which can be then detected. In this case, a SNOM tip used for the detection as will described in the next section.

SNOM

The scanning near–field optical microscope (SNOM) lends itself as the perfect candidate for high precision SPP generation and detection. The SNOM probe can move with

nanometer precision under 10 nm from the surface which is well inside the near–field of SPP waves. The method can measure 3D topography map along with SPP signal, so it is possible to precisely select a position to excite or detect surface plasmons.

The disadvantage of this method is its slow scanning speed and shallow depth of field. Measuring SPP waves on a $10 \times 10\,\mu\text{m}^2$ chip can take around an hour, and can be only done on flat samples. The setup is also very sensitive to vibrations and the cost associated with it can be quite prohibitive. Next section will delve into more details about this method.

1.5 Scanning near-field optical microscopy

Nowadays, Scanning near-field optical microscope is at the forefront of science and engineering because it opens the gates for studying the nanoworld. Its prowess in nano-sensing comes from combining the advantages of scanning probe microscopy with the power of optical sensing.

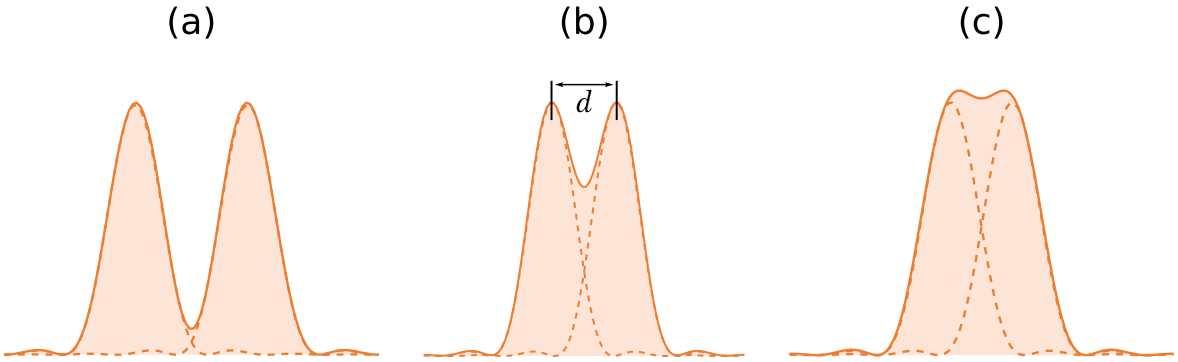

Fig. 1.5: A visual demonstration of the Abbe's diffraction limit $d = \lambda/(2NA)$. Two light sources emitting light at a wavelength λ are observed by a microscope with a numerical aperture NA at varying distance from each other: (a) both points are resolved; (b) the Rayleigh criterion; (c) the points are unresolved.

1.5.1 Studying nanoscale structures

The main characteristics interesting about a nanostructure are its shape and size, molecular structure, chemical composition, and functional properties. To study such structures a high spatial, spectral, and temporal resolutions are required. Classical microscopes excel in regards to spectral and temporal resolving power, but their spatial resolution is limited by Abbe's diffraction limit shown in Fig. 1.5. Using Rayleigh criterion, Ernst Abbe formulated minimal distance d at which can be two separate points emitting light of wavelength λ can be distinguished by an objective with numerical aperture NA.

$$d = \frac{\lambda}{2NA} \tag{1.25}$$

This limits the classical microscopy resolving strength to about a half of the used wavelength. For visible light, the spatial resolution is then around $0.2 - 0.5\,\text{nm}$. While this method is great at parallel imaging, it can never break the super–resolution needed for imaging nanostructures. The three limiting factors of optical microscopy are:
1) Abbe's diffraction limit discussed before.
2) Lens has limited aperture and collects only far–field radiation, thus neglecting the evanescent fields which carry higher frequencies containing more information.
3) Lens receives out of focus light.

Many serial methods have been developed to overcome these limitations such as confocal microscopy, stimulated emission depletion (STED) [39], stochastic optical reconstruction microscopy (STORM) [40], and structured illumination microscopy (SIM) [41]. While these methods can achieve super resolution under 100 nm in the xy plane, they lack the precision in the Z direction, so true 3D imaging is not impossible. The hurdle is that these methods lack the information from the evanescent fields which carry higher frequencies and do not travel into far field. To achieve even higher resolution, we need to consider another approach.

1.5.2 Development of SNOM

In 1909, Sommerfeld described for the first time a radiating dipole oriented vertically. This opened the possibility of coupling a far–field radiation with long wavelength into a much smaller object which would then diffract the light. Following this work, in 1928, Irish scientist Synge proposed an experimental scheme for probing nanoscale resolution. He described an opaque screen with 100 nm wide hole which would serve as a point light source illuminating thin biological sample from less than 100 nm. The sample would scatter light which would be collected on a photodetector. A daring idea at the time which would take almost 60 years to realize [8].

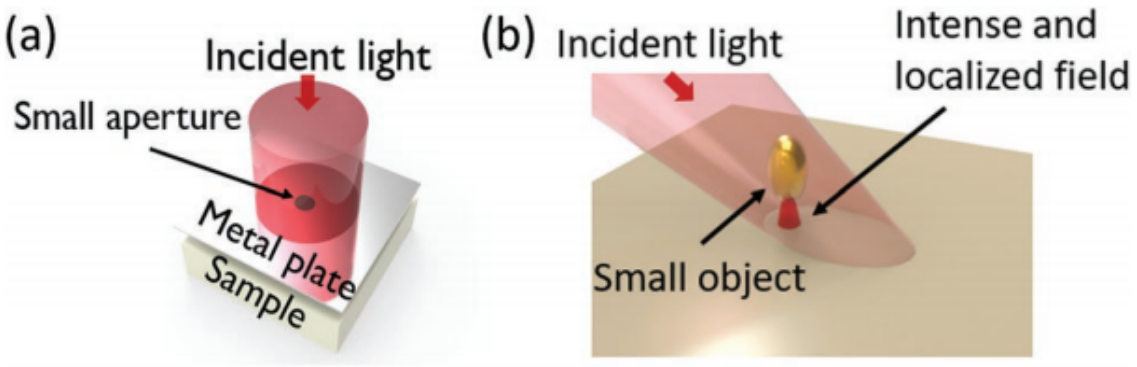

Fig. 1.6: (a) Synge's original concept for overcoming the diffraction limit and achieving an ultrahigh spatial resolution using a small aperture. b) Synge's second concept with a small subwavelength object as light confiner and scatterer. Taken from [42].

A new breakthroughs in technology came with the invention of scanning tunneling microscope in 1981 and atomic force microscope in 1986 by Gerd Binnig et al at IBM Zürich [9]. Now with the technology to safely bring sharp objects close to the surface,

scan them along the surface, and collect positional information, new possibilities emerged. In 1984, Synge's old design was reinvented by Pohl and with Denk and Duerig they demonstrated its functionality at the IBM research institute Rüschlikon [10]. The same year, Lewis and his group developed similar technology at the Cornell University [43]. The setup now relied on an optical fiber with sub–wavelength scale aperture at the tip. This probe was scanned along the surface in a controller way at a constant distance maintained by a feedback loop. Thus aperture scanning near–field optical microscopy was born.

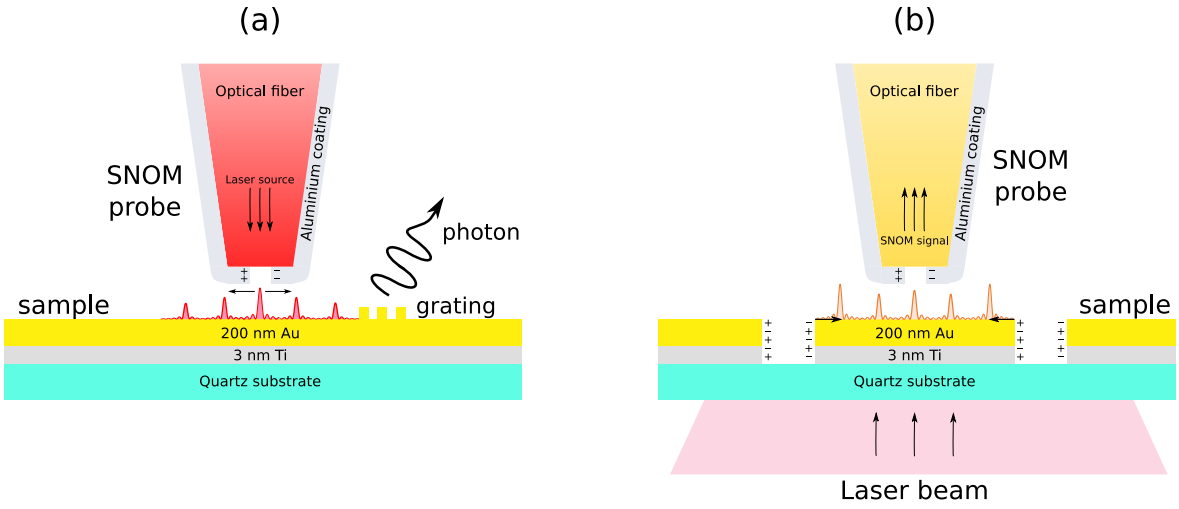

Fig. 1.7: Two experimental setup for measuring with a aperture type SNOM. (a) SNOM probe excites an SPP on the surface of metal which is decoupled from the surface by a periodic grating. The signal is measured in the far–field. (b) Laser source excites SPPs on the surface of a gold film. Here, the SPP waves interfere and create standing waves which can be measured by a SNOM tip close to the surface. The signal is sent via the optical fiber into photo multiplier device.

Aperture type SNOM

As mentioned above, the first type of SNOM developed was the aperture type SNOM (a–SNOM). Nowadays, the basic operation principle is as follows. An optical fiber is etched on one end into a very sharp tip. Then, it is coated with a metal layer and a small aperture ($50 - 250\,\mathrm{nm}$) is drilled into its apex. This probe tip is attached to a quartz crystal tuning fork. This tuning fork was designed for quartz watches, so it is very small and has precise resonant frequency of $32768\,\mathrm{Hz}$. The tuning fork with the fiber end is inserted into a SNOM head with piezo motors inside to allow precise positioning of fiber tip along the surface. The other end of the fiber is attached into a photomultiplier device. When the fiber tip is lowered to the surface of the sample, Van der Waals sheer forces change the resonant frequency of the tuning fork which can be detected by a feedback mechanism to adjust height of the probe. As the probe apex is scanned across the sample, the evanescent field of SPP waves traveling across the sample surface couples into the fiber end. This coupling emits photon down the optical fiber into the photomultiplier device, amplifying the optical signal which can then be

digitized by a CCD chip into a computer. An example measurement scheme is shown in Fig. 1.7(b).

By decreasing the size of the aperture the resolution can be improved, but at a cost of signal–to–noise ratio. This way SNOM can reach lateral resolution up to 20 nm and vertical resolution of 2 nm [44], but the scanning speed can be severely hindered. In science, this is generally not much of a problem, so images of size $10 \times 10\,\mu m^2$ at a resolution of $512 \times 512\,px^2$ are usually measured. Such an image will take around 45 minutes at the integration time of 10^{-2} s/px. Unfortunately, this capture time is actually doubled as the topography data has to measured separately from the SNOM measurement. This is done by double scanning each row, first capturing the topography data and second time detecting SPPs. One problem of a long detection window can be drifting, so this has to be accounted for in extremely long measurements.

As mentioned above, a–SNOM tip can be used also as a SPP wave generator. Such experimental scheme is shown in Fig. 1.7(a). In this configuration, a laser source is coupled into the fiber tip which creates evanescent field at the tip of the probe which can excite SPP on the surface of the sample. These SPPs can activate fluorescent molecules or decouple from surface by a grating producing photons which can be collected in far–field. There are commercially available SNOM devices which can both collect and excite SPP waves in the near–field by using two or four probes.

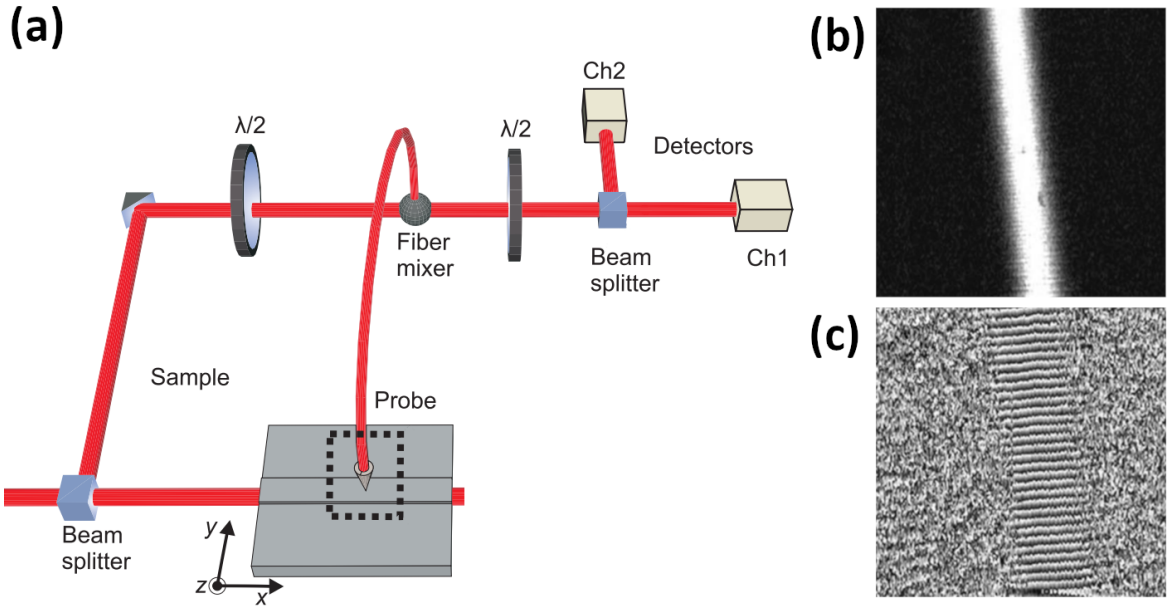

Fig. 1.8: (a) Schematic of the phase-sensitive near-field microscope. The near-field probe, indicated by the dashed box, is scanned 20 nm above the sample and collects the evanescent field of the light inside the waveguide. The light is mixed with light from a reference branch. The resulting light is split by a polarizing beam–splitter, and the two orthogonal polarizing components are detected with a heterodyne scheme. By suitably choosing the orientation of the two l/2 waveplates, we can relate the signal at the two detectors, called Ch1 and Ch2, with the fields present in the sample. Taken from [45]. (b) a–SNOM $10 \times 10\,\mu m^2$ near–field image of a buried ion–exchange waveguide. (c) Image taken by a–SNOM heterodyne setup measuring phase of the waveguide shown in (b). Taken from [46].

Aperture type SNOM works with wide range of electromagnetic radiation from 200 to 2000 nm. This offers wide variety of uses by coupling it with other methods such as Fourier-transform infrared spectroscopy (FTIR) [47], tip–enhanced Raman spectroscopy [48], and fluorescent microscopy [49]. Also, it is possible to measure near–field phase using a heterodyne a–SNOM setup [45]. Such system is shown in Fig. 1.8(a). This heterodyne SNOM can measure both electric and magnetic component of SPP waves. It can also detect phase by mixing the collected signal with the SNOM head with the reference signal traveling in the reference arm of the setup. While this method is suited for detecting phase of wave–guides as shown Fig 1.8(b), it is not a true near–field holographic since the interference happens in the far–field. In the last chapter, we will present a true near–field method of detecting phase of the SPP waves, but first we will describe another SNOM technique which can extract phase information.

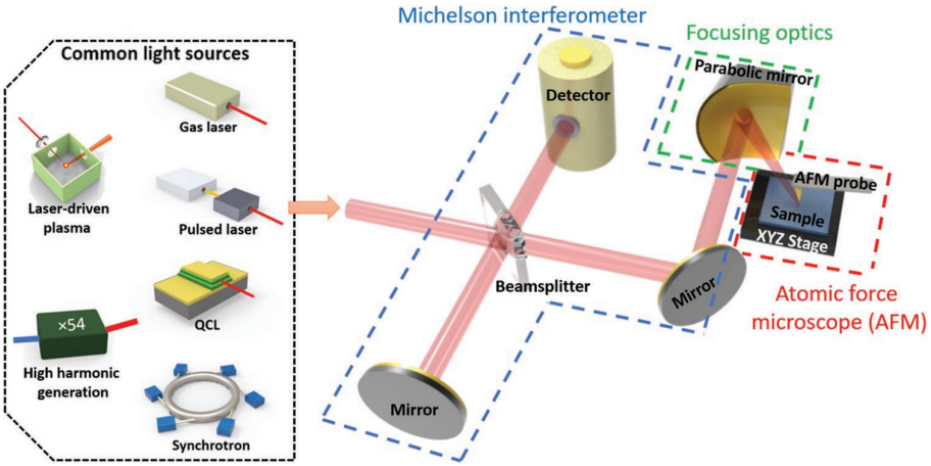

Fig. 1.9: A typical s-SNOM setup with visible or IR light sources. For completeness, a THz CW source, with high-harmonic generation using a microwave, is included. Taken from [42].

Scattering type SNOM

Another type of SNOM started to be developed in the late 1990s. First pioneer work utilizing scattering-type SNOM (s–SNOM) was done by Lahrech et al. in 1996. [50] They could image gold grating and gold surface at impressive $\lambda/100$ resolution. Early 2000s experienced a significant progress in probe microscopy, and provided the foundation for today's s–SNOM in the work of Hillenbrand et al [51]. The modern s–SNOM utilizes non–contact atomic force microscopy (nc–AFM) for imaging the near–field.

A typical setup of s–SNOM is shown in Fig. 1.9. Basic principle is that a laser source is split via beamsplitter in a Michelson type interferometer into reference and probing arms. In the probing arm, the laser beam is focus usually by a parabolic mirror on an apex of a AFM probe. This probe is generally made of silicon, either non-coated or coated in metal, and is oscillating above the surface of the sample in tapping mode. The laser beam focused on the probe creates a large field enhancement near the probe's tip. This produces a scattered optical signal which is then collected by a parabolic mirror and directed back into the Michelson type interferometer where it is analyzed.

The main advantage over a–SNOM lies in the increased resolution for longer wavelengths of radiation. Theoretically, a–SNOM can decrease the resolution arbitrarily by decreasing the aperture hole. But, in practice, due to low signal to noise ratio and the wave–guide cut-off effect, the resolution is constrained to $\approx \lambda/10$ [52]. This implies that for terahertz regime the resolution is limited to $1\,\mu$m which prohibits nanoscale imaging. However, s–SNOM is not limited by the wavelength used, but only by the radius of curvature of the apex of the tip [53]. This is why s–SNOM is so popular for THz spectroscopy.

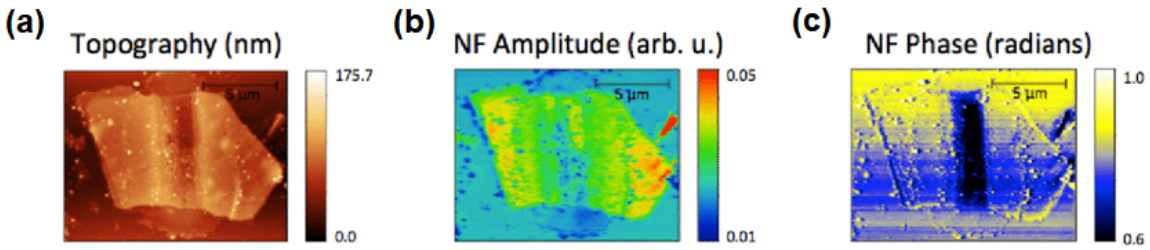

Fig. 1.10: s-SNOM measurement of a $MoTe_2$ structure. Scan images of the (a) topography, (b) near-field amplitude, and (c) the near-field phase. Taken from [54].

Another use of s–SNOM is to extract phase information of near–field. The reference arm mirror of the Michelson interferometer is usually oscillating at a frequency of the AFM probe. This creates a feedback loop which allows the operator to filter desired signal. In practice, the mirror is oscillating at higher harmonic frequencies as the probe's own feedback loop might be interfering with the measured signal. Subsequently, the interferometric setup allows both phase and amplitude to be recorded at the same time creating a hologram. A measurement where topography, near–field intensity and phase are recorded is shown in Fig. 1.10. This makes the s–SNOM a crucial tool for studying plasmonic nanoantennas [55], SPP waves on graphene [56], and nano-FTIR [57].

1.5.3 Fabrication of a–SNOM tips

Nowadays, there are many commercial types of SNOM probes available. It is pivotal for the SNOM tip to well defined and free from any morphological defects to measure the near–field with high signal–to–noise ratio. While it is possible to buy SNOM tips, the variety of sizes, materials, and shapes limited, and their price of $(100 - 200\ €)$ is rather prohibitive. So, fabricating SNOM tips in–situ can be desirable. The fabrication process to create the tips used in this thesis consists of four fabrication steps:
1) Chemical wet etching.
2) Focused ion beam (FIB) dry etching.
3) Metal coating using ion beam sputtering (IBS).
4) Drilling an aperture using FIB.

The SNOM tips utilized in this thesis were fabricated by Jan Krpenský in the laboratories of the Institute of Physical Engineering at Brno University of Technology and in the cleanrooms of CEITEC Nano.

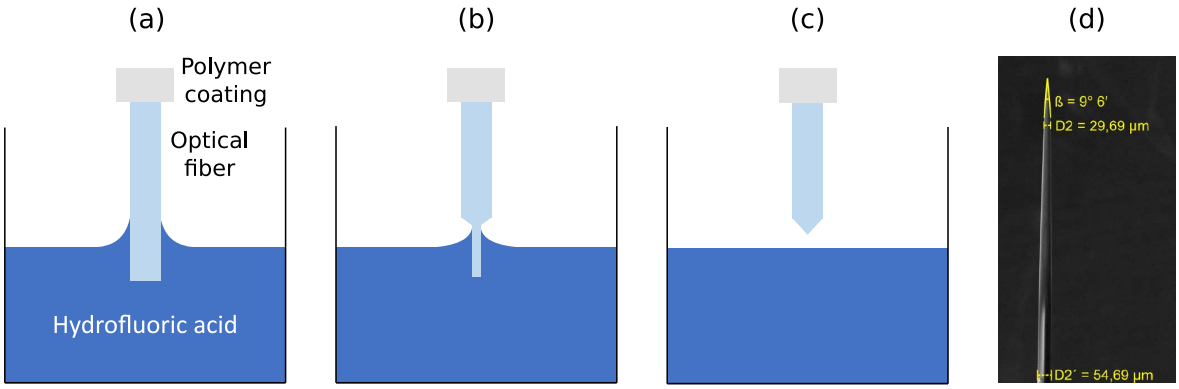

Fig. 1.11: Chemical etching of a optical fiber. (a) The optical fiber tip is inserted into 48% hydrofluoric acid. (b) Etching in progress. (c) Etching is finished and a sharp tip is formed. (d) Fiber tip after etching. Taken from [58].

Chemical wet etching

First step of the tip fabrication process is the chemical etching of an optical fiber. This step is necessary to create sharp tip with well defined edges. The optical fiber used is 630HP from Thorlabs. The core of this fiber has a diameter of 125 μm and is optimized as a single–mode for $600 - 800$ nm. This suits out setup where we have implemented He–Ne laser ($\lambda = 638.8$ nm).

First, the polymer coating which protects the fiber from breaking is removed from the last 2 mm of the fiber. This leaves the fiber end vulnerable, so care must be taken to ensure the fiber tip is not hit from this point on. Second, exposed tip is inserted into 48% hydrofluoric acid for 50 minutes. The acid creates a meniscus around the fiber and slowly etches the fiber. As the fiber tip narrows, the meniscus decreases until it falls off leaving a sharp tip. This method of fabricating SNOM fiber tips is called modyfied Turner method [59] and is shown in the Fig. 1.11(a-c). In the original patent, Turner used an oil layer flowing on the acid to suppress evaporation of the acid, however, we left the acid exposed, so its vapors further etch the fiber into even sharper tip. The final etched fiber tip is shown in the Fig. 1.11(d). Next, the fiber tip has to be dry etched using FIB to smooth out imperfections and taper off the fiber end.

Focused ion beam (FIB) dry etching

This is the most time consuming step because the tips have to loaded into the FIB one by one and the FIB requires careful calibration for each tip. Fig. 1.12(a) shows the fiber end before FIB etching imaged by electron microscope. First, the pinnacle of the fiber tip is cut perpendicular to its rotational axis to create a truncated cone at the end. This is the best shape of the fiber end for transmitting light waves. Second, the fiber end is rotated to face the ion beam. Then, ion beam is turned on for a brief moment to smooth out the fiber exit and the sides of the conical end. The sides etch faster than the flat surface at the tip, so the imperfections are blasted off quickly. Fig. 1.12(b) shows the fiber end after FIB etching. Now the tips are prepared to be coated by a metal layer.

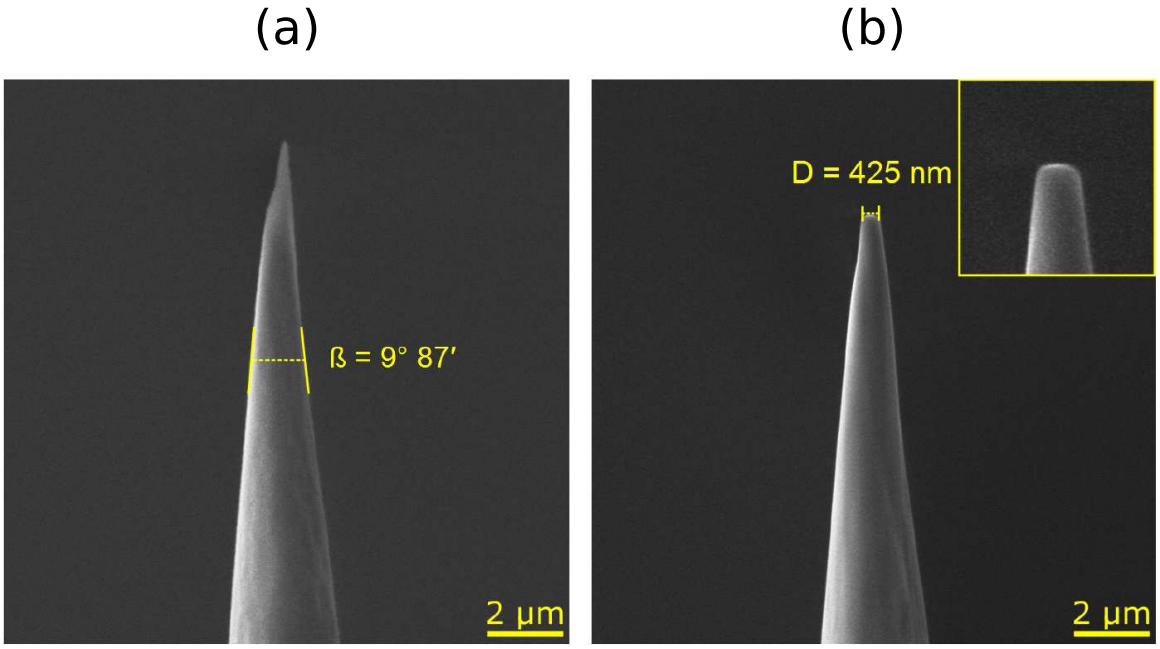

Fig. 1.12: FIB dry etching of a optical fiber imaged in an electron microscope. (a) A fiber tip before etching. (b) Finished tip after truncating the end and FIB cleaning. Taken from [58].

Metal coating using ion beam sputtering

The etched tips have now tapered conical shape with 10° angle at the end. Now, the whole naked fiber tip has to be covered in metal to reduce signal loses and prevent damage to the fiber. For this purpose, ion beam sputtering is utilized to coat the tip in gold. The fiber tip is placed into a vacuum chamber with a gold target. A thermal emission cathode ionizes argon gas. The argon ions are then accelerated towards the gold target where they impact the surface. This sputters gold particles on the sample which is slowly coated by an gold layer. During this process the fiber tip is rotated to allow it to be coated from all sides evenly. This continues until a layer of 130 nm of gold is built. Now the tip is completely enclosed in metal from all sides, so an aperture must be made to allow SNOM measurements.

Aperture drilling using FIB

Lastly, a small aperture must be drilled into the fiber end. Here, a focused ion beam is again utilized. A circular aperture with the diameter of $d = 100\,\text{nm}$ is milled through the metal coating. This circular slit will serve to collect or excite near–field radiation. One of its uses is to measure standing electromagnetic waves on on–chip interferometers which will be discussed in the next chapter.

2. INTERFEROMETRY

Interferometry is a family of measurement methods utilizing the phenomenon of interference of waves (usually electromagnetic, sound or seismic waves). The application of these methods can be found in many fields of science and engineering. In this chapter, we will focus on the interference of electromagnetic and surface plasmon polariton waves. First, let's describe the theory of interference.

2.1 Interference

When two or more waves of the same type propagate into one point of space, they form a new wave whose amplitude at this point is a vector sum of phasors of each wave. This is the principle of superposition of waves. When two waves with identical amplitudes and which are coherent, meaning they have the same frequency, occupy the same space then constructive resp. destructive interference occurs depending on whether the phase difference between them is an even resp. odd multiple of π. Images produced via interference are called interferograms.

Since light consists of electromagnetic waves visible to human eyes, it experiences interference by the principle of superposition of waves. The ideal case of interference assumes a single frequency of light beams. This is not practical as it would require the wave to be infinite in time. As long as the frequency of the waves does not change over finite duration then the two waves can interfere over that period. Nowadays, laser sources approximate monochromatic source the best and are most commonly employed to generate interference fringes. To understand interferometric devices, we first need to explain the basics of interference.

2.1.1 Two-wave interference

In this thesis, we focus on interferometric instruments utilizing interference of two coherent electromagnetic waves to extract useful information about physical systems. Here, we derive equations which govern their interaction.

The time dependent phasor $A(\mathbf{r},t)$ and intensity $I(\mathbf{r})$ of an electromagnetic wave are

$$A(\mathbf{r},t) = A_0(\mathbf{r})e^{\mathrm{i}[\varphi(\mathbf{r})-\omega t]} \tag{2.1}$$

and

$$I(\mathbf{r}) = \frac{1}{T}\int_0^T A(\mathbf{r},t)A^*(\mathbf{r},t)\mathrm{d}t, \tag{2.2}$$

where A_0 is its maximum amplitude, φ the phase, and ω the frequency. When two monochromatic waves interfere at a point $\mathbf{r}$, the amplitude of the resultant wave U the superposition of both waves is given by

$$U(\mathbf{r},t) = A_1(\mathbf{r})e^{\mathrm{i}[\varphi_1(\mathbf{r})-\omega t]} + A_2(\mathbf{r})e^{\mathrm{i}[\varphi_2(\mathbf{r})-\omega t]} \tag{2.3}$$

Practically, it is only possible to measure the intensity of light I because the frequency ($\sim 10^{14}$) is too high for modern detectors such as CCD chips. Combining equations 2.2 and 2.3 we arrive at

$$I(\mathbf{r}) = I_1(\mathbf{r}) + I_2(\mathbf{r}) + 2\sqrt{I_1(\mathbf{r})I_2(\mathbf{r})}\cos(\phi(\mathbf{r})), \tag{2.4}$$

where $\phi = \varphi_1(\mathbf{r}) - \varphi_2(\mathbf{r})$ is the relative phase difference between the two propagating waves. These equations hold for any point of space where two waves meet, so now we will discuss what happens when two waves interfere in a closed region of space.

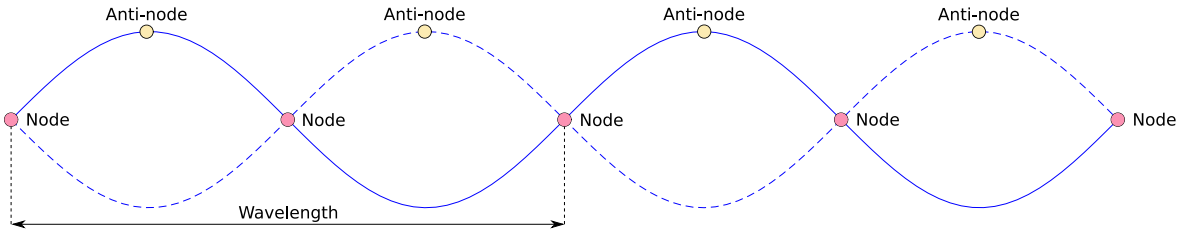

Fig. 2.1: A standing wave at 1/4 (full line) and 3/4 (dashed line) of its periodic oscillation. Wavelength of the original waves is shown.

2.1.2 Standing waves

One fateful day in 1831, Michael Faraday was doing an experiment with water in a vibrating container. Suddenly, he noticed a strange pattern emerge from the vibration on the surface. The water stopped moving almost frozen in a wave like pattern [60]. This was the first known discovery of standing waves.

Regardless of their late discovery, standing waves play an important role in all of our daily lives. They are responsible for a variety of resonance effect such as in musical instruments creating harmonics, optical cavity resonators e.g. Fabry–Pérot inferferometer, and even at geographic scales they can appear in seismic waves or create air currents in the atmosphere.

Standing waves appear every time two waves with the same frequency and amplitude travel in the opposite directions. Here, we will derive their basic properties for sinusoidal waves one dimension, but their description can be extended into more complex systems in 2D or 3D though it is outside of the scope of this thesis.

First, we write equations for two sinusoidal waves traveling in along x–axis with

the same maximum amplitude A_0, frequency ω, and wavelength λ, but in the opposite direction. Their time dependent amplitudes $y_{1,2}(x,t)$ will equal to

$$y_1(x,t) = A_0 e^{-\mathrm{i}(\omega t - kx)}, y_2(x,t) = A_0 e^{-\mathrm{i}(\omega t + kx)}, \tag{2.5}$$

where $k = 2\pi/\lambda$ is the wave vector of the waves. At each point they meet they interfere, so the amplitude of the resultant wave $y(x,t)$ will be

$$y(x,t) = y_1(x,t) + y_2(x,t) = 2A_0 \cos(\frac{2\pi}{\lambda}x)e^{-\mathrm{i}\omega t} = A_m(x)e^{-\mathrm{i}\omega t}. \tag{2.6}$$

This equation describes a wave which exhibits temporal oscillations, but is spatially stationary. Each point along the x–axis has the same maximum amplitude $A_m(x) = 2A_0 \cos(\frac{2\pi}{\lambda}x)$. This implies the resultant wave has at even multiples of a quarter wavelength points along the x–axis called nodes where the maximum amplitude is always zero $A_m = 0$ and anti–nodes with maximum amplitude equal to $A_m = 2A_0$ at odd multiples of a quarter wavelength. The wavelength of two neighboring nodes or antinodes will be at half the wavelength of the original waves. The basic principle is shown in the Fig. 2.1.

Their significance for plasmonic holography becomes apparent when their capturing method is considered. Intensity of SPPs is measured in finite time, so eq. 1.11 tells us it is only their maximum intensity $A_m(\mathbf{r})$ is what determines the SPP signal strength. After all, surface plasmons travel at speeds much higher than a SNOM tip can capture their intensity. Relative to them it is frozen in time. Here, standing waves come into play. If we excite standing waves of SPPs, the spatial location of nodes and antinodes will be fixed, and we can measure them using SNOM. This method will acquire only amplitude information of the SPP standing waves. To get more information about the surface plasmon polaritons, we have to also acquire their phase. Extraction of phase is no easy topic, so we will explain its basic principles in the next section.

2.2 Optical interferometers

An optical interferometer is an important tool for quantitative and qualitative characterization of micro- and nanostructures utilizing the interference of light. Source light beam is split via a beam-splitter into objective and reference paths of the interferometer. The objective arm contains the studied sample which creates a phase shift in the light beam traveling through it. Both beams are then combined to create an interferogram. An important requirement of a functional interferometer is to have sufficiently coherent source, so that the coherence length is longer than the optical path difference of the two arms. Nowadays, this is not a big problem in table sized apparatus as lasers have typical coherence length of $10 - 30\,\mathrm{cm}$. However, with more complicated setups and precise measuring techniques, incoherent light can be made to interfere which can increase the resolution of the microscope and provide more information about the studied sample by reducing the coherence noise, eliminating certain artifacts, and increasing the lateral resolution [61].

2.2.1 Types

Nowadays, the two most commonly used interferometers are Michelson and Mach-Zehnder. Michelson interferometer is well suited for studying opaque materials with good reflectance. The schematic of its configuration is showed in Figure 2.2(a). However, for transparent samples it is best to utilize Mach-Zehnder interferometer which is shown in Figure 2.2(b). The key aspect is that the sample can be illuminated and the transmitted or reflect light can be collected using variety of different instruments. Objectives, fiber tips, SNOM tips, and lenses can all be used as collection and illumination devices.

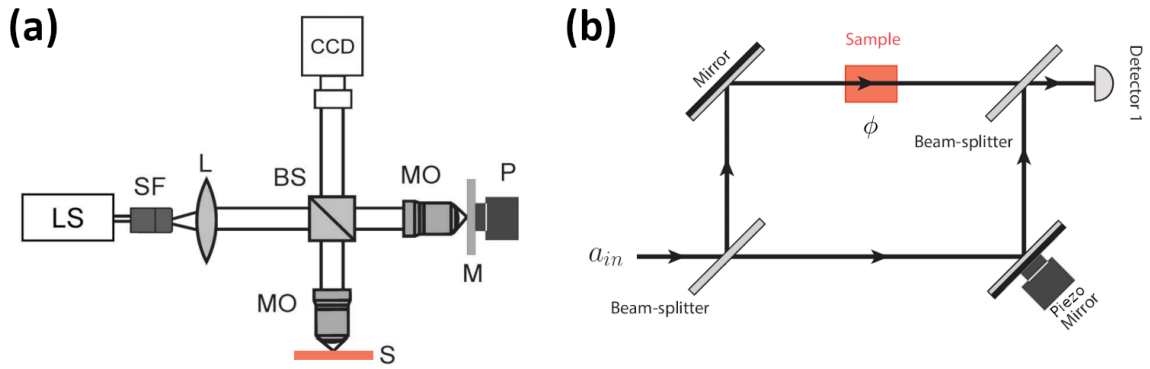

Fig. 2.2: (a) Modified Michelson interferometer setup for phase-shifting digital holographic microscopy [LS, light source; SF, spatial filter; L, lens; BS, beam splitter; M, mirror; MO, microscope lens; P, piezo actuator; CCD, digital image recording device (CCD camera)]. Taken from [62]. (b) Standard Mach-Zehnder setup for in-line phase-shifting digital holography. [a_{in}, input light source; ϕ, sample induced phase shift]

2.3 Extracting holograms

Since an interferogram is captured typically on a CCD chip where each pixel integrates over many wave cycles and therefore lacks the phase information. Each digitized measurement is only the amplitude information of the desired hologram. To construct a full hologram, more advanced techniques must be utilized. These include phase shifting algorithms, spatial synchronous capture, Fourier methods, or using micropolarizer arrays. Phase–shifting interferometry (PSI) is the most easy to implement, but suffers the most from temporally induced phase–shifting errors. The other methods can capture full hologram in single shot, but are harder or more expensive to implement while suffering from other induced errors.

2.3.1 Phase–shifting holography

To extract a hologram, both phase and intensity information, from several interferograms additional techniques must be utilized. The interferometer measures only intensity I in the equation 2.4, but the equation has 3 variables: I_1, I_2, and ϕ. This can be solved by adding an optical delay component in either arm of the interferometer,

which imposes a known phase-shift to the light traveling through it. Modifying eq. 2.4, substituting $I_{dc}(\mathbf{r})$ for $I_1(\mathbf{r}) + I_2(\mathbf{r})$ and $I_{ac}(\mathbf{r})$ for $2\sqrt{I_1 I_2}(\mathbf{r})$, and adding a term for a known phase shift δ, we obtain a simplified equation

$$I(\mathbf{r}) = I_{dc}(\mathbf{r}) + I_{ac}(\mathbf{r})\cos(\phi + \delta). \tag{2.7}$$

To extract ϕ, we need at least 3 measurements of $I(\mathbf{r})$ for different values of δ. The most commonly used algorithms employ phase shift of $\delta = n\pi/2$, where $n = 0,1,2,3,4....$ This is achieved by a moving piezoelectric mirror in on of the arms of the interferometer while capturing images. For a five-step algorithm, the intensity of each pixel in each interferogram is then described as:

$$I_1(\mathbf{r}) = I_{dc}(\mathbf{r}) + I_{ac}(\mathbf{r})\cos(\phi), \tag{2.8}$$

$$I_2(\mathbf{r}) = I_{dc}(\mathbf{r}) - I_{ac}(\mathbf{r})\sin(\phi), \tag{2.9}$$

$$I_3(\mathbf{r}) = I_{dc}(\mathbf{r}) - I_{ac}(\mathbf{r})\cos(\phi), \tag{2.10}$$

$$I_4(\mathbf{r}) = I_{dc}(\mathbf{r}) + I_{ac}(\mathbf{r})\sin(\phi), \tag{2.11}$$

$$I_5(\mathbf{r}) = I_{dc}(\mathbf{r}) + I_{ac}(\mathbf{r})\cos(\phi). \tag{2.12}$$

While the phase ϕ can be calculated from only three images, more steps reduce the phase shifting errors. Also, it is true that $I_1 = I_5$ in theory, but in practice, due to phase shifting errors and static noise, adding the fifth step increases the precision of the calculation. By combining all five equations together and solving for ϕ we obtain:

$$\phi = \tan^{-1}\left(\frac{2(I_2 - I_4)}{2I_3 - I_5 - I_1}\right). \tag{2.13}$$

This algorithm is known as *Schwider-Hariharan algorithm* [63] for which an error due to a 5% incorrect phase shift is reduced by a factor of 25 compared to only 3–step algorithm. [64]

2.3.2 Off-axis holography

The next common method for extracting phase information from an interferogram is the off-axis holography. The method is implemented by introducing a high tilt between the reference and objective beams. This creates tilt fringes in the interferogram at spatial frequency f which separates the wavefront phase information in Fourier space. To extract phase, the captured interferogram is Fourier transformed and then spatially filtered around the frequency f. An inverse Fourier transform on the filtered signal gives the phase of the wavefront. A schematic of an off–axis holographic microscope is shown in Fig. 2.3.

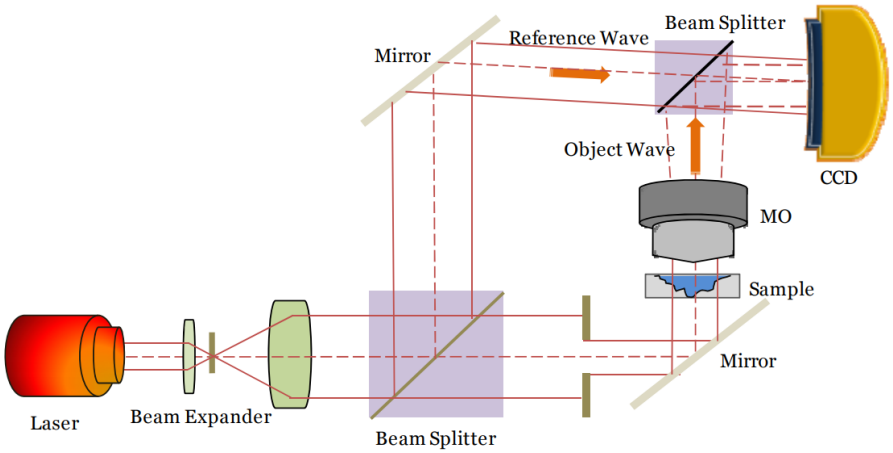

Fig. 2.3: Schematic of a off–axis digital holographic microscope. Taken from [65].

2.3.3 Phase shifting errors

Every interferometric measurement utilizing phase–shifting methods is going to have phase shifting errors in the output data. Most common errors include quantization errors, source instabilities, detector nonlinearity, incorrect phase shifts, vibrations, and stray reflections. Issues like spatial intensity variation and pixel–to–pixel non uniformity do not contribute to the phase error function because phase is calculated on pixel basis, and is therefore independent of it's neighbors. The error is generally represented as a phase error $\Delta\phi$ or as root mean square (RMS) phase error σ_ϕ.

Quantization errors

When capturing interferograms into computer, they have to be converted from analog signal to digital input. The conversion will erase some data depending on the number of bits used to represent the measured data. The following equation describes the relationship between RMS phase error $\sigma_{\phi,B}$, number of bits used B, and number of steps used for the algorithm N:

$$\sigma_{\phi,B} = \frac{2}{2^B\sqrt{3N}}. \tag{2.14}$$

Source instabilities

When the light source has not stable frequency, mismatched optical paths will create phase shift error. When the free space distance of both arms is different by d and the frequency change of the light source is $\Delta\nu$, then its associated phase error $\Delta\phi_{freq}$ equals

$$\Delta\phi_{freq} = 2\pi\frac{d}{c}\Delta\nu, \tag{2.15}$$

where c is the speed of light in free space.

Second possible source instability is the irradiation fluctuation. If the signal to noise ratio is SNR and the number of steps of the algorithms is N, then the mean square

phase error $\sigma_{\phi,I}$ is

$$\sigma_{\phi,I} = \frac{1}{SNR\sqrt{N}}. \tag{2.16}$$

Detector non–linearity

The phase shifting algorithms expect the data to be recorded by a linear function. Special care has to be taken to adjust exposure settings to prevent over– or underexposure. Fortunately, nowadays, most detectors operate in almost strictly linear over their whole dynamic range, so this error is negligible in PSI.

Incorrect phase shifts

When the phase shifting algorithm is not calibrated precisely, a linear phase shift error appears with twice the frequency of original interference fringes. This error can be reduced by adding more steps to the algorithm. If the miscalibration is around 5% then going from 4 to 5 steps reduces the error by factor of 25 [64].

Linear phase error is described by the average phase shift between frames A. When using Schwider-Hariharan algorithm with 5–steps, the average phase shift on each pixel is

$$A(x,y) = \cos^{-1}\left[\frac{1}{2}\frac{I_5(x,y) - I_1(x,y)}{I_4(x,y) - I_2(x,y)}\right]. \tag{2.17}$$

Using this algorithm we can construct a histogram of values of A. The position of peak of the histogram detect incorrect phase shifts between frames.

Vibrations

Since phase shifting interferometry (PSI) operates over a time interval, it is very sensitive to phase shifts induced by vibration. The advantage of high precision in PSI is also its main hindrance as even small change of lengths can induce large phase shift errors in the interferogram. Great care must be taken to eliminate source of vibrations in any interferometric setup and algorithms must be designed to operate over the shortest time period possible. These methods can be quite expensive in terms of equipment and electronics. It is also possible to capture all data in single shot to reduce vibrations, but the setups for these techniques are difficult to build, expensive, and hard to calibrate.

Stray reflections

The large coherent length of lasers in common interferometer setups are both a blessing and a curse. Thanks to them, we can separate objective and reference arms by large distances and still produce interference fringes. However, this also poses a challenge as any stray reflection of the components of the interferometer will interfere with the image at the detector. This can produce large phase–shifting errors. The stray reflections must be either blocked or a low coherence source must be used to eliminate them. Fortunately, they do not contribute to the following phase detection method.

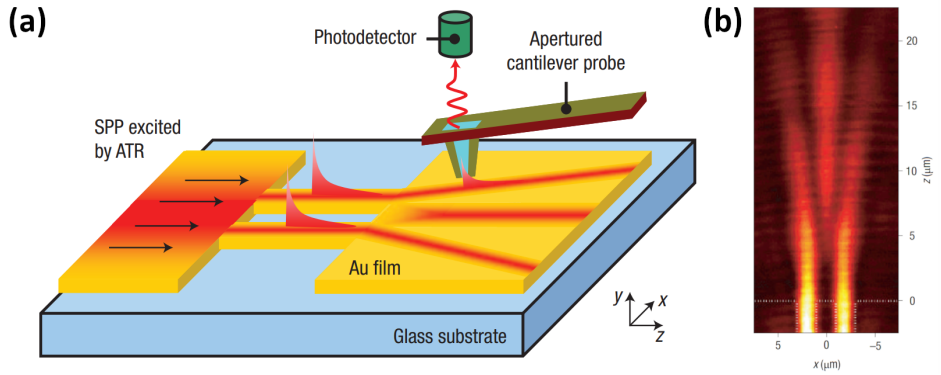

Fig. 2.4: (a) Schematic of an experimental configuration in which a photon scanning tunnelling microscope (PSTM) is used to visualize Young's double-slit experiment for SPPs. The SPPs are first launched along the surface of a patterned Au film (on the left) by an attenuated total reflection (ATR) technique. These SPPs then excite the guided polariton modes supported by two adjacent metal stripe waveguides. These stripes perform an analogous role to the slits in the traditional Young's doubleslit experiment. An apertured cantilever probe is used to locally tap into the guided SPP waves and scatter light towards a photodetector in the far field. The detected signal provides a measure of the local field intensity just under the tip and the propagation, diffraction and interference of the SPPs can be imaged by scanning the tip over the patterned metal. (b) Experimental near-field image taken with a PSTM demonstrating guided polariton propagation, diffraction, and interference for the structure shown in (a). Taken from [66].

2.4 Surface plasmon polariton interferometry

Surface plasmon polaritons introduced in the last chapter are electromagnetic surface waves coupled to a free electron gas confined to a metal–dielectric interface. SPPs exhibit high vertical confinement to the surface as their electric field components extend only $\approx 100\,\text{nm}$ into the surrounding materials. This lateral confinement lends SPPs their surface sensitive properties. Like other waves in nature, they scatter off of defects, diffract around nanostructures, and exhibit interference patters by interfering with each other [67]. This high sensitivity to surface conditions is why they are explored for use in novel sensors [68], enhanced spectroscopy [69], and on–chip interferometers [70]. Let's discuss an interference of two SPP waves.

2.4.1 Interference of SPP waves

Surface plasmon polaritons exist only in TM polarization, so their electric field $\mathbf{E}$ is composed of a out–of–plane component $\mathbf{E}_\perp$ and a in–plane component $\mathbf{E}_\parallel$. Wherever SPP waves interact, their respective electric field components interfere with each other giving rise to patterns similar to that of interfering waves on a surface of water. To understand their wave–like properties, we can use Young's double–slit experiment as shown in Fig. 2.4(a). In Fig. 2.4(b) two SPP waves are propagating in a z direction. From $z = 5\,\mu\text{m}$ to $z = 15\,\mu\text{m}$ distinct interference pattern can be observed with a maximum intensity in the middle and two 1st order maxima traveling at an angle.

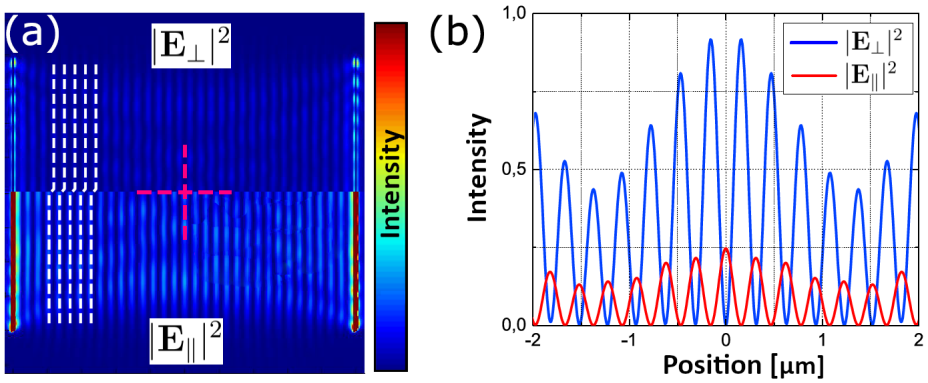

Fig. 2.5: (a) Comparison of interences made by $\mathbf{E}_\perp$ and $\mathbf{E}_\parallel$ by FDTD simulations on two parallel slits. The π phase shift between two is easily spotted. (b) A cross section taken through both interferograms. Taken from [71].

As our–of–plane component $\mathbf{E}_\perp$ and a in–plane component $\mathbf{E}_\parallel$ electric field interfere separately, they create different interference patterns from each other. This can be seen in the interference pattern made by two opposing vertical slits. As seen in the Fig. 2.5, the phases of $\mathbf{E}_\perp$ and $\mathbf{E}_\parallel$ are shifted by a $\lambda_{SPP}/4$, so that the minima of $\mathbf{E}_\parallel$ lies in the maxima of $\mathbf{E}_\perp$. Another important fact is that the maximal intensity of $\mathbf{E}_\parallel$ is usually much weaker than $\mathbf{E}_\perp$. Combined with the fact that SNOM tips commonly used couple much better with $\mathbf{E}_\perp$ explains why in our measurements, the phase images always correlate better with the phase simulations of $\mathbf{E}_\perp$.

These experiments confirm that SPP waves undergo both diffraction and interference as classical 2D waves, and can be used for holographic measurements which we will discuss in the next section.

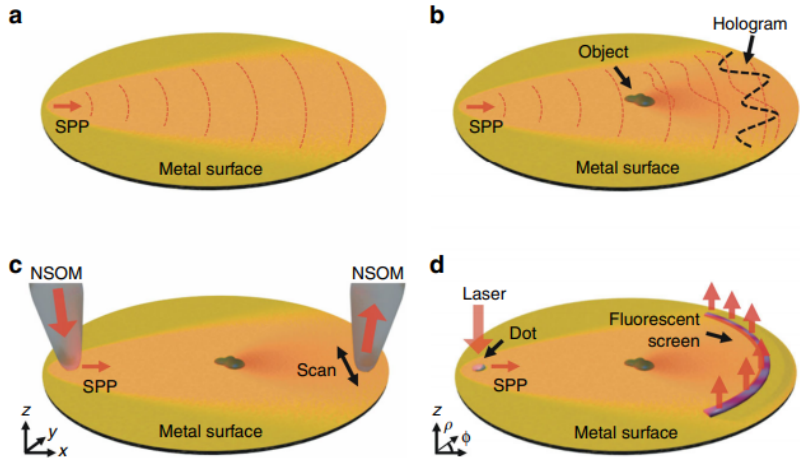

Fig. 2.6: (a) A plasmon reference wave propagates over a surface and (b) interacts with micro-objects forming the scattered object wave. The object wave interferes with the reference wave forming a plasmonic hologram. The hologram is accessed via (c) a dual-probe NSOM system or with (d) a fluorescent screen. Taken from [70].

2.4.2 SPP holography

The SPP wavefont is very sensitive to distortions by an objects on the metal–dielectric surface. This knowledge can be exploited for developing a SPP holographic microscope. This device would, just as a classical holographic microscope, send an objective wave modified by a studied object and then combined with a reference wave. By capturing their interferogram, the original image could be digitally reconstructed. This device would enable studying nanostructures under the diffraction limit with uncanny precision. The most used method for extracting holograms of SPP waves is the phase–shifting interferometry. Different methods for inducing phase–shift have been proposed. A simple configuration using lateral shifting of detecting probe for capturing SPP holograms is described in Fig. 2.6. Another possibility is to use heterodyne SNOM. Heterodyne SNOM collects light in the near–field and then interferes it with the far–field reference. This means it requires expensive and precise setup to minimize noise.

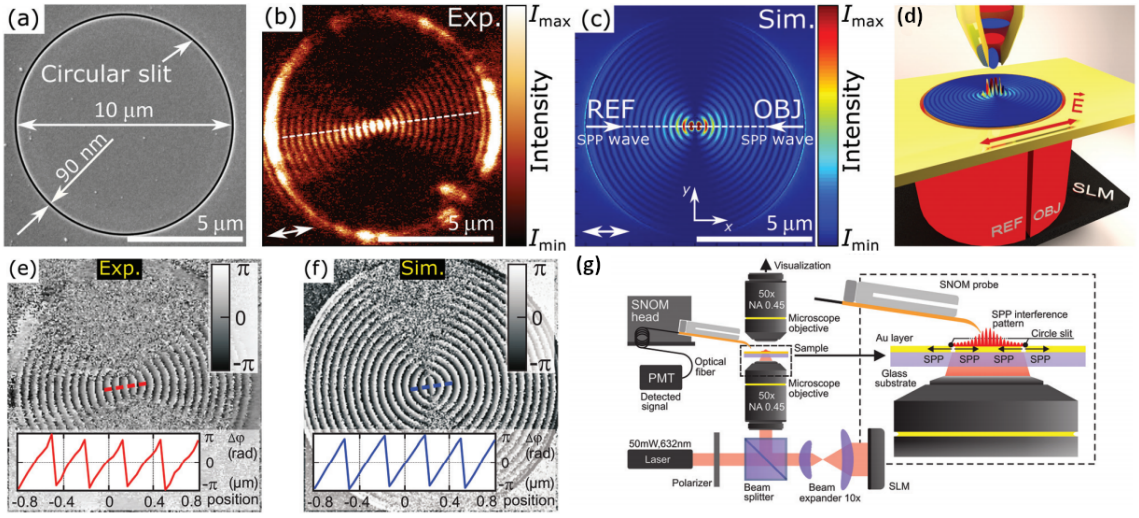

Fig. 2.7: (a) Scanning electron microscopy image of the fabricated 90 nm wide circular slit with a diameter of 10 μm. (b) SNOM image and (c) finite–difference time–domain method simulation of the SPP interference pattern (out-of-plane component) resulting from the laser illumination linearly polarized in the direction marked by the double arrow. (d) Concept of near-field digital holography for plasmon phase imaging. (e) The SPP phase difference reconstructed by numerical processing of the experimental data (interference patterns such as (a)). (f) The simulated SPP phase interference pattern with added noise to emulate experimental conditions. (g) Scheme of the experimental setup. Taken from [72].

A new method being developed by our group is to use spatial light modulator (SLM) in the excitation laser path as shown in Fig. 2.7(d). This enables us to set precise phase–shift to each generated SPP wave and by using the 5–step algorithm we can extract a SPP hologram. A circular sample shown in Fig. 2.7(a) was illuminated from bellow by a laser source. SPP wave resonance formed on the surface as measured in Fig. 2.7(b) matching the simulation in Fig. 2.7(c). The whole SNOM holographic setup is shown in the Fig. 2.7(g) and the results of using this method are shown in Fig. 2.7(e) matching the simulations in Fig. 2.7(f).

3. MACH–ZEHNDER TYPE IN–LINE DIGITAL HOLOGRAPHIC MICROSCOPE

In this chapter, we describe a simple way to construct a Mach–Zehnder type in–line digital holographic microscope shown in Figure 3.2. This instrument allows us to study how objects modulate amplitude and phase of the illumination wave on a pixel by pixel basis. By turning off the reference arm, we are able to also measure near-field intensity images and images of the Fourier plane of the objective by inserting a movable telescope. A custom software was written to communicate with all the parts and a graphical user interface was created to allow users to measure quickly their samples, process the data, and save it for later use. These capabilities are demonstrated in the last section of this chapter.

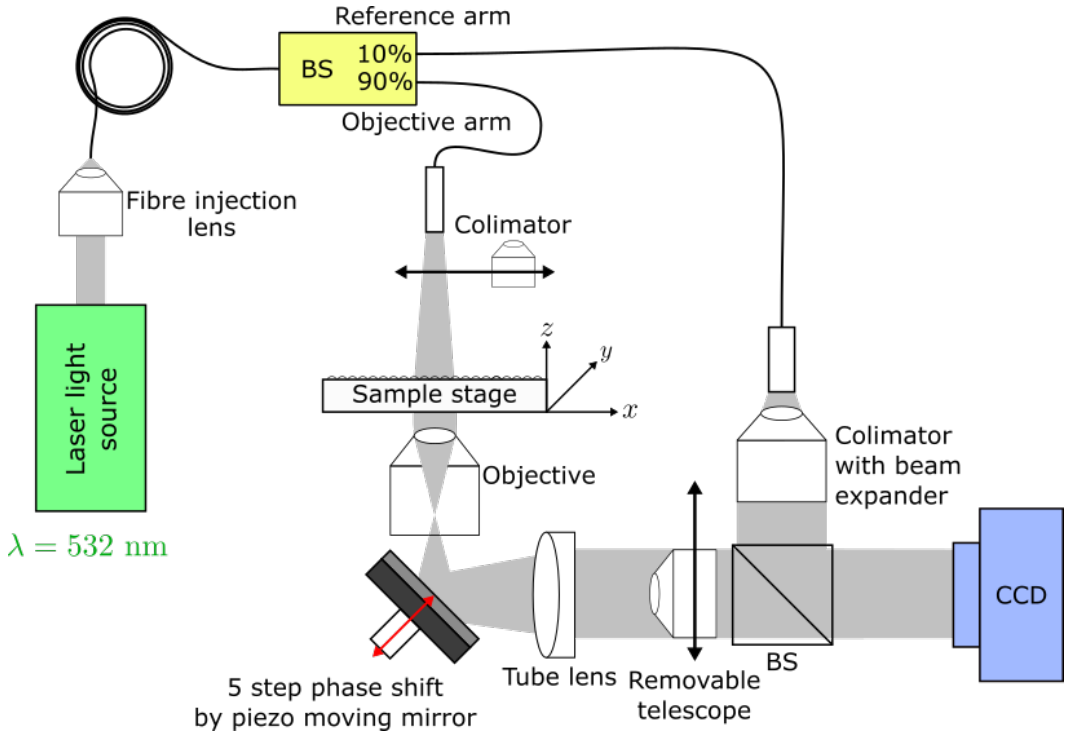

Fig. 3.1: A schematic of a Mach-Zehnder type in–line digital holographic microscope [BS, beam splitter]. Black arrows indicate optional components which can be inserted for additional modes of operation.

3.1 Layout

The schematic of our microscope is in the Figure 3.1. The 532 nm laser source is split between objective and reference arm by a fiber beam splitter. Since most of the light is absorbed and scattered when passing through the sample and optical elements, 90:10 beam splitter is utilized to balance intensities of the objective and the reference arms. Additional intensity correction is done by inserting neutral density filters of varying strength in either optical path.

In the objective arm, we have implemented both Gaussian and colimated illumination beams by a rail system which can switch between simple fiber exit and a colimated exit. Switching between each mode is done by connecting the objective fiber to the desired fiber exit on the microscope and moving the correct exit on the rail above the sample. The Gaussian beam is naturally created by the fiber exit with NA = 0.12.

The laser beam in the objective arm passes through the sample and experiences an unknown phase shift $\Delta\phi$. The sample rests on an XYZ stage with micrometer precision screws which are used to align sample precisely under the illumination source. Light scattered by the sample is then collected by an objective with 20× magnification and NA = 0.40. Next, the laser beam is reflected off of a piezo mirror which is calibrated to introduce a specific phase-shift θ_i compared to the reference arm. A fixed tube lens focuses on a back focal plane of the objective which creates an image of the sample. The image is then combined with reference arm in a beam-splitter. The laser beam in the reference arm is colimated and expanded before interfering with the laser beam from the objective arm. The final interference image is collected by a CCD camera.

To study the Fourier plane of the objective, we have implemented a Bertrand lens which can flipped in and out of the objective arm between tube lens and final beam-splitter. This allows studying the far field with ease. The final built microscope is shown in Fig. 3.2.

Mechanical and electronic equipment used

The laser source used in the setup is Diode Pumped Green CrystaLaser CL-2000 with the wavelength of 532 nm. The fiber beam splitter used was TW470R2F2, 2×2 wideband fiber optic coupler, splitting ratio 90 to 10. The fibers used are P1-405B-FC single mode patch cables for $405 - 532$ nm with FC/PC connectors and 0.12 NA. The objective used was optimized for near UV with 20× magnification. Piezo motor is controlled by the NewportDC servo controller CONEX-CC. Measuring is done by a CCD monochromatic camera CM3-U3-50S5M-CS with 5 megapixels, 35 FPS, from SONY IMX264O.
The control software was written in Matlab R2019a. From there the piezo motor was controlled by sending control messages via COM port and the image of the camera was accessed via a driver provided by the manufacturer.

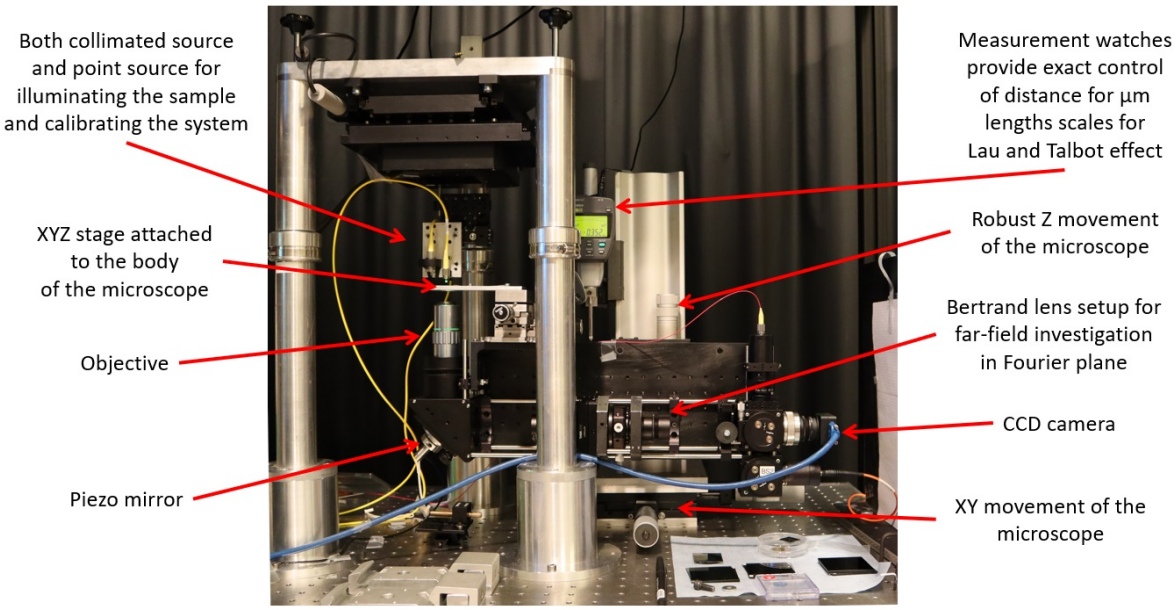

Fig. 3.2: Constructed Mach–Zehnder type in–line phase–shifting digital holographic microscope at the Nanophotonics and Metrology Laboratory, EPFL.

3.2 Custom software

Working with in-line digital holograph can be tricky as it is able to measure change of optical path at the nanometer lengths. Thus, it is particularly sensitive to external disturbances of the apparatus. This is especially problematic when working with thin optical cables which can be deformed by air turbulence. The quality of coherence of the laser source used can be a problem too and can introduce temporal phase shifting errors. For these reasons it is pivotal to carry out all the measurements needed for every hologram in the shortest amount of time.

So, a custom software has been written to capture and process data from the CCD camera. First step of the processing is to extract phase information from the intensity images utilizing the 5-step phase shifting algorithm using modified Goldstein algorithm [73]. The unwrapped phase image can be also fitted with Zernike polynomials to obtain coefficients which represent parameters of the lens [74]. The code is available at GitHub [75].

Programming language

The setup described in this section was meant to be operated by multiple people, so we have decided to use a well known programming language, Matlab 2019a, to build the interface and all the functions. Matlab has the advantage of already having many pre-made functions for creating graphical user interface (GUI), easy syntax, fast image processing, and quick debugging. The main disadvantage of it is its lack of portability as it requires expensive license to install, but fortunately the laboratory had enough licenses for all computers.

Communication

The main software runs on a Windows 10 machine. The camera is connected via USB 3.1 and the communication is done through the *Pointgrey* driver. Matlab already has video input library which mediates this interaction, and allows us to modify any parameter on the camera. The piezo is connected with USB 2.0 and it communicates with our software via a serial port. Several functions have been written in Matlab to allow sending specific instructions to the piezo and read output values from it.

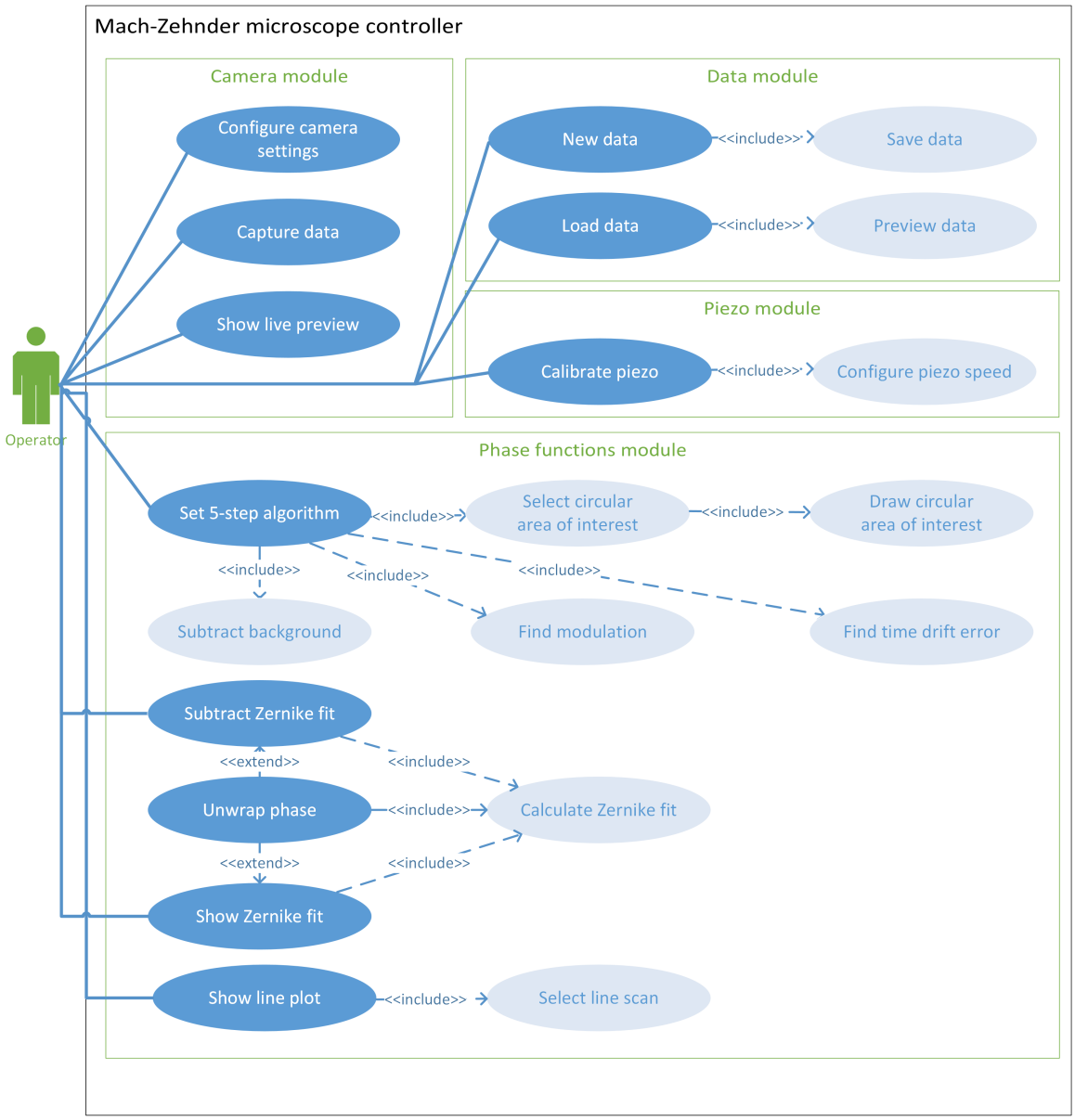

Fig. 3.3: The use case diagram of the Mach-Zehnder in-line microscope. The microscope controller consists of four modules interacting with each other. The operator can choose to use any of them at any time.

Use case diagram

The Fig. 3.3 is shown the use case diagram of our program in universal programming language (UPL). The controlling program for the microscope has three distinct modules the operator can use and will be discussed in the following sections:
1) Camera module.
2) Piezo module.
3) Data module.
4) Phase functions module.

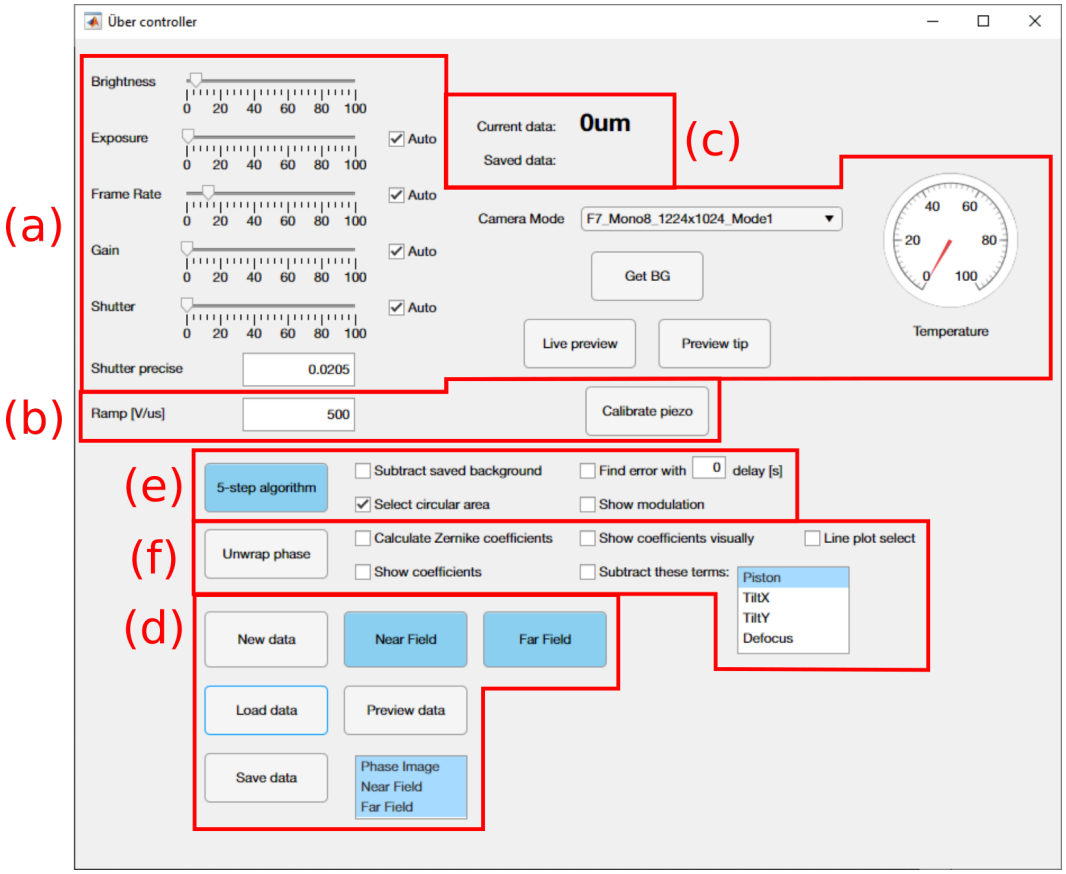

Fig. 3.4: The main graphical user interface (GUI) for controlling the microscope and data manipulation.

3.2.1 Camera module

In Fig 3.4(a) are the controls for the camera settings. The camera is connected with videoinput library in Matlab which uses *Pointgrey* driver to communicate. The camera's individual exposure values by default are automatic, but can be also modified manually to desired value with sliders. Shutter has an input box for more precise configuration. The min/max values are loaded automatically from the camera, and are used to validate the sending values to prevent crashing. A digital thermometer for the main camera was also added as it was continually sending current temperature back. A secondary camera was sometimes used for sample alignment. If it was attached then button *Preview tip*

would show its live preview.

The main camera has several modes of operation based on resolution and output bits. Its default resolution is 2448×2048, but it also supports 1224×1024 and 608×512 by utilizing pixel binning. The return types are monochromatic 8–bit or 16–bit pixel data. For our experiments, the camera was set to 8–bit pixel data as it is computationally more efficient and provides enough pixel information.

Basic flow

1) The operator configures the camera to the desired settings to achieve correct exposure. Each parameter can be set to *Auto* mode and it will try to get balanced exposure automatically.
2) The operator opens live preview to position the view and focus on the sample or to the desired plane of observation.
3) The operator captures image data from the camera using *Near–Field*, *Far–Field*, or *Get BG* buttons. The data from near– and far–field measurements are shown in Fig. 3.6(b).

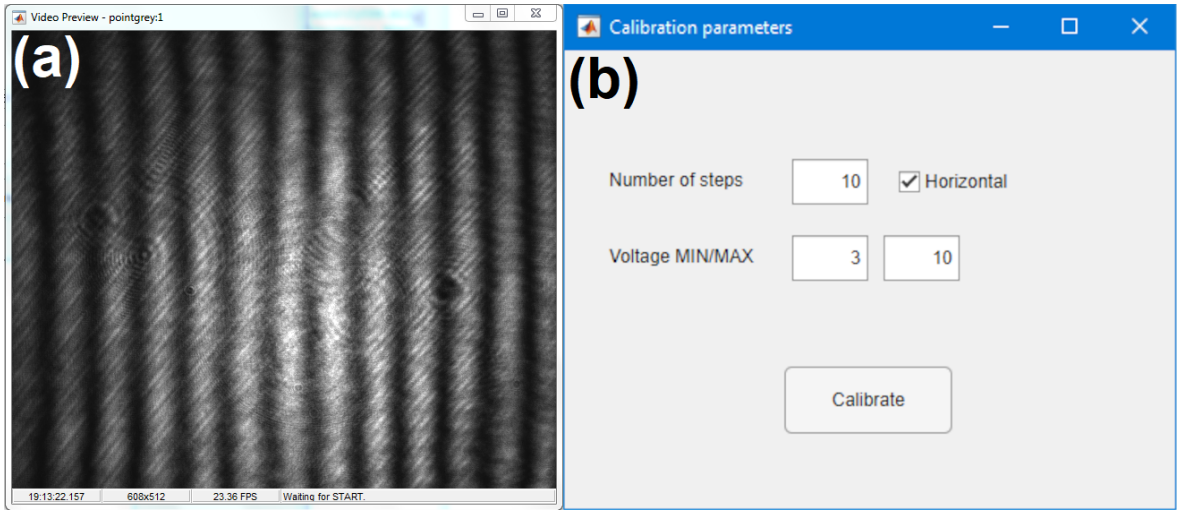

Fig. 3.5: (a) A window showing the correct interference pattern used for calibration of piezo driver. (b) A graphical user interface used for calibrating the piezo voltages.

3.2.2 Piezo module

The piezo servo actuator is driven by a controller which communicates with PC via a serial port by receiving short strings which it parses into commands. Several string parsers have been written in Matlab to mediate this communication on the PC side. Fig. 3.4(b) shows the *Ramp* value text–field which the operator can use to set the speed of the piezo controller, and a button to calibrate the piezo voltage steps for the 5–step algorithm.

Calibrate piezo button runs a function which creates the window show in Fig 3.5(b). *Voltage MIN/MAX* text–field setup the range which the piezo will cycle through while the camera records data. This voltage range is divided into number of steps and at each

a picture is taken. All this is done after pressing the *Calibrate* button. The horizontal checkbox has to be set in the direction the interference fringes are oscillating.

To calibrate the piezo controls, the operator tilts the piezo mirror to form interference line fringes as shown in Fig. 3.5(a). In this case, the *Horizontal* checkbox has to be checked which tells the program to sum the images along the vertical axis. The resulting data is a two dimensional intensity function of horizontal position. Such pattern can be approximated by a sine function which is used to fit the relationship. By extracting the phase of the fitted sine function and unwrapping it, it gives us the relationship between phase and voltage. This linear function the program utilizes to calculate the voltages needed for each phase shifting step. The program then saves the positions to a piezo calibration file corresponding to $0, \pi/2, \pi, 3\pi/2, 2\pi$ phase shift in the objective arm.

Basic flow

1) The operator tilts the piezo mirror to create off–axis pattern as shown in Fig 3.5(a).
1) The operator sets the desired piezo *Ramp* speed.
2) The operator presses the *Calibrate piezo* button.
3) The operator sets the value of the *Horizontal* checkbox depending on the direction of the interference fringes.
4) The operator chooses the minimum and maximum voltage and number of steps the piezo actuator uses for the calibration.
5) The operator presses *Calibrate*.

3.2.3 Data module

Saving the measured data is handled by creating data folders. The data folder's name identifies the data name, and can be created by saving current measurement. In Fig. 3.4(c), the controller displays the current opened data folder and the name of the last saved data folder. Data can be later loaded again at any time overriding the current measured data. The data file consists of near–field and far-field intensity images, extracted phase image from the 5–step algorithm, original images for the 5–step measurement, and the unwrapped phase image. 5–step algorithm and unwrap phase functions can be run with several parameters, so can be re-run with the loaded data instead of capturing new images. The button for data manipulation and preview previously measured data are shown in Fig. 3.4(d).

Basic flow

1) The operator measures his data.
2) The operator saves the data into a file after measuring using *Save data* button.
3) The operator wipes previous data from the working memory by pressing *New data* button.

Alternative flow

1) The operator can load previously saved data using *Load data* button. This will override current measured data.
2) The operator can wipe the current data using *New data* button to start measuring from scratch again.

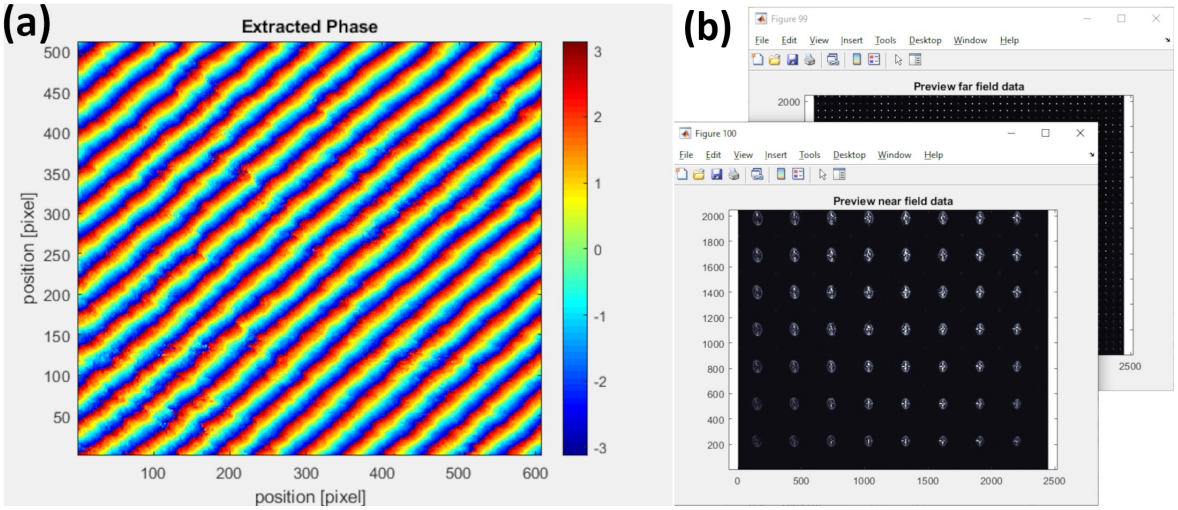

Fig. 3.6: (a) Extracted phase window after running the 5–step algorithm. (b) Windows which are opened when previewing the near–field and far–field captured data by the operator after measurements.

3.2.4 5–step algorithm

5-step algorithm button shown in 3.4(e) runs the 5–step algorithm function. The function has several parameters which can be seen on the right side of the button. The function runs as follows:
1) It retrieves all the positions from piezo calibration file corresponding to $0, \pi/2, \pi, 3\pi/2, 2\pi$ phase shift in the objective arm.
2) Moves the piezo actuator through each position and captures intensity images with the current camera settings.
3) Calculates the phase of each pixel using the 5–step algorithm described in 2.13.
4) Displays the extracted phase image to the user in a window as shown in Fig. 3.6(a), and saves it in the data file.

When the algorithm is finished, user can save the final image and continue by unwrapping the phase. The 5–step algorithm function can also run with several parameters modifying its functionality:
1) *Subtract saved background*: By pressing the *Get BG* button in main menu, the camera saves a picture of the static background and when this parameter is selected, the saved background is subtracted from each image. In theory, this parameter should not make a difference, but can be interesting to compare it to normal operation to be sure everything is working correctly.

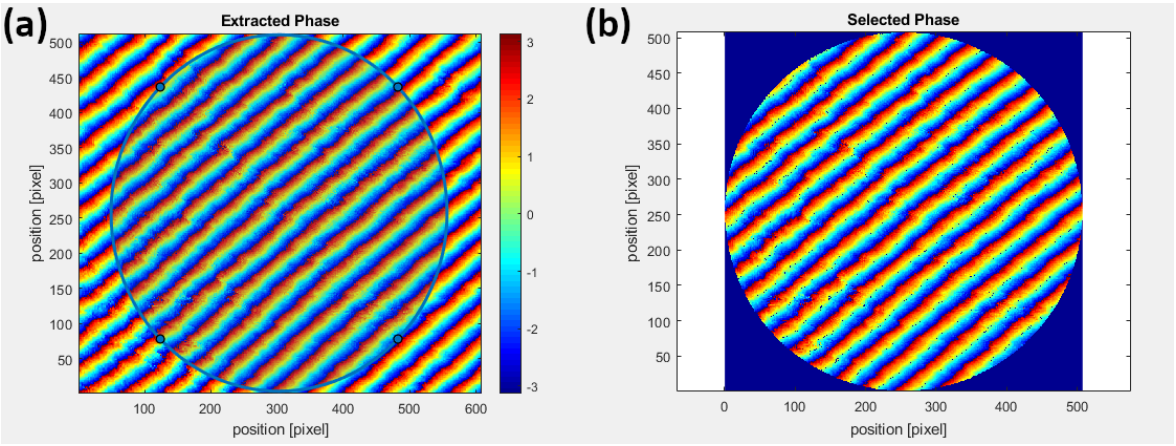

Fig. 3.7: (a) A selection made on the extracted phase image by the operator. (b) A circular cut out from the step (a).

2) *Find error with X delay [s]*: This option runs the 5–step algorithm twice with X seconds delay in between the measurements. Next, it unwraps both phase images and subtracts them. This 3D phase error plot is then shown to the user along with mean square error calculation.
3) *Select circular area*: Unwrapping high resolution images is computationally intensive and some parts of extracted phase image might be unimportant, so the user can use this parameter to select a circular area to be cut out of the extracted phase.
4) *Show modulation*: To find the error of the phase shifting, this option calculates modulation which represents the average phase shift for each pixel. The operator should calibrate the interferometer, so that the phase shift is as close to $\pi/2$ as possible. The formula for average phase shift is in 2.17.

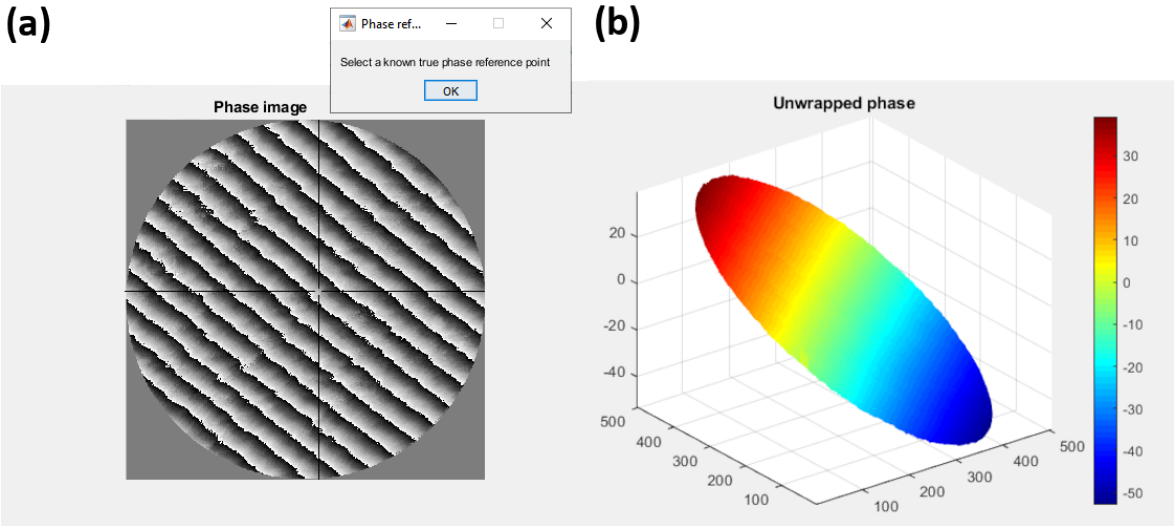

Fig. 3.8: (a) An unwrapping graphical user interface used for selecting the reference phase for the unwrapping algorithm. It sets the selected pixel's phase as 0 rad and the rest of the image is calculated relative to this pixel. (b) The unwrapped phase.

Basic flow

1) The operator find area of interest on his sample using camera module.
2) The operator presses the *5–step algorithm* button to get the extracted phase image of the sample.
3) The operator can then save the image for later study.

Alternative flow

1) The operator can calculate phase–shift errors running the *Show modulation* method.
2) The operator can find the temporal error of vibration or laser instability by using the *Find error X delay [s]* method.
3) The operator can subtract static background for each step of the 5–step algorithm.
4) The operator can select an area of interest after extracting the phase by ticking the *Select circular area* checkbox.

3.2.5 Unwrapping of phase

Unwrapping phase is done with the Goldstein algorithm [76] originally implemented by Bruce Spottiswoode [77]. We will not go into detail how it works, but the general idea is to unwrap the 2D extracted phase image into a 3D hologram by finding abrupt phase jumps and stitching them together by adding a 2π phase shift between them. The unwrapping of a phase image needs a ground truth reference point, so during the unwrap the program will ask the user to provide a reference point on the image which will be set to a base phase value of 0 rad. The rest of the unwrapped image will be calculated in reference to the this point. The window where the operator selects this point is show in 3.9(a). Then, the algorithm unwraps the phase image. Such unwrap is shown in the Fig. 3.9(b).

Since we are studying microlens arrays it is pivotal to study how they distort a wavefront passing through them and find higher frequency aberrations. To describe these aberrations, Zernike polynomials are commonly used to fit the shape of the unwrapped phase. [74] They are a sequence of polynomials orthogonal on a unit disk. Each coefficient of the n–th order polynomial represents certain quality of shaping the wavefront. A wavefront fitted by a Zernike polynomial is shown in Fig. 3.9(a). After fitting the wavefront, the operator can either look at the higher order Zernike coefficients values to evaluate specific higher aberrations directly or subtract the lower order Zernike polynomials from the original data to see all the higher order aberrations visually as shown in Fig. 3.9(b).

The function can be run with several parameters which are shown in the Fig. 3.4:
1) *Calculate Zernike coefficients*: This options enables fitting of the unwrapped phase by Zernike polynomials up to the 14th order. The function then output both plot of the extracted phase and its fit.
2) *Show coefficients*: With this enabled the previous function will also display graphically and numerically all the coefficients for each polynomial.
3) *Show coefficients visually*: Displays all the polynomials plotted separately.

4) *Subtract these terms [Piston, TiltX, TitlY, Defocus]*: This option allows to quickly subtract unimportant parts of the fitted curve to highlight higher order aberrations which are being studied.
5) *Line plot select*: After calculating unwrapped phase, the program will prompt the user to draw a line across the graph to extract a cross–section along the drawn line which then will be shown in a 2D plot window.

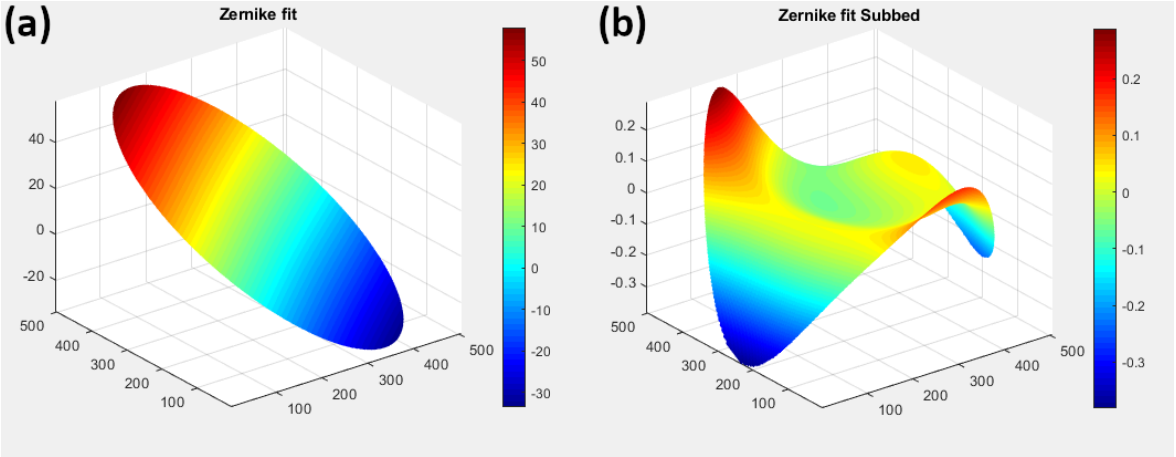

Fig. 3.9: (a) A plot of Zernike polynomial fit for the unwrapped data in Fig. 3.8. (b) Zernike fit from (a) subtracted from the original data to show higher frequency aberrations.

Basic flow

1) After extracting phase image which is suitable, the operator unwraps the phase image by pressing the *Unwrap phase* button.
2) In a new window opened, the operator chooses a point which will be a reference point of phase value 0 rad.
3) The operator can choose to save the final unwrapped image.

Alternative flow

1) The operator can select the *Calculate Zernike coefficients* to display a Zernike fit of the unwrapped phase.
2) The operator can show the coefficient values of each polynomial by also selecting a *Show coefficients* option.
3) The operator can display all the polynomials in separate windows by selecting the *Show coefficients visually*.
4) The operator can choose to show higher frequency aberrations of the wavefront by subtracting any number of the first four fitted Zernike polynomials from the original data.
5) The operator can decide to extract a line plot along a selected line on the unwrapped phase image.

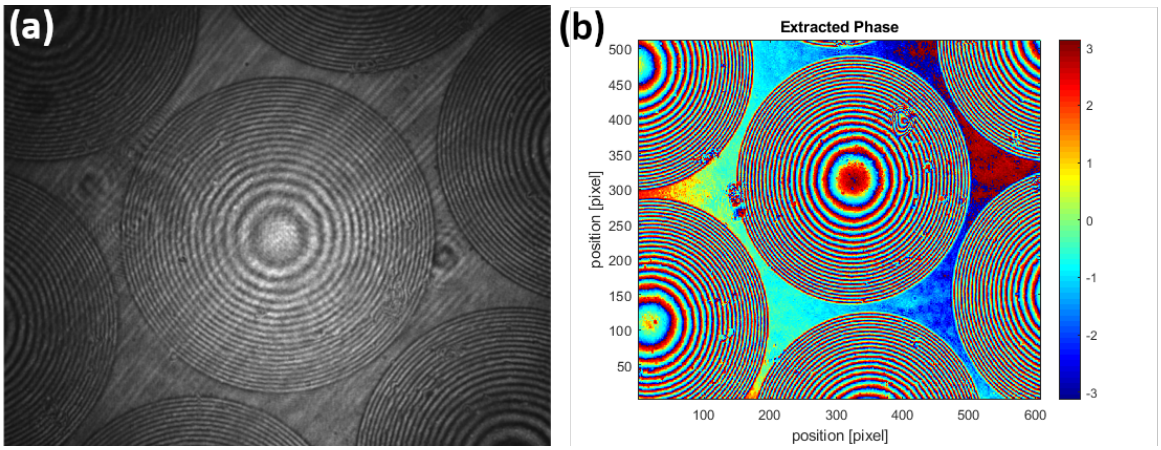

Fig. 3.10: (a) An interferogram of a colimated beam passing through a microlens array. (b) An extracted phase of a microlens array.

3.3 Studying phase shifting structures

This research was funded by Marie–Curie grant for studying micro–lens arrays in the transition regime. The field of optics is well researched for both conventional optics in which light is approximated as rays and for diffraction optics where light is modeled as a wave. However, there are few models which can account for the transitional regime where both diffraction and far–field propagation play a role. Our motivation for building this microscope was to study thick microoptical structures optimized for far–field pattern generation. The results of these experiments helped develop theoretical models of microlens far–field imaging by illumination near the diffraction limit.

During the research, we have also measured several classical microlens arrays to optimize the setup and prove its functionality. We have also been able to measure phase shifting capabilities of nanostructures in a metasurface. Finally, Maryam Yousefi took over the setup to fine tune her simulation models of thick microlens arrays to work on her doctoral thesis.

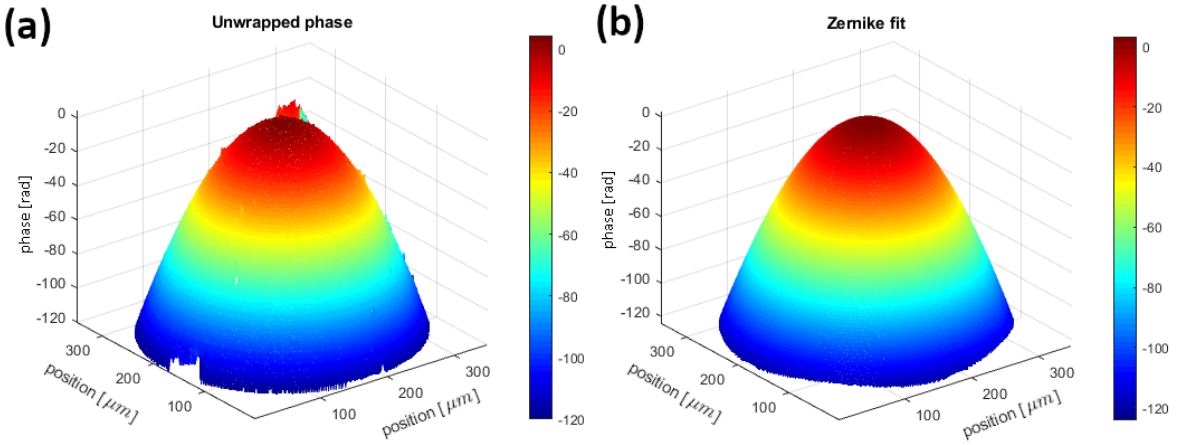

Fig. 3.11: (a) An unwrapped phase profile of a single microlens. (b) A Zernike polynomial fit for a single microlens.

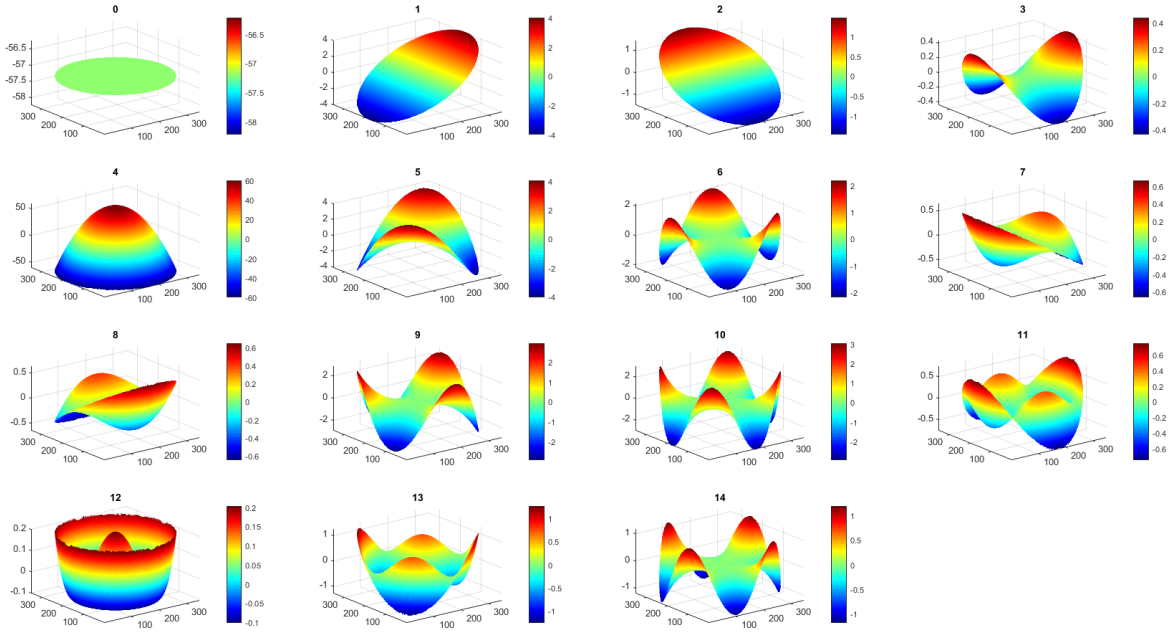

Fig. 3.12: All of the Zernike polynomials plotted separately from the fit in Fig. 3.11(b).

3.3.1 Classical microlens arrays

First, we studied the intensity and phase near-field images of thin microlens arrays. By using our 50× objective, the configuration creates a magnified image of the lens array with resolution reaching 300 nm. For the calibration of our setup we have studied a microlens array from Zeiss which was made of fused silica. The lenses had a diameter of 150 μm and were 15 μm thin. An interference image of the microlens array is shown in the Fig. 3.10(a). By running the 5–step algorithm, we extracted a phase image of the microlens array which is then shown in Fig. 3.10(b). The illumination source was a collimated beam from the backside, so the background has a fairly homogeneous phase. Only one lens was selected from the extracted phase and then unwrapped to produce a hologram shown in Fig. 3.11(a). This measurement shows how the originally flat wavefront was distorted when it passed through a microlens. To study its shape analytically, a Zernike polynomial fit was done to calculate basic parameters of the lens. The fit is shown in Fig. 3.11(b). By studying the Zernike polynomials, we can obtain the curvature of the wavefront, tilt, and its abberations. Each polynomial represents a certain mode and thus gives important information about the lens properties. To represent Zernike polynomials from the last fit visually, the first 15 orders are shown in the Fig. 3.12.

We were also interested in measuring under different illumination configurations to fine tune analytical models. A scheme shown in Fig. 3.13(a) was used to calculate the near–field phase and far–field intensity analytically. The lenses used in this part of the project were from Suss microoptics shown in Fig. 3.13. In Fig. 3.14 are three separate measurements of a microlens array, one with a collimated beam and two with Gaussian beam. The Gaussian beam measurements were done with different distances of D from the illumination tip to the sample. One can notice that the near–field images

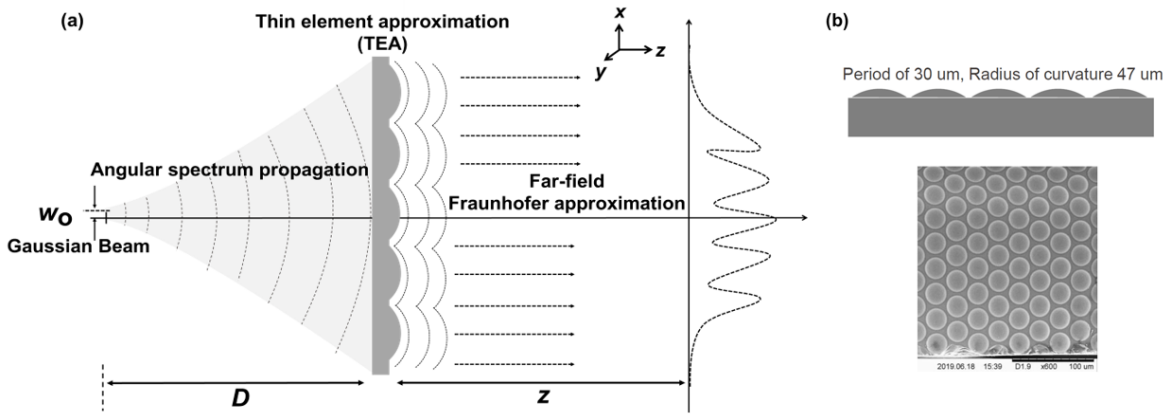

Fig. 3.13: (a) Configuration under study which is an microlens array (MLA) under the Gaussian beam illumination, (b) lens array drawing from side view and a scanning electron microscopy (SEM) images of sample from top view.

look almost identical in all three measurements. The phase image of the microlenses is also very similar in all three. To study the far–field propagation of the lens array, we inserted a Bertrand lens in the optical path behind the tube lens. When configured properly, this setup images the back focal plane of our objective on the CCD chip. This information can be propagated to obtain far–field intensity. As one can notice, the far–field intensity is rather different in all three situations.

These measurements were then compared to the theory developed by Maryam Yousefi. The simulations were done in three steps. First, an angular spectrum propagation from the source to the micro–lens array was performed. Next, the light propagation through the lenses was computed using the thin element approximation. Finally, the calculated phase after the lens arrays was propagated into the far–field using Fraunhofer approximation [78]. The results of the simulation for the Gaussian beam are shown in Fig. 3.15. This proved the simulation models for thin lenses are correct and allows us to design specific far–field patterns using back propagation. However, the far–field patterns were extremely weak. The highest exposure settings barely captured the dot patterns shown in previous images. Here, thick microoptical elements will useful as shown in the next section.

3.3.2 Sinusoidal phase grating

Generating high–contrast dot pattern with a high field of view and equal intensity peaks has many uses in imaging, microscopy, or sensing. This task is very challenging and one method of achieving it is through the use of microoptical elements under Gaussian beam illumination. As a good model system, a thick sinusoidal grating with a 50 μm with different heights illuminated by a Gaussian beam was investigated. The near–field phase was measured using our system and the measurement is shown in Fig. 3.16. The near–field obtained experimentally was used to validate simulations of the microoptical system [79]. While a sinusoidal grating is a good model, it only illuminates in one dimension. So, for a 2D dot pattern we need to use a thick micro–lens arrays.

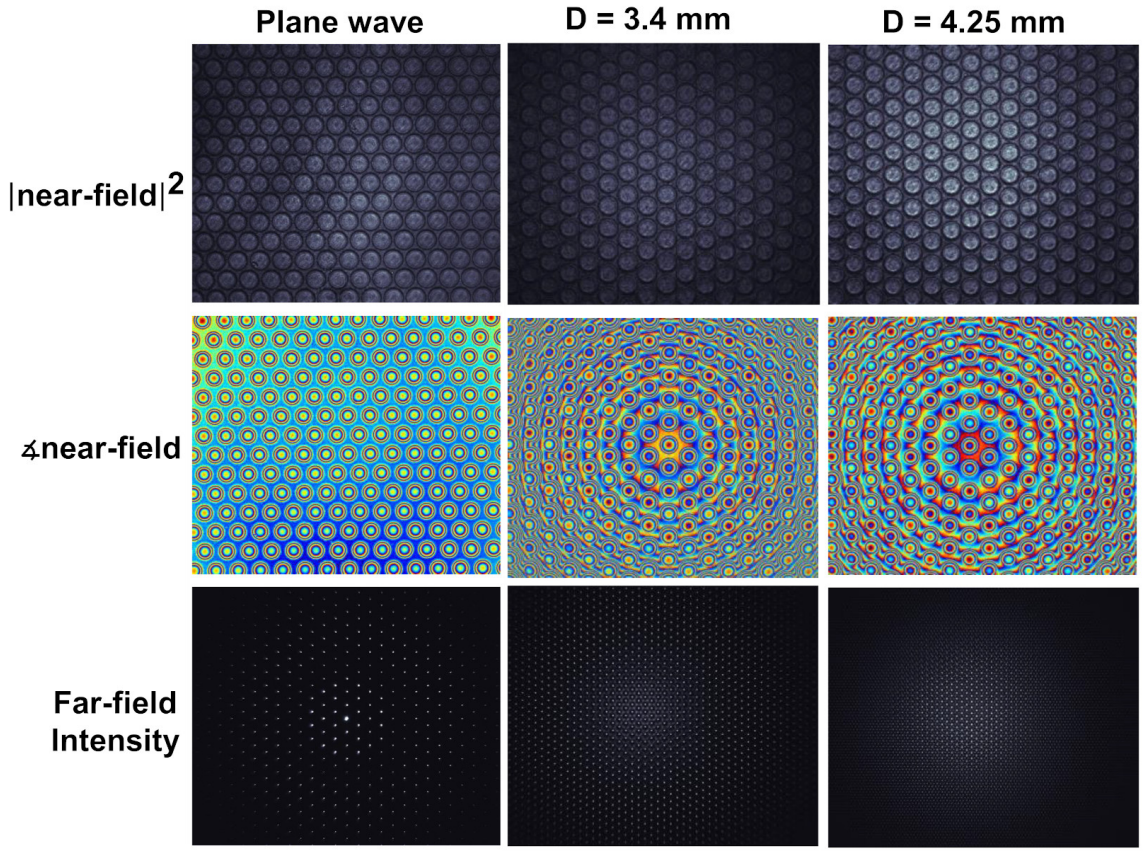

Fig. 3.14: Three measurements of near–field intensity of microlens array with illumination by a plane wave and Gaussian beam with distance to the sample of $D = 3.4\,\mathrm{mm}$ and $D = 4.25\,\mathrm{mm}$. The corresponding near–field phase profile is shown along with a far–field intensity.

3.3.3 Thick microlens arrays

Thick microlenses are very hard to model properly. When light propagates through them it refracts, reflects, and diffracts inside them and in the surrounding area. This makes designing them a challenging engineering problem. So far, only limited models have been developed to design thick microlens arrays for specific far–field dot generation. In Fig. 3.17 is a complete measurement of a thick microlens array using our setup. It is interesting that the microlens system does not modify the near–field phase very much, but is able to create sharp far–field patterns. Many more measurements have been made on these systems, so now we are waiting for a fast simulation model to be developed based on these results. This concludes the microlens measurements made on the system so far. However, the phase measuring capabilities of our setup were also utilized for studying phase shifting capabilities of metasurfaces.

3.3.4 Metasurfaces

Metasurfaces are structured 2D systems generally built out of plasmonic nanostructures. Our group was developing metalenses and needed to test if their nanostructures produced correct phase shifts. First $10 \times 10\,\mu\mathrm{m}^2$ arrays of nano–holes were milled into a gold

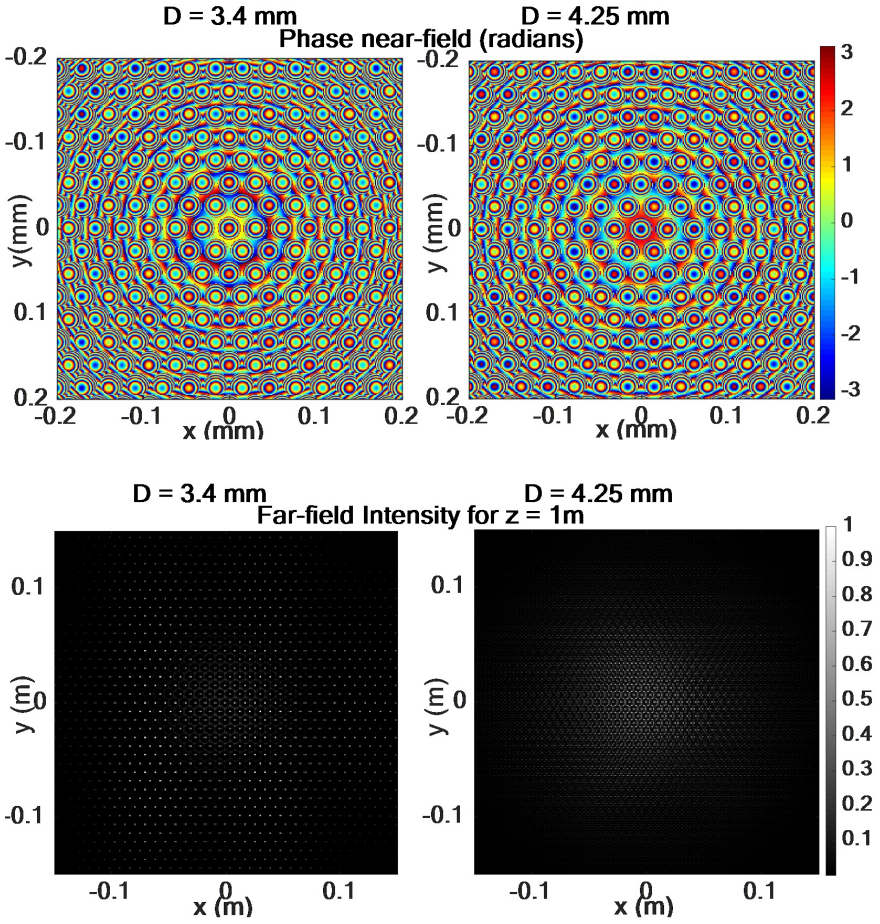

Fig. 3.15: A simulation results of microlens array using Gaussian beam illumination with distance to the sample of $D = 3.4\,\text{mm}$ and $D = 4.25\,\text{mm}$. The corresponding near–field phase profile is shown along with a far–field intensity.

film using focused ion beam. These structures were then analyzed by our holographic microscope. The results are shown in the Fig. 3.18. The top arrays have induced phase–shift $\phi_1 = 2.47\,\text{rad}$ and the bottom ones $\phi_2 = 0.94\,\text{rad}$ to the passing wavefront. The phase shift was subtracted from their average surrounding phase as the wavefront was not perfectly flat throughout the measuring window. By subtracting the phase shifts of the structures, we get a relative phase shift to each other $\phi = \phi_1 - \phi_2 = 1.53\,\text{rad} = 88°$. Unfortunately, to fabricate a metasurface lens a phase shift of $\phi = 3.14\,\text{rad} = 180°$ is needed for the two metasurfaces. The reason why the nanostructures were not able provide correct phase shift was probably due to manufacturing errors as well as some simulation errors which did not account for the precise shape of the milled holes.

This concludes the capabilities explored so far of our Mach–Zehnder type in–line digital holographic microscope. Hopefully, in the future, more applications and modifications will be made to improve its capabilities. The main disadvantage was the inability to overcome the Abbe's limit for imaging as the collecting lenses were diffraction limited. If we replaced the objective with a SNOM head to collect the near–field information, we would get enough information to resolve much finer details at nanometer scales. Such a device will be introduced in the next section.

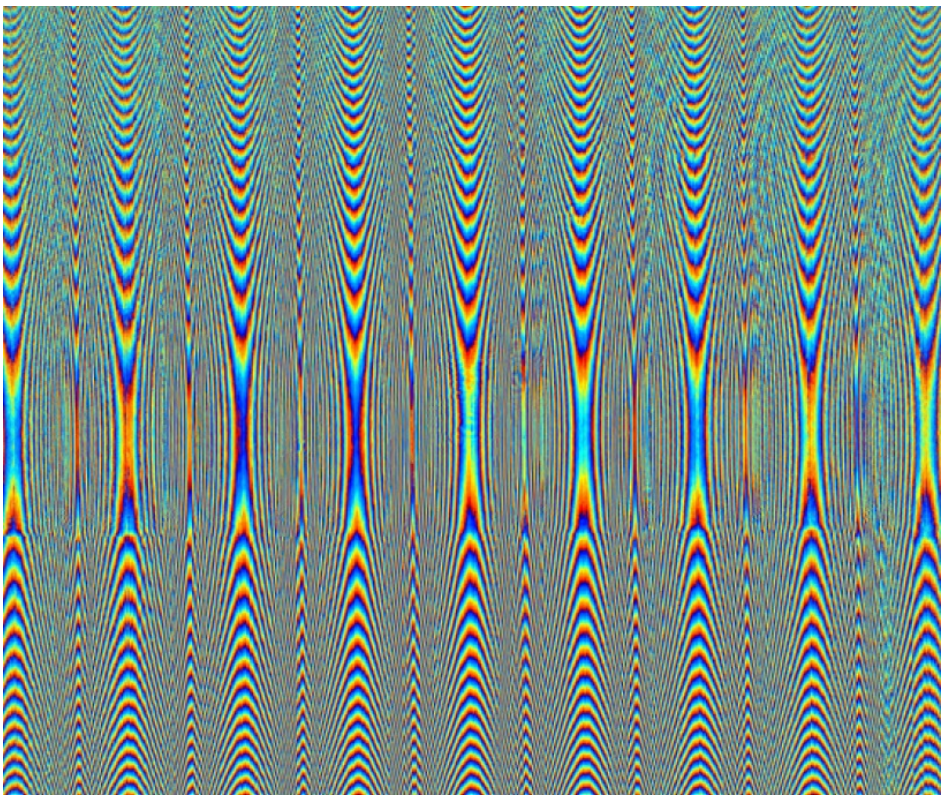

Fig. 3.16: Near field phase profile measurement for 12 μm sinusoidal phase grating. Taken from [79].

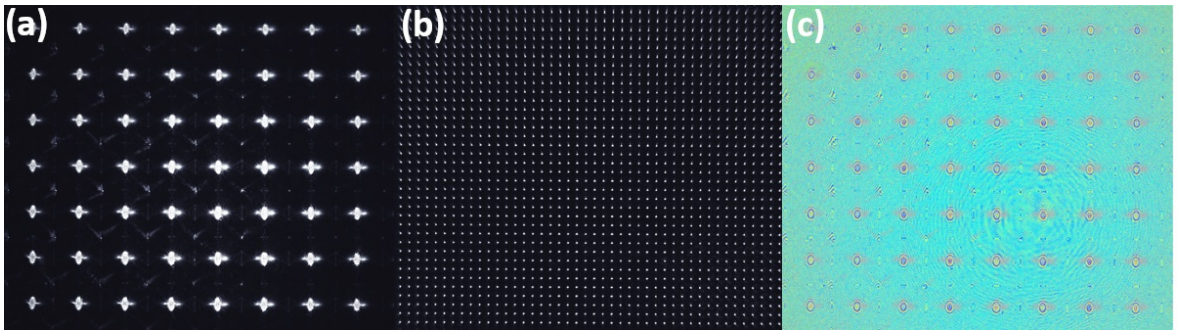

Fig. 3.17: (a) Near–field amplitude, (b) far–field amplitude, and (c) near–field phase profile measurement for thick microlens array.

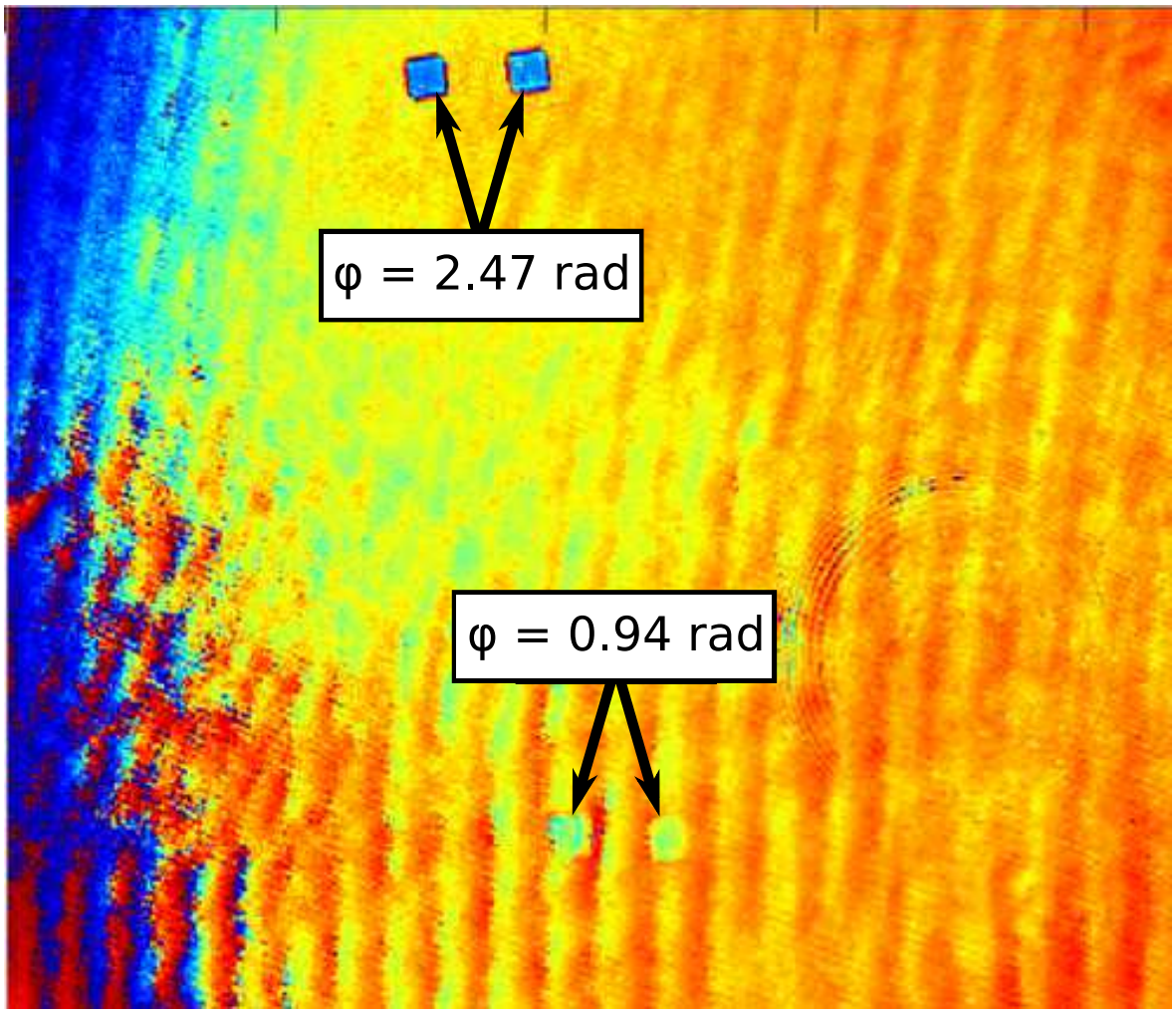

Fig. 3.18: Phase shifting induced by a metasurface arrays. Two different nanostructures have been used (top) and (bottom) for generating a phase shift. The measurement was completed using our holographic microscope.

4. SCANNING NEAR–FIELD HOLOGRAPHIC MICROSCOPE

This chapter focuses on how we have built a scanning near–field holographic microscope in our laboratory, and how we designed a software for remote control of our setup and data processing. Using this setup, we have been able to achieve phase imaging bellow the diffraction limit. During the project, several samples have been fabricated and measured which is shown demonstrated in the last part of this chapter.

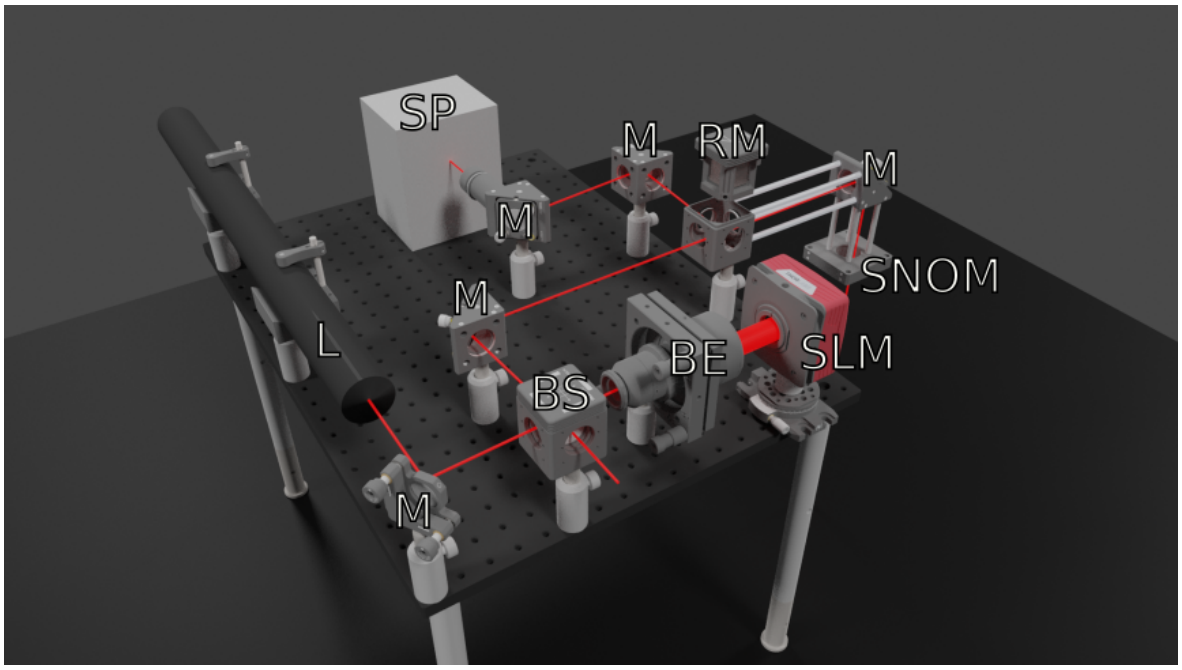

Fig. 4.1: The model of our laser injection system for a scanning near–field optical holographic microscope. L - laser source; M - mirror; BS - beam–splitter; BE - beam expander; SLM - spatial light modulator; RM - removable mirror; SNOM - an injection port for the SNOM.

4.1 Experimental layout

First, a 3D model of the setup was created in Blender using parts from Thorlabs. Fig. 4.1 shows our design for injecting laser into the microscope. We added a possibility of a reverse configuration where the capturing light from the microscope is sent to

a spectrometer by adding a removable mirror. This creates a direct path from the microscope to the spectrometer.

Fig. 4.2 shows our experimental setup for measuring surface plasmon holography. Helium–neon gas laser with wavelength of 632.8 nm is directed by a mirror with xy tilting through a beam splitter into 10× beam expander. The expanded laser beam is reflected off of a spatial light modulator (SLM) which changes the spatial distribution of phase in the cross section of the beam as shown in Fig. 4.3(c). In this case, the π phase shift of neighboring regions creates destructive interference rendering the interface between them dark. The reflected beam travels back through the beam expander and is redirected by the beam splitter and two mirrors into the top port of Olympus IX71 microscope. The microscope focuses the laser beam on the sample surface with a 20× objective. The incoming light scatters off of ridges on the sample. These ridges act as dipoles exciting surface plasmon polaritons (SSPs) traveling across the sample surface as explained in the section 1.4.1. By sending two waves of SPPs against each other, they interfere and create standing wave on the surface. When a SNOM tip comes near the surface of the sample, evanescent fields of the SPPs can couple with the aperture which is acting as a dipole. This transfers the energy from a SPP wave to the aperture dipole which excites photons into the fiber tip. The signal travels through the fiber inside the SNOM aparatus, and is amplified by a photomultiplier. The amplified signal is then collected via a photo sensitive chip. The data is paired with xy positional information to create a 3D map with 2 axis representing position and 1 axis representing intensity of collected light. The distance between the tip and sample's surface is controlled by a feedback–loop mechanism (FLM). We also obtain the topography of sample by measuring FLM's voltage, similar to an atomic force microscopy.

We attached two cameras to enable observation of sample during alignment. First is inserted into one of the oculars of the microscope, giving us the ability to observe the sample and the laser spot from the laser side. Second camera is attached above the sample with a strong light source, so we can observe the laser spot on the structure of the sample and align it however we need.

4.1.1 Spatial light modulator

A spatial light modulator (SLM) is a device which imposes spatially varying modulation on a beam of light. In our setup, we have used an SLM device which imposes a specific phase delay in the cross section of our laser beam. We are using electrically addressed spatial light modulator which consists of pixels made of liquid crystals whose orientation is controlled via electric field and a reflecting back plate. The orientation of each crystal determines the pixel's refractive index. This allows us to impose specific phase shift on a pixel basis. The SLM used in our setup had 800×600 pixels with 196 levels of phase delay between $0 - 2\pi$. The principle of operation is shown in Fig. 4.3.

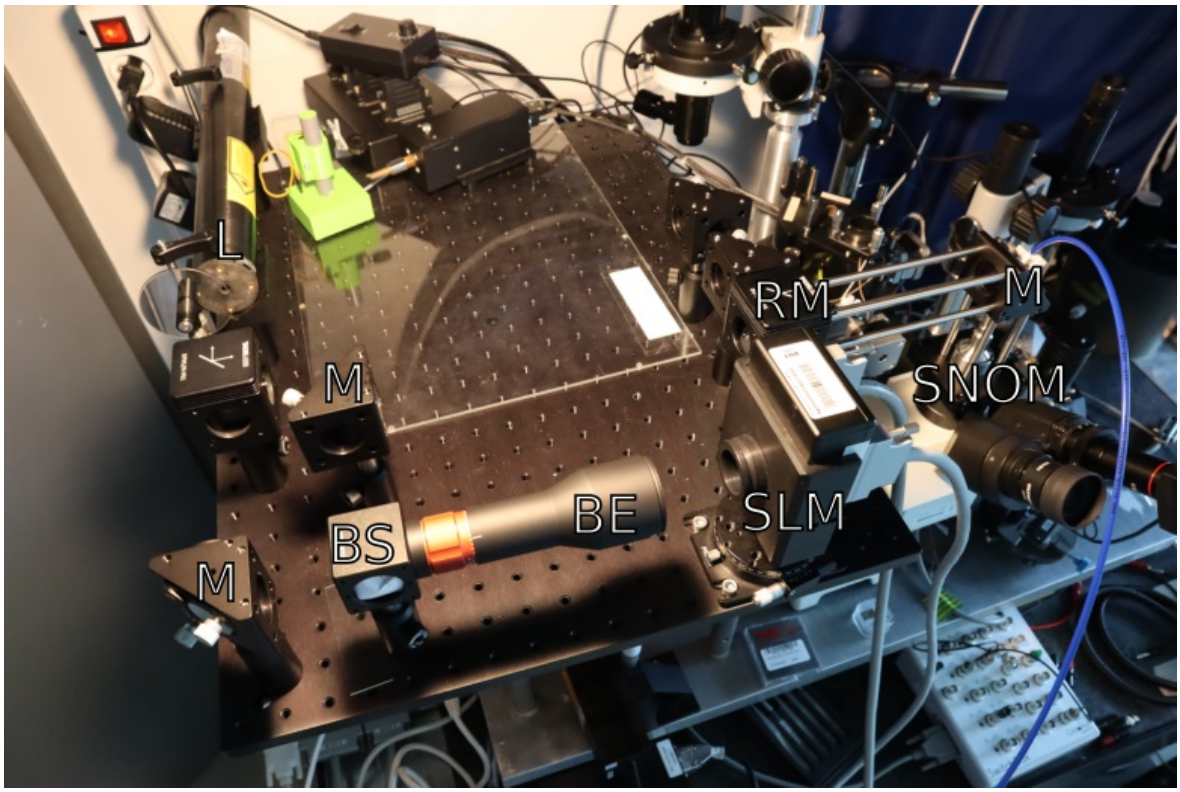

Fig. 4.2: The laser injection setup for SNOM holography. L - laser source; M - mirror; BS - beam–splitter; BE - beam expander; SLM - spatial light modulator; RM - removable mirror; SP - spectrometer; SNOM - an injection port for the SNOM.

4.1.2 SNOM measuring loop

The operation of SNOM holograph is very time expensive task. Time between the insertion of a sample into the microscope and capturing a single hologram can take several hours. Most of this time, the operator is simply waiting or manually re–processing images. This motivated us to design a custom software to enable remote control of the microscope setup and fast processing of the measured data.

Say the operator wants to collect a SNOM hologram. First, he aligns the laser insertion setup and adds a sample onto the SNOM stage. Then, he aligns the laser onto the sample surface. Next, he places the SNOM head on top of the sample and calibrates the piezo then begins to approach the sample. This process is automatic and can take around a one hour, so he has to wait. Since he has to stay in the laboratory, this can be very unproductive time for him as he does not have his work PC there, and is distracted by other operators and lab noises.

When the SNOM tip finally approaches the sample, the operator can begin measuring. First, he uploads a phase mask to the SLM. He cannot readily modify the mask to give it certain rotation, so he has to be precise with his stage alignment. Once all the alignments of mask and focusing of the laser beam are done, he can begin measuring topography and the SPP signal (transmission). This again takes around an hour and is automatic, so the operator has to wait until it finishes. If the measurement is successful, he repeats the last step 4 times while changing the SLM mask each time.

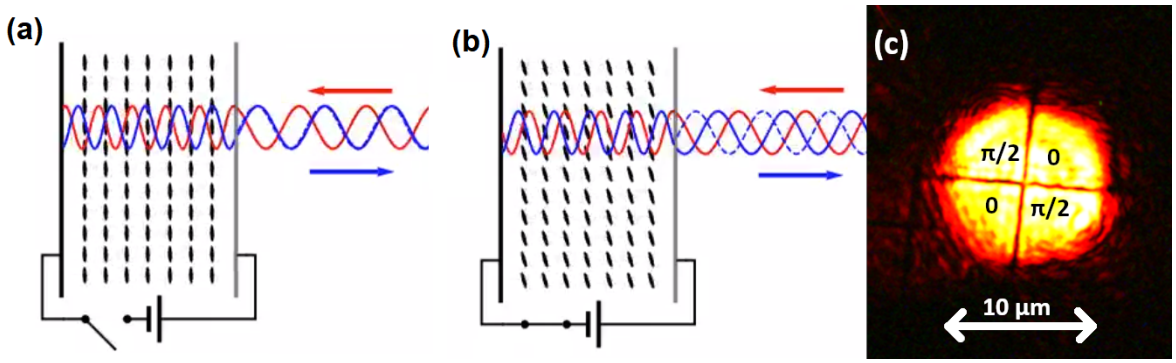

Fig. 4.3: The principle of operation of a spatial light modulator. When voltage is applied to the liquid crystals they rotate and induce a phase shift to the outgoing light as shown in (b) by moving the blue wave to the right. (c) The laser beam split into 4 regions. At the interface of each region destructive interference happens.

When the operator finishes all the measurements, he is left with 5 topography and 5 transmission images. Unfortunately, the SNOM can drift between measurements, so the next step is to align the images based off of topography. Doing this by hand is rather imprecise, and can lead to image shift errors which produce results not physical in nature, artifacts of image manipulation. Lastly, the operator inserts the images into his software which finally outputs the desired hologram.

4.2 Custom software

A part of the contribution of this master's thesis is to create three software tools to automate the SNOM setup and allow remote control. The use case chart for the utilities is shown in 4.4. Each serves a specific role and can be run separately.
1) Phase mask generator and SLM controller.
2) Stage controller.
3) Image aligning and phase extraction tool.

Programming language

All modules have been written in Python 3.6. The language was chosen because of its versatility, plethora of external libraries, and easy deployment. The code for Arduino Uno was written in its own language based on C++ using the Arduino IDE. The code is available at GitHub [80].

Communication

The communication between Arduino and PC was done via serial port. A string of instructions was composed on the PC side and transmitted to Arduino as a series of bytes with a beginning, separator, and terminator bytes. The Arduino then decodes the string into a single instruction with several parameters which it carries out. The Arduino itself communicates with motors, light, and shutter by changing voltage of its communication pins.

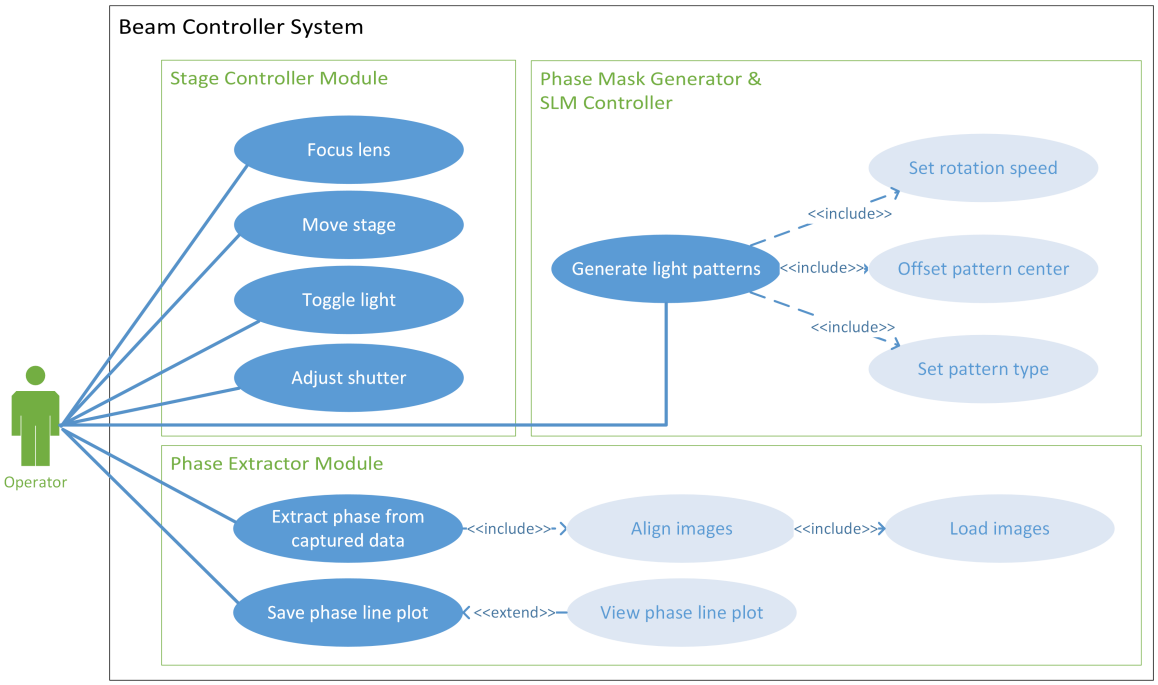

Fig. 4.4: The use case chart for software written in this thesis for the scanning near–field holographic microscope made in universal modeling language.

4.2.1 Phase mask generator and SLM controller module

This module enables operator to generate custom phase masks and upload them to the SLM device directly. There are two mask patterns to choose from, a vortex and a square. Both can be modified by changing their parameters. The pixel color represents the phase delay, but it is different for each wavelength, so correct wavelength has to be set in the *Wavelength* input field. The phase mask can also be modified by shifting its center point on the screen. This can be achieved by specifying the center's coordinates or using mouse to select a point on the mask. The mask can be also rotated by a specific angle or angular speed around its center. If several displays are attached the window drop down menu can be used to select the SLM as output.

Basic flow

1) The operator sets the wavelength of the laser beam used.
2) The operator selects square or vortex type of mask and sets its parameters. Then, the operator presses the *Generate* button to create the phase mask.
3) The operator selects the monitor output corresponding to the SLM device and toggles the *output enabled* checkbox to output the mask to the SLM.
4) The operator rotates the mask by a desired angle and sets the center of the mask to the desired position to get the correct illumination of the sample.

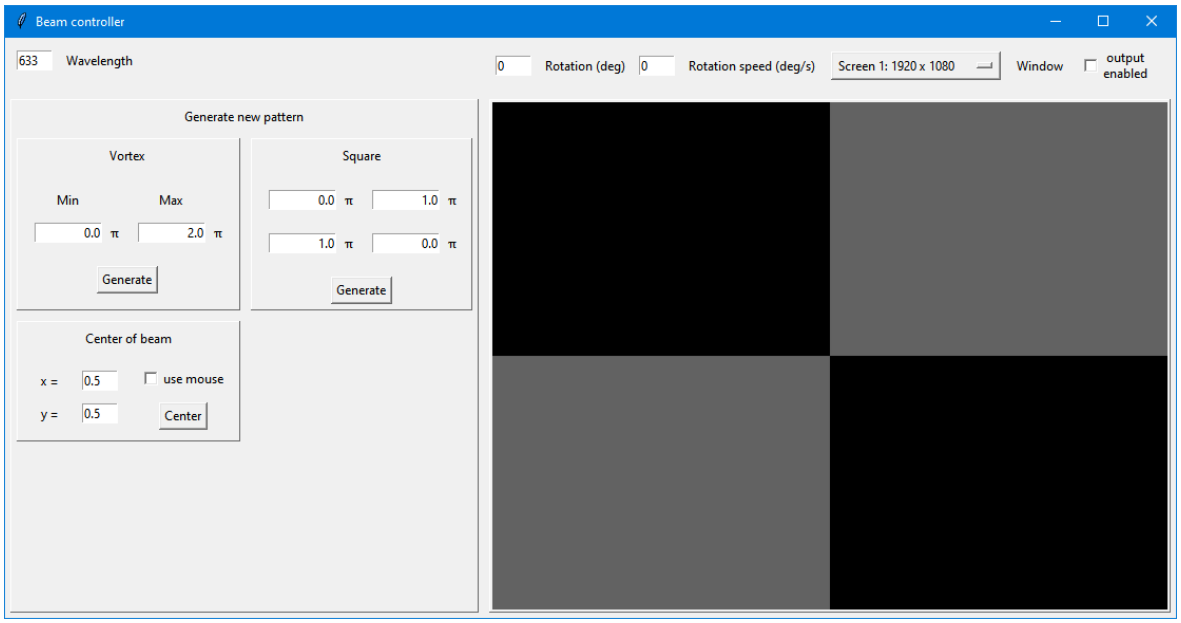

Fig. 4.5: The phase mask generator and SLM controller graphical user interface (GUI). An operator can use this module to upload custom phase masks to the spatial light modulator. The masks can be also changed real time for precise control over the beam shape.

4.2.2 Phase extractor module

The main function of this module is to extract the phase of the SPP waves from the images previously captured by SNOM. The images outputted from the SNOM can be loaded into the program by clicking the load image next to each picture slot. The images can be either in .PNG format or as raw data in .TXT format. To load a whole folder, the operator can press the *Load Folder* button and select a folder from the filesystem where the images are located. The software then uses the naming system specified under the button to select the correct images using the symbol ? as a placeholder for the numbering of images.

To properly extract the phase, the operator has align the images on top of each other. If the topography data is loaded with the SNOM data, this can by invoking the align function. The align function works by cross–correlating the first topography image with every other topography image to find the lateral shifts between images. The cross–correlation was implemented by using a convolution the two images using fast Fourier transform with the second image being rotated by 180°. The peak frequency of the convoluted image transformed into the image coordinates gives the center of the second image in the first image's coordinates. By subtracting the first image's center coordinates from the second's we get the lateral shift of the two images. This is done for each subsequent topography image. Finally, both the topography and SNOM images are shifted by the opposite of their lateral shift to be superimposed on top of each other, a largest possible window of the overlap is calculated, and the images are cropped according to it. To check if the images are aligned properly, the *Open aligned images* button can be pressed or any image icon can be clicked to open the image

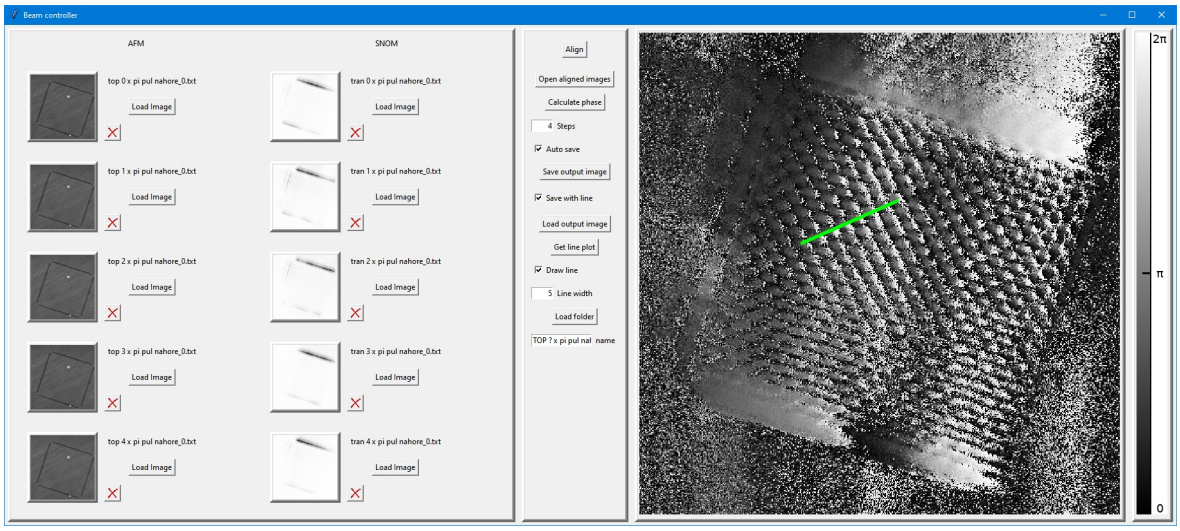

Fig. 4.6: The phase extractor graphical user interface (GUI). The program has already processed SNOM data and the extracted phase is shown on the right. The green line indicates the path along which the line plot is calculated.

viewer and cycle through the images as shown in Fig. 4.7(a).

The properly aligned SNOM images can be used to extracting the phase of the SPP waves. By pressing the *Calculate phase* button a 4– or 5–step algorithm is run based on the number of steps specified under the button. The 5–step algorithm runs the calculation from eq. 2.13 on each pixel. The 4–step algorithm runs the same as the 5–step algorithm with $I_5 = I_1$. If *Auto save* is toggled, the extracted phase image is automatically saved into the input folder. This can be also accomplished manually by pressing the *Save output image* which opens dialog box to select a place to save the output image.

The profile of the extracted phase image can be investigated by toggling the *Draw line* checkbox then drawing a line on the image using mouse. Next, the *Get line plot* button is pressed and a line plot across the drawn line is plotted as shown in Fig. 4.7(b). The line plot can be saved as an image or .TXT data. The data is averaged over the width of the line drawn which can be set using the *Line width* input box. The line position can be saved on the extracted phase image by toggling *Save with line* checkbox before the image is saved.

Basic flow

1a) The operator loads 5 topography and 5 SNOM images by clicking the Load Image button next to each of the empty thumbnails and by specifying a valid path in the filesystem.
1b) The operator loads 5 topography and 5 SNOM images by selecting a template name of the images and then specifying containing folder in the filesystem.
2) The operator aligns the images by clicking the *Align* button.
3) The operator views the aligned images by clicking the *View Aligned Images* button or by clicking the thumbnails of images.

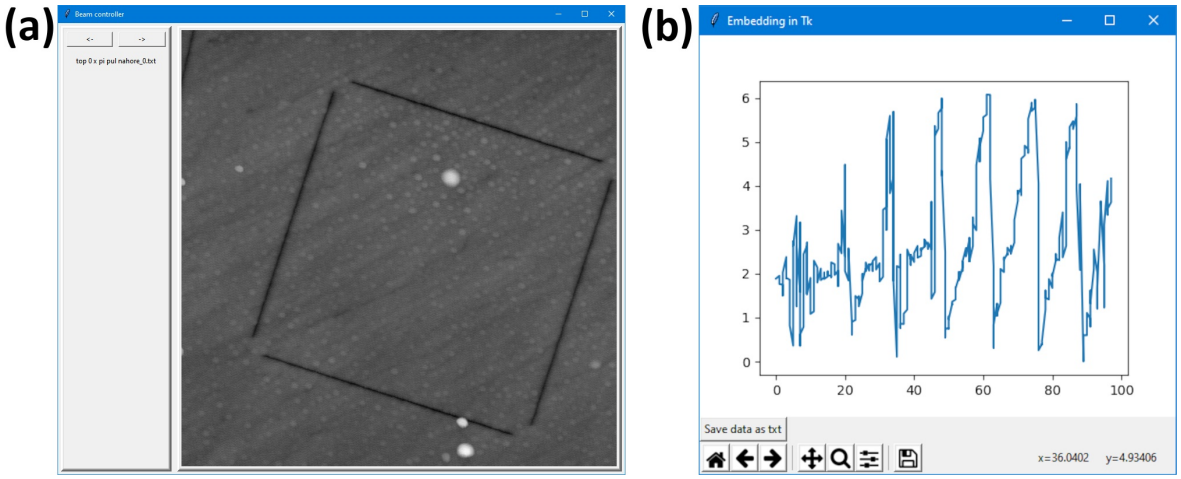

Fig. 4.7: This figure shows two additional windows opened by the operator in the phase extractor module: (a) an image viewer GUI, (b) GUI showing line plot along the green line in Fig. 4.6.

4) The operator extracts the SPP phase by clicking the *Calculate Phase* button.
5) The operator draws a line across the output phase image in the program.
6) By clicking the *Get Line Plot* button, the operator is able to view a cross–section of the extracted phase across the drawn line plotted on a 2–axis diagram in a separate window. This window remains open until closed by the *X* button in the upper right corner.
7) The operator saves the diagram image by clicking the floppy disk button or saves the data as .txt file by clicking *Save data as txt* button.

Alternative flow

1) The operator may load different images at any time.
2) The operator may choose to load previously extracted phase image, so he can extract a new line cross–section.
3) The operator can choose the integration width of the line plot.

4.2.3 Stage controller module

Using this module, the operator is able to control xy direction of the SNOM stage, focus z of the Olympus microscope, toggle light above the sample, and toggle laser shutter from the software. The operator can precisely set the desired speed/stepping distance for each axis of the xy stage and the microscope focus z by moving the slider under the axis' buttons.

Basic flow

1) The operator toggles light by clicking the *Toggle light* button. The checkbox underneath tells him the current state of the light.

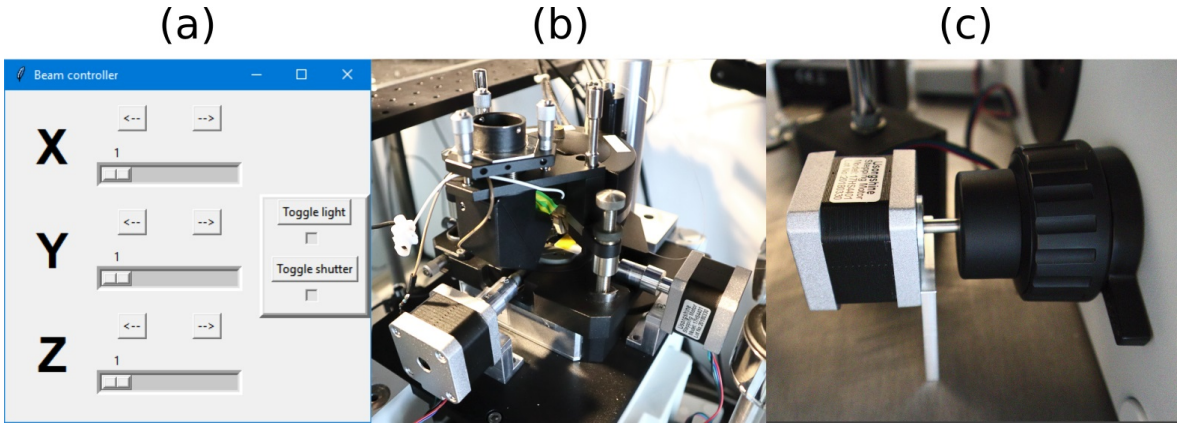

Fig. 4.8: (a) The stage controller GUI. (b) The SNOM stage. Two stepper motors control the x and y axis. (c) The focusing knob of the microscope. A stepper motor was added to focus remotely.

2) The operator toggles laser shutter by clicking the *Toggle shutter* button. The checkbox underneath tells him the current position of the shutter.
3) The operator sets a speed on a slider next to the axis he wishes to move.
4a) By clicking the directional button, the operator moves the axis in the desired direction by the amount of steps selected in step 3.
4b) By holding down the directional button, the operator moves the axis in the desired direction with the speed selected in step 3.

4.3 Measurements of plasmon holography

The scanning near-field optical holographic microscope described in this chapter was built as a part of a project submitted to the Czech Science Foundation (Grantová agentura České republiky - GAČR). The plan for the project is to develop plasmon digital holography for quantitative phase imaging below diffraction limit to enable studying of 2D nanostructures on metal–dielectric interface. To demonstrate the capabilities of our setup, several samples have been fabricated to serve as on–chip interferometers. One of these samples has been measured as we will shown later.

4.3.1 Fabrication of on–chip interferometers

The fabrication of samples was done in three steps:
1) Fused silica wafer was cut into small samples.
2) Gold crystals were grown and deposited on the samples.
3) Focused ion beam milling was employed to mill the structure of samples.

The samples used for the following measurements were fabricated in the laboratories of the Institute of Physical Engineering at Brno University of Technology and in the cleanrooms of CEITEC Nano.

Sample cutting

A pure fused silica wafer was coated by a spincoater with protecting layer of photoresist and then cut using Laser dicer Oxford Lasers A-Series into $10 \times 10\,\mathrm{mm}^2$ samples. These were then cleaned in an ultrasonic bath, first using acetone, then isopropyl alcohol, and finally water. After drying, the samples were ready for the next step.

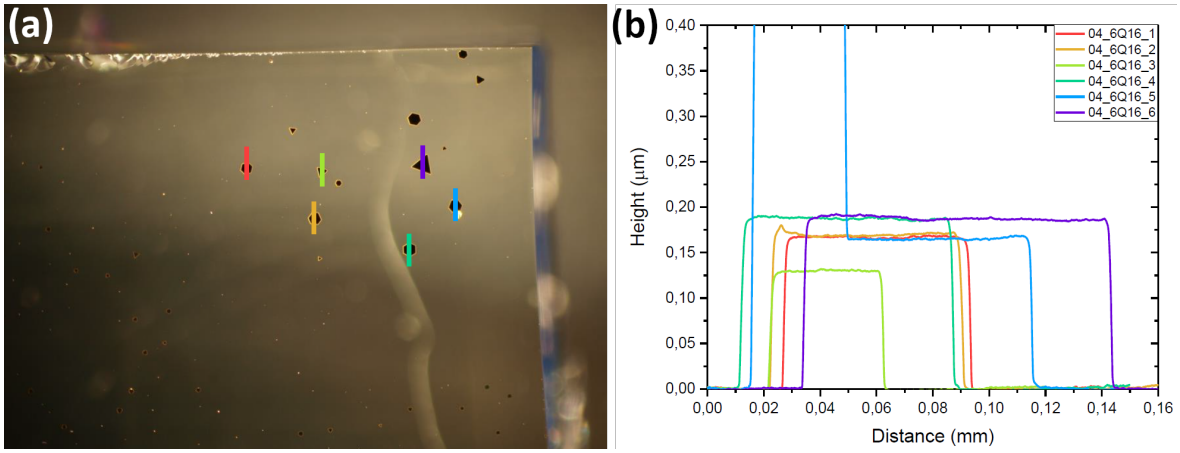

Fig. 4.9: (a) Gold crystals shown under an optical microscope with colored line indicating the direction of measuring their thickness which is then plotted in (b). Photographed and measured by Lukáš Kejík.

Gold flakes

Gold flakes were grown by Lukáš Kejík in–situ by introducing aniline to a heated ethylene glycol solution of a hydrogen tetrachloroaurate ($HAuCl_4 \cdot 4H_2O$) [81]. Afterwards, they were transferred onto the fused silica samples and the liquid solution was evaporated. This resulted in our fused silica samples to be covered by a myriad of 2D gold crystals of varying sizes. The gold flakes we were looking for were around the size of a 100 μm and thickness of 200 nm. The crystals used for the next step are shown in Fig. 4.9(a) with their thickness measurements in Fig. 4.9(b). The crystals 3 and 6 were unused as they did not meet the criteria. Now we were ready to carve on–chip interferometers into these gold flakes.

Fabrication of on–chip interferometers

Using the Focused Ion Beam/Scanning Electron Microscope FEI Helios NanoLab 660 at CEITEC facility, several designs for plasmonic interferometers were milled into the samples. Square interference samples are shown in Fig. 4.10, two structures for exciting a focused plasmonic standing wave are displayed in Fig. 4.11(a) and two opposing slits type of interometer is in Fig. 4.11(b). These samples are ready to be measured by our setup.

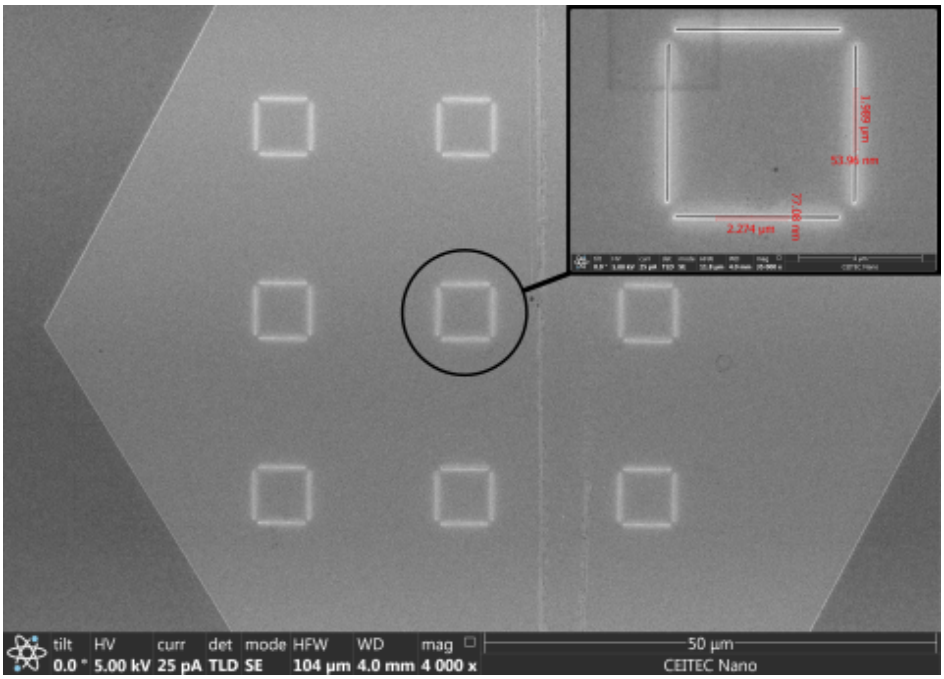

Fig. 4.10: A completed milling of a square slit design for plasmon interference. Milled using FIB and imaged using scanning electron microscopy (SEM) by Michal Horák.

4.3.2 Measurements of samples

The samples presented in the last section were measured using our holographic SNOM. Due to time constraints, only the square samples have been measured to this date. The process for measuring the surface plasmon hologram is as follow. The illumination laser is focused on the middle of the square. Next, it is defocused and split into two regions by SLM to illuminate the top and bottom slit with relative phase shift δ. For each phase shift of $\delta = n\pi/2$, where $n = 0,1,2,3,4$, a transmission measurement by SNOM is taken along with the topographic measurement. The topography is used to align images on each other before running the 5–step algorithm to extract the phase of SSPs. The final extracted image is showed in Fig. 4.12(a) along with a line cross

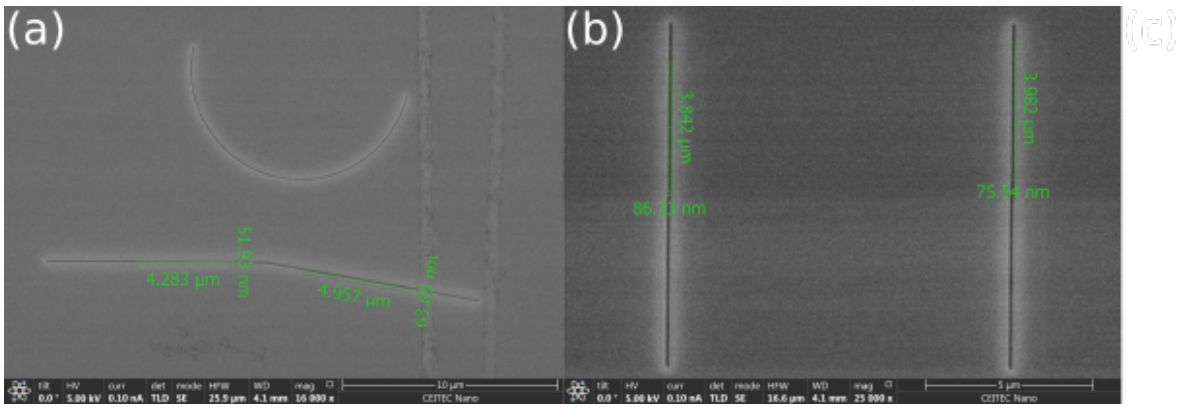

Fig. 4.11: (a) Two designs for creating a focused plasmonic wave. (b) Two parellel slits for creating plasmon interference. Milled using FIB and imaged using SEM by Michal Horák.

section shown in Fig. 4.12(b). The measured data can be compared with the analytical model shown in Fig. 4.13(a) and its cross section in Fig. 4.13(b). A nice correlation of measurement to the model can be observed. Also analytic and simulation models of SPP interference on square slits which are shown in Fig. 4.14(a),(b). The measured data is noisy, but a good correlation between the simulated and measured interference is also found which proves our setup to be operational.

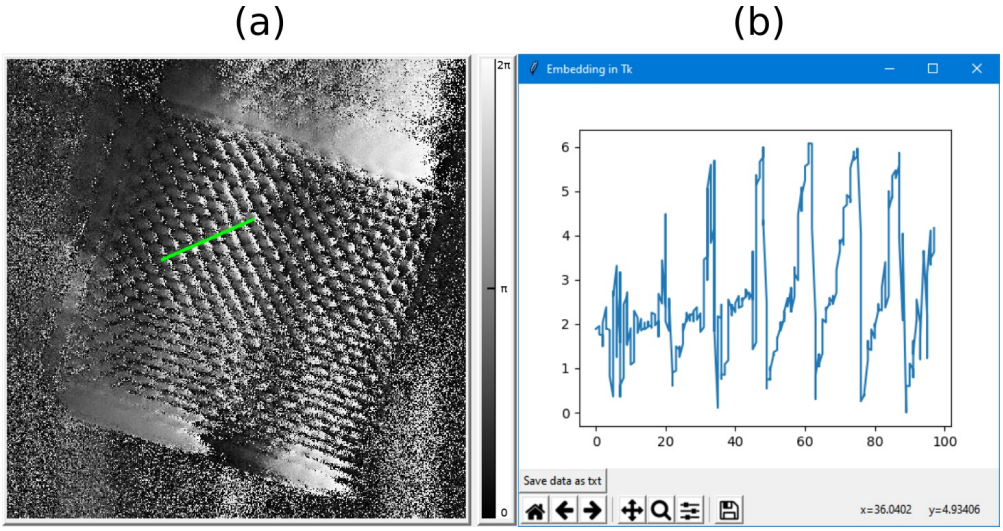

Fig. 4.12: (a) Measured plasmon interference on square slits using a–SNOM holography. The green line represents the line cross section displayed in (b).

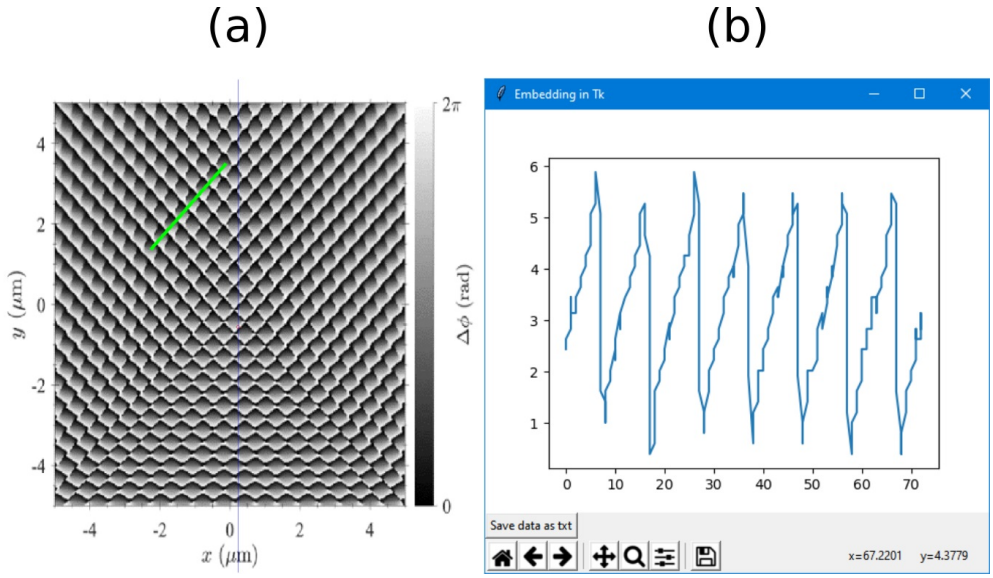

Fig. 4.13: (a) Simulated plasmon interference on square slits. The green line represents the line cross section displayed in (b).

Also, to experimentally confirm that our a–SNOM collects mostly $\mathbf{E}_\perp$ component of SPP waves as described in section 2.4.1, we can compare the analytic model of phase distribution for each component of electric field. In Fig. 4.15(a) and 4.15(b) are shown analytic models of $\mathbf{E}_\parallel$ and $\mathbf{E}_\perp$ respectively. It is clear to see how the out–of–plane component of electric field is dominant in our measurements.

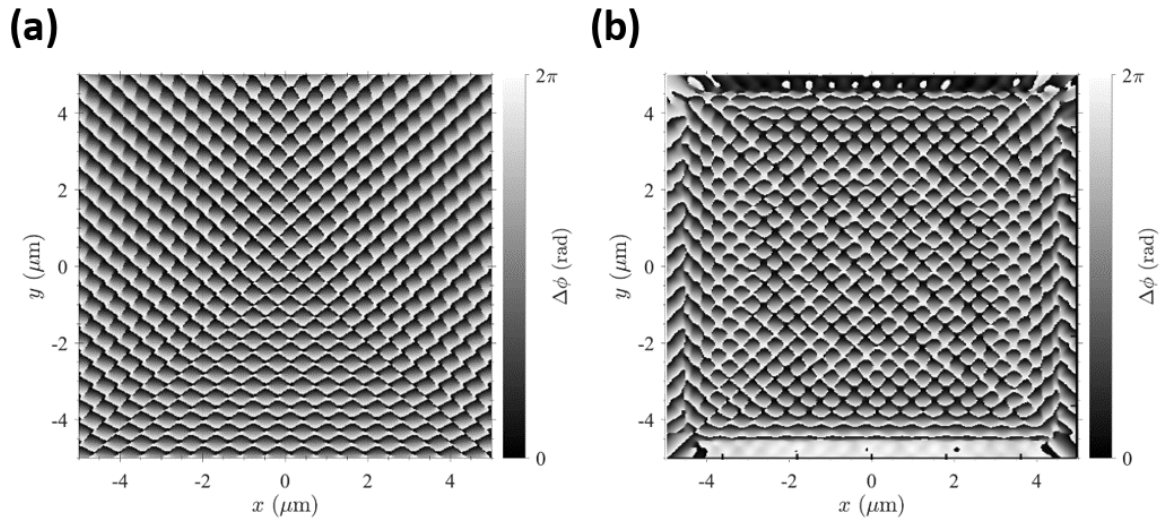

Fig. 4.14: Plasmon interference on square slits (a) analytically modeled, (b) simulated using finite–difference time–domain method.

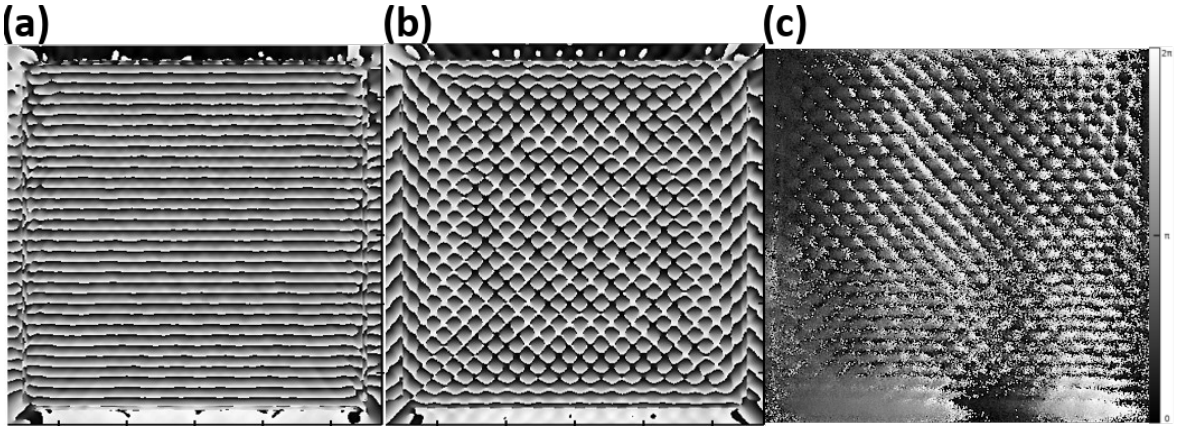

Fig. 4.15: Plasmon phase in an interference on square slits (a) analytically modeled, (b) simulated, (c) measured using a–SNOM holography.

5. CONCLUSIONS

The main objective of this thesis was to investigate possibilities of pushing the classical microscopy beyond the diffraction limit. First, a research on the topic of nanophotonics, plasmonics, interferometry, and optical imaging was carried out. The first chapter was built on this knowledge to give fundamental theoretical background for light–matter interactions, plasmonics, and nano–optics. First, it introduced the Maxwell's equations governing the behavior electromagnetic fields in a material. Next, models of dielectric function were derived which gave rise to the surface plasmon polaritons which are the foundation of plasmonics. Their detection and excitation was described in the relation to this thesis, especially the device called scanning near–field microscope which was utilized in our setup described in the last chapter.

Second chapter laid the theoretical foundation of optical interferometry and plasmon holography. First, we introduced the concept of interference of waves, and how standing waves arise from these equations. Next, two methods for phase extracting were introduced: phase shifting algorithms and off–axis holography. Then, phase shifting errors were explained. Finally, a step towards nanoworld was taken and surface plasmon holography was introduced.

In the third chapter, we focused on the topic of holography as mean of partially breaking the diffraction limit. We have constructed a Mach–Zehnder type digital holographic microscope which can operate in in–line regime by utilizing a phase shifting algorithm. By measuring the distortions of wavefront as it travels through a microoptical system, we can detect changes in length at the nanometer scale. A custom software was written for the microscope to allow fast measurements and data processing. The software can configure camera settings, can automatically calibrate piezo actuator voltages for phase shifting algorithm, extract and unwrap phase images, fitting of output wavefront, data manipulation, and more. The whole program was written in just over 1500 lines of code in MATLAB 2019a. The microscope was built primarily as a tool for microlens imaging for a Ph.D. project of Maryam Yousefi, a student at EPFL to finish her thesis, and several papers have been written utilizing it, one of which was accepted last December on the study of sinusoidal phase gratings [79]. The device was also used to measure metasurface phase shifting capabilities. We hope in the future the device will be used for more microlens research and that future students will innovate on it to produce even crisper holographic images.

Finally, the fourth chapter is focused on an experimental setup which enables true phase imaging under the diffraction limit. The scanning near–field holographic microscope. First we had to build the laser injection system. It went through several

iterations, finally settling on it after it was modeled in 3D in Blender. Next, the individual parts were assembled along with the SNOM microscope to create the complete setup as per the objectives set. During this time, several samples of nanoplasmonic structures were fabricated which was one of the objectives. They contained slits in gold film which excite SPP standing waves. These standing waves were to be then measured using our holographic SNOM. The measuring process was fairly slow, and had to be completed while in the laboratory. So, we highly optimized the process using stepper motors and software modules written in Python, in little over 2300 lines of code, which allowed remote control for the operator. This made the whole process more efficient and enabled even more precise control of the stage, focusing of the microscope, and phase mask generation. This finished setup was then used to measure the SPP phase profile of square samples fabricated earlier and by comparing the results with the theoretical models, we confirm that our setup is indeed working as expected completing the last objective of this Master's thesis.

In the future, we hope to finish measuring the other type of samples fabricated, and move onto more complicated sample layouts with added objects for us to study. We hope this holographic microscope can one day find its use for studying nanoobjects, living cells, proteins, and plasmonic nanostructures with unprecedented precision and open new possibilities in the realms of science.

BIBLIOGRAPHY

[1] Pullman, B. *The atom in the history of human thought*. Oxford University Press, 2001.

[2] Lane, N. The unseen world: reflections on leeuwenhoek (1677) (concerning little animals). *Philosophical Transactions of the Royal Society B: Biological Sciences 370*, 1666 (2015), 20140344. doi: 10.1098/rstb.2014.0344.

[3] McCartney, M. R., and Smith, D. J. Electron holography: Phase imaging with nanometer resolution. *Annual Review of Materials Research 37*, 1 (2007), 729–767. doi: 10.1146/annurev.matsci.37.052506.084219.

[4] Lenssen, B., and Bellouard, Y. Optically transparent glass micro-actuator fabricated by femtosecond laser exposure and chemical etching. *Applied Physics Letters 101*, 10 (2012), 103503. doi: 10.1063/1.4750236.

[5] KimMyung-K. *Journal of the Optical Society of Korea 14*, 2 (06 2010), 77–89.

[6] Korres, S., and Dienwiebel, M. Design and construction of a novel tribometer with online topography and wear measurement. *Review of Scientific Instruments 81*, 6 (2010), 063904. doi: 10.1063/1.3449334.

[7] Kühn, J., Charrière, F., Colomb, T., Montfort, F., Cuche, E., Emery, Y., Marquet, P., and Depeursinge, C. Dual-wavelength digital holographic microscopy with sub-nanometer axial accuracy. In *Optical Micro- and Nanometrology in Microsystems Technology II* (2008), C. Gorecki, A. K. Asundi, and W. Osten, Eds., vol. 6995, International Society for Optics and Photonics, SPIE, pp. 22 – 30. doi: 10.1117/12.781263.

[8] Synge, E. Xxxviii. a suggested method for extending microscopic resolution into the ultra-microscopic region. *The London, Edinburgh, and Dublin Philosophical Magazine and Journal of Science 6*, 35 (1928), 356–362. doi: 10.1080/14786440808564615.

[9] Binnig, G., Quate, C. F., and Gerber, C. Atomic force microscope. *Phys. Rev. Lett. 56* (Mar 1986), 930–933. doi: 10.1103/PhysRevLett.56.930.

[10] Pohl, D. W., Denk, W., and Lanz, M. Optical stethoscopy: Image recording with resolution $\lambda/20$. *Applied Physics Letters 44*, 7 (1984), 651–653. doi: 10.1063/1.94865.

[11] Taminiau, T. H., Stefani, F. D., Segerink, F. B., and van Hulst, N. F. Optical antennas direct single-molecule emission. *Nature Photonics 2*, 4 (Apr 2008), 234–237. doi: 10.1038/nphoton.2008.32.

[12] Dorfmüller, J., Vogelgesang, R., Khunsin, W., Rockstuhl, C., Etrich, C., and Kern, K. Plasmonic nanowire antennas: Experiment, simulation, and theory. *Nano Letters 10*, 9 (Sep 2010), 3596–3603. doi: 10.1021/nl101921y.

[13] Amenabar, I., Poly, S., Nuansing, W., Hubrich, E., Govyadinov, A., Huth, F., Krutokhvostov, R., Zhang, L., Knez, M., Heberle, J., Bittner, A., and Hillenbrand, R. Structural analysis and mapping of individual protein complexes by infrared nanospectroscopy. *Nature communications 4* (12 2013), 2890. doi: 10.1038/ncomms3890.

[14] Sandtke, M., Engelen, R. J. P., Schoenmaker, H., Attema, I., Dekker, H., Cerjak, I., Korterik, J. P., Segerink, F. B., and Kuipers, L. Novel instrument for surface plasmon polariton tracking in space and time. *Review of Scientific Instruments 79*, 1 (Jan 2008), 013704. doi: 10.1063/1.2825463.

[15] Schuller, J. A., Barnard, E. S., Cai, W., Jun, Y. C., White, J. S., and Brongersma, M. L. Plasmonics for extreme light concentration and manipulation. *Nature Materials 9*, 3 (Mar 2010), 193–204. doi: 10.1038/nmat2630.

[16] Chen, H.-T., Taylor, A., and yu, N. A review of metasurfaces: Physics and applications. *Reports on Progress in Physics 79* (May 2016). doi: 10.1088/0034-4885/79/7/076401.

[17] Pendry, J. B. Negative refraction. *Contemporary Physics 45*, 3 (May 2004), 191–202. doi: 10.1080/00107510410001667434.

[18] Basiri, A., Chen, X., Bai, J., Amrollahi, P., Carpenter, J., Holman, Z., Wang, C., and Yao, Y. Nature-inspired chiral metasurfaces for circular polarization detection and full-stokes polarimetric measurements. *Light: Science & Applications 8*, 1 (Aug 2019), 78. doi: 10.1038/s41377-019-0184-4.

[19] Tao, H., Chieffo, L. R., Brenckle, M. A., Siebert, S. M., Liu, M., Strikwerda, A. C., Fan, K., Kaplan, D. L., Zhang, X., Averitt, R. D., and Omenetto, F. G. Metamaterials on paper as a sensing platform. *Advanced Materials 23*, 28 (Jul 2011), 3197–3201. doi: 10.1002/adma.201100163.

[20] Walia, S., Shah, C. M., Gutruf, P., Nili, H., Chowdhury, D. R., Withayachumnankul, W., Bhaskaran, M., and Sriram, S. Flexible metasurfaces and metamaterials: A review of materials and fabrication processes at micro- and nano-scales. *Applied Physics Reviews 2*, 1 (Mar 2015), 011303. doi: 10.1063/1.4913751.

[21] Jiang, Z. H., Yun, S., Toor, F., Werner, D. H., and Mayer, T. S. Conformal dual-band near-perfectly absorbing mid-infrared metamaterial coating. *ACS Nano 5*, 6 (Jun 2011), 4641–4647. doi: 10.1021/nn2004603.

[22] Huft, P. R., Kolbow, J. D., Thweatt, J. T., and Lindquist, N. C. Holographic Plasmonic Nanotweezers for Dynamic Trapping and Manipulation. *Nano Letters 17*, 12 (Dec. 2017), 7920–7925. doi: 10.1021/acs.nanolett.7b04289.

[23] Xu, Y., Fu, Y., and Chen, H. Planar gradient metamaterials. *Nature Reviews Materials 1*, 12 (Oct 2016), 16067. doi: 10.1038/natrevmats.2016.67.

[24] Shalaev, V. M. Optical negative-index metamaterials. *Nature Photonics 1*, 1 (Jan 2007), 41–48. doi: 10.1038/nphoton.2006.49.

[25] Novotny, L., and Hecht, B. *Principles of nano-optics*. Cambridge University Press, 2019.

[26] Band, Y. B., and Avishai, Y. 9 - electronic properties of solids. In *Quantum Mechanics with Applications to Nanotechnology and Information Science*, Y. B. Band and Y. Avishai, Eds. Academic Press, Amsterdam, 2013, pp. 381 – 544. doi: https://doi.org/10.1016/B978-0-444-53786-7.00009-5.

[27] Puri, S. P. *Classical electrodynamics*. Alpha Science International Ltd., 2011.

[28] Seybold, J. S. *Introduction to RF propagation*. Wiley, 2005.

[29] Johnson, P. B., and Christy, R. W. Optical constants of the noble metals. *Phys. Rev. B 6* (Dec 1972), 4370–4379. doi: 10.1103/PhysRevB.6.4370.

[30] Derkachova, A., Kolwas, K., and Demchenko, I. Dielectric function for gold in plasmonics applications: Size dependence of plasmon resonance frequencies and damping rates for nanospheres. *Plasmonics 11*, 3 (Jun 2016), 941–951. doi: 10.1007/s11468-015-0128-7.

[31] Ligmajer, F. *Advanced plasmonic materials for metasurfaces and photochemistry*. PhD thesis, Brno University of Technology, 2018.

[32] Corum, K., Corum, J., and Miller, M. Surface waves and the 'crucial' propagation experiment — the key to efficient wireless power delivery. pp. 1–4. doi: 10.1109/WMCaS.2016.7577497.

[33] Otto, A. Excitation of nonradiative surface plasma waves in silver by the method of frustrated total reflection. *Zeitschrift für Physik A Hadrons and nuclei 216*, 4 (Aug 1968), 398–410. doi: 10.1007/BF01391532.

[34] Kretschmann, E., and Raether, H. Notizen: Radiative decay of non radiative surface plasmons excited by light. *Zeitschrift für Naturforschung A 23*, 12 (1968), 2135 – 2136. doi: https://doi.org/10.1515/zna-1968-1247.

[35] Homola, J., Yee, S. S., and Gauglitz, G. Surface plasmon resonance sensors: review. *Sensors and Actuators B: Chemical 54*, 1 (1999), 3 – 15. doi: https://doi.org/10.1016/S0925-4005(98)00321-9.

[36] Martin-Fernandez, M. L., Tynan, C. J., and Webb, S. E. D. A 'pocket guide' to total internal reflection fluorescence. *Journal of microscopy 252*, 1 (Oct 2013), 16–22. 23889125[pmid]. doi: 10.1111/jmi.12070.

[37] Yao, Y.-F., Lin, C.-H., Chao, C.-Y., Chang, W.-Y., Su, C.-Y., Tu, C.-G., Kiang, Y.-W., and Yang, C. C. Coupling of a light-emitting diode with surface plasmon polariton or localized surface plasmon induced on surface silver gratings of different geometries. *Opt. Express 26*, 7 (Apr 2018), 9205–9219. doi: 10.1364/OE.26.009205.

[38] Baudrion, A.-L., de León-Pérez, F., Mahboub, O., Hohenau, A., Ditlbacher, H., García-Vidal, F. J., Dintinger, J., Ebbesen, T. W., Martín-Moreno, L., and Krenn, J. R. Coupling efficiency of light to surface plasmon polariton for single subwavelength holes in a gold film. *Opt. Express 16*, 5 (Mar 2008), 3420–3429. doi: 10.1364/OE.16.003420.

[39] Hell, S. W., and Wichmann, J. Breaking the diffraction resolution limit by stimulated emission: stimulated-emission-depletion fluorescence microscopy. *Opt. Lett. 19*, 11 (Jun 1994), 780–782. doi: 10.1364/OL.19.000780.

[40] Rust, M. J., Bates, M., and Zhuang, X. Sub-diffraction-limit imaging by stochastic optical reconstruction microscopy (storm). *Nature Methods 3*, 10 (Oct 2006), 793–796. doi: 10.1038/nmeth929.

[41] Guerra, J. M. Super-resolution through illumination by diffraction-born evanescent waves. *Applied Physics Letters 66*, 26 (1995), 3555–3557. doi: 10.1063/1.113814.

[42] Chen, X., Hu, D., Mescall, R., You, G., Basov, D. N., Dai, Q., and Liu, M. Modern scattering-type scanning near-field optical microscopy for advanced material research. *Advanced Materials 31*, 24 (2019), 1804774. doi: 10.1002/adma.201804774.

[43] Lewis, A., Isaacson, M., Harootunian, A., and Muray, A. Development of a 500 åspatial resolution light microscope: I. light is efficiently transmitted through $\lambda/16$ diameter apertures. *Ultramicroscopy 13*, 3 (1984), 227 – 231. doi: https://doi.org/10.1016/0304-3991(84)90201-8.

[44] Oshikane, Y., Kataoka, T., Okuda, M., Hara, S., Inoue, H., and Nakano, M. Observation of nanostructure by scanning near-field optical microscope with small sphere probe. *Science and Technology of Advanced Materials 8*, 3 (2007), 181–185. doi: 10.1016/j.stam.2007.02.013.

[45] Burresi, M., van Oosten, D., Kampfrath, T., Schoenmaker, H., Heideman, R., Leinse, A., and Kuipers, L. Probing the magnetic field of light at optical frequencies. *Science 326*, 5952 (2009), 550–553. doi: 10.1126/science.1177096.

[46] Gomez, L., Bachelot, R., Bouhelier, A., Wiederrecht, G., Gray, S., Hua, F., Jeon, S., Rogers, J., Castro, M., Blaize, S., Stefanon, I., Lerondel, G., and Royer, P. Aperture less scanning near-field optical microscopy: A comparison between homodyne and heterodyne approaches. *JOSA B 23* (05 2006). doi: 10.1364/JOSAB.23.000823.

[47] Huth, F., Govyadinov, A., Amarie, S., Nuansing, W., Keilmann, F., and Hillenbrand, R. Nano-FTIR Absorption Spectroscopy of Molecular Fingerprints at 20 nm Spatial Resolution. *Nano Letters 12*, 8 (Aug. 2012), 3973–3978. doi: 10.1021/nl301159v.

[48] Sonntag, M. D., Pozzi, E. A., Jiang, N., Hersam, M. C., and Van Duyne, R. P. Recent advances in tip-enhanced raman spectroscopy. *The Journal of Physical Chemistry Letters 5*, 18 (Sep 2014), 3125–3130. doi: 10.1021/jz5015746.

[49] Ianoul, A., Street, M., Grant, D., Pezacki, J., Taylor, R. S., and Johnston, L. J. Near-field scanning fluorescence microscopy study of ion channel clusters in cardiac myocyte membranes. *Biophysical Journal 87*, 5 (2004), 3525 – 3535. doi: https://doi.org/10.1529/biophysj.104.046383.

[50] Lahrech, A., Bachelot, R., Gleyzes, P., and Boccara, A. C. Infrared-reflection-mode near-field microscopy using an apertureless probe with a resolution of $\lambda/600$. *Opt. Lett. 21*, 17 (Sep 1996), 1315–1317. doi: 10.1364/OL.21.001315.

[51] Hillenbrand, R., Taubner, T., and Keilmann, F. Phonon-enhanced light–matter interaction at the nanometre scale. *Nature 418*, 6894 (Jul 2002), 159–162. doi: 10.1038/nature00899.

[52] Richards, D., Zayats, A., Keilmann, F., and Hillenbrand, R. Near-field microscopy by elastic light scattering from a tip. *Philosophical Transactions of the Royal Society of London. Series A: Mathematical, Physical and Engineering Sciences 362*, 1817 (2004), 787–805. doi: 10.1098/rsta.2003.1347.

[53] Brehm, M., Taubner, T., Hillenbrand, R., and Keilmann, F. Infrared spectroscopic mapping of single nanoparticles and viruses at nanoscale resolution. *Nano Letters 6*, 7 (Jul 2006), 1307–1310. doi: 10.1021/nl0610836.

[54] Hammerland, D. *Boundary Effects in Van der Waals Materials*. PhD thesis, 04 2016.

[55] Gigler, A. M., Huber, A. J., Bauer, M., Ziegler, A., Hillenbrand, R., and Stark, R. W. Nanoscale residual stress-field mapping around nanoindents in sic by ir s-snom and confocal raman microscopy. *Opt. Express 17*, 25 (Dec 2009), 22351–22357. doi: 10.1364/OE.17.022351.

[56] Gerber, J. A., Berweger, S., O'Callahan, B. T., and Raschke, M. B. Phase-resolved surface plasmon interferometry of graphene. *Phys. Rev. Lett. 113* (Jul 2014), 055502. doi: 10.1103/PhysRevLett.113.055502.

[57] Amarie, S., Ganz, T., and Keilmann, F. Mid-infrared near-field spectroscopy. *Opt. Express 17*, 24 (Nov 2009), 21794–21801. doi: 10.1364/OE.17.021794.

[58] Krpenský, J. *Interakce mezi SNOM hrotem a blízkým elektromagnetickým polem.* Vysoké učení technické v Brně, Fakulta strojního inženýrství, 2020. 36 s. Vedoucí Ing. Petr Dvořák, Ph.D.

[59] Turner, D. R. Etch procedure for optical fibers, 1983.

[60] Scott, A. Encyclopedia of nonlinear science, 2014.

[61] Chmelík, R., Petráček, J., Slabá, M., Kollárová, V., Slabý, T., Čolláková, J., Komrska, J., Dostál, Z., and Veselý, P. Holographic microscopy in low coherence. In *Quantitative Phase Imaging II* (2016), G. Popescu and Y. Park, Eds., vol. 9718, International Society for Optics and Photonics, SPIE, pp. 40 – 46. doi: 10.1117/12.2209465.

[62] Remmersmann, C., Stuerwald, S., Kemper, B., Langehanenberg, P., and Bally, G. Phase noise optimization in temporal phase-shifting digital holography with partial coherence light sources and its application in quantitative cell imaging. *Applied optics 48* (04 2009), 1463–72. doi: 10.1364/AO.48.001463.

[63] Schwider, J., Burow, R., Elssner, K.-E., Grzanna, J., Spolaczyk, R., and Merkel, K. Digital wave-front measuring interferometry: some systematic error sources. *Appl. Opt. 22*, 21 (Nov 1983), 3421–3432. doi: 10.1364/AO.22.003421.

[64] Goodwin, E. P., and Wyant, J. C. 2006, ch. Field Guide tolinterferometric Optical Testing, p. 32-42.

[65] Moon, I., Yi, F., Lee, Y., Javidi, B., Boss, D., and Marquet, P. Automated quantitative analysis of 3d morphology and mean corpuscular hemoglobin in human red blood cells stored in different periods. *Optics express 21* (12 2013), 30947–57. doi: 10.1364/OE.21.030947.

[66] Zia, R., and Brongersma, M. L. Surface plasmon polariton analogue to young's double-slit experiment. *Nature Nanotechnology 2*, 7 (Jul 2007), 426–429. doi: 10.1038/nnano.2007.185.

[67] Hecht, B., Bielefeldt, H., Novotny, L., Inouye, Y., and Pohl, D. W. Local excitation, scattering, and interference of surface plasmons. *Phys. Rev. Lett. 77* (Aug 1996), 1889–1892. doi: 10.1103/PhysRevLett.77.1889.

[68] Gordon, R., Sinton, D., Kavanagh, K. L., and Brolo, A. G. A new generation of sensors based on extraordinary optical transmission. *Accounts of Chemical Research 41*, 8 (Aug 2008), 1049–1057. doi: 10.1021/ar800074d.

[69] Willets, K. A., and Van Duyne, R. P. Localized surface plasmon resonance spectroscopy and sensing. *Annual Review of Physical Chemistry 58*, 1 (2007), 267–297. PMID: 17067281. doi: 10.1146/annurev.physchem.58.032806.104607.

[70] Nelson, J. W., Knefelkamp, G. R., Brolo, A. G., and Lindquist, N. C. Digital plasmonic holography. *Light: Science & Applications 7*, 1 (Aug 2018), 52. doi: 10.1038/s41377-018-0049-2.

[71] Dvořák, P. *Nanophotonics*. PhD thesis, Brno University of Technology, 2018.

[72] Dvořák, P., Kvapil, M., Bouchal, P., Édes, Z., Šamořil, T., Hrtoň, M., Ligmajer, F., Křápek, V., and Šikola, T. Near-field digital holography: a tool for plasmon phase imaging. *Nanoscale 10* (2018), 21363–21368. doi: 10.1039/C8NR07438K.

[73] Yoon, S.-K., Cho, H.-J., Kim, D.-C., Yu, Y., and Kim, S.-K. Phase unwrapping using modified goldstein algorithm in digital holography. *Korean Journal of Optics and Photonics 18* (04 2007), 122–129. doi: 10.3807/HKH.2007.18.2.122.

[74] Pulaski, P. D., Roller, J. P., Neal, D. R., and Ratte, K. Measurement of aberrations in microlenses using a Shack-Hartmann wavefront sensor. In *Current Developments in Lens Design and Optical Engineering III* (2002), R. E. Fischer, W. J. Smith, and R. B. Johnson, Eds., vol. 4767, International Society for Optics and Photonics, SPIE, pp. 44 – 52. doi: 10.1117/12.451325.

[75] Software for mach–zehnder holographic microscope written in matlab 2019a, https://github.com/Mejval5/Mach-Zehnder-microscope.

[76] Goldstein, R. M., Zebker, H. A., and Werner, C. L. Satellite radar interferometry: Two-dimensional phase unwrapping. *Radio Science 23*, 4 (1988), 713–720.

[77] Spottiswoode, B. 2d phase unwrapping algorithms, 2008.

[78] Goodman, J. W. *Introduction to Fourier optics*. McGraw-Hill, 2017.

[79] Yousefi, M., Nečesal, D., Scharf, T., and Rossi, M. Simulation of micro-optics under inhomogeneous illumination: Sinusoidal phase grating under gaussian beam illumination. In *2019 24th Microoptics Conference (MOC)* (2019), pp. 224–225.

[80] Software for scanning near–field holographic microscope written in python 3.6, https://github.com/Mejval5/Plasmon-holographic-microscope.

[81] Guo, Z., Zhang, Y., DuanMu, Y., Xu, L., Xie, S., and Ning, G. Facile synthesis of micrometer-sized gold nanoplates through an aniline-assisted route in ethylene glycol solution. *Colloids and Surfaces A: Physicochemical and Engineering Aspects 278* (04 2006), 33–38. doi: 10.1016/j.colsurfa.2005.11.075.

LIST OF ABBREVIATIONS

a–SNOM ..... Aperture type scanning near–field optical microscope

AFM ..... Atomic force microscope

ATR ..... Attenuated total reflection

CCD ..... Charge–coupled device

CEITEC ..... Central European Institute of Technology

COM ..... Communication port

EPFL ..... Ecole polytechnique fédérale de Lausanne

FDTD ..... Finite–difference time–domain method

FTIR ..... Fourier transform infrared spectroscopy

FIB ..... Focused ion beam

FLM ..... Feedback–loop mechanism

GUI ..... Graphical user interface

NA ..... Numerical aperture

PSI ..... Phase shifting interferometry

SEM ..... Scanning electron microscope

SLM ..... Spatial light modulator

SNOM ..... Scanning near–field microscope

SPM ..... Scanning probe microscope

SPP ..... Surface plasmon polariton

STM ..... Scanning tunneling microscope

s–SNOM ..... Scattering type scanning near–field optical microscope

TM ..... Transverse magnetic

USB ..... Universal serial bus